Investigations of Sooting Laminar Coflow Diffusion Flames at Elevated Pressures

Dissertation by

Scott Andrew Steinmetz

In Partial Fulfillment of the Requirements

For the Degree of

Doctor of Philosophy in Mechanical Engineering

King Abdullah University of Science and Technology, Thuwal,

Kingdom of Saudi Arabia

EXAMINATION COMMITTEE PAGE

The dissertation of Scott Andrew Steinmetz is approved by the examination committee

Committee Chairperson: Mani Sarathy

Committee Member: Suk Ho Chung

Committee Member: William L. Roberts

Committee Member: Fabrizio Bisetti

Committee Member: Murray J. Thomson

ABSTRACT

Investigations of Sooting Laminar Coflow Diffusion Flames at Elevated Pressures

Scott Andrew Steinmetz

Soot is a common byproduct of hydrocarbon based combustion systems. It poses a risk to human and environmental health, and can negatively or positively affect combustor performance. As a result, there is significant interest in understanding soot formation in order to better control it. More recently, the need to study soot formation in engine relevant conditions has become apparent. One engine relevant parameter that has had little focus is the ambient pressure. This body of work focuses on the formation of soot in elevated pressure environments, and a number of investigations are carried out with this purpose. Laminar coflow diffusion flames are used as steady, simple soot producers.

First, a commonly studied flame configuration is further characterized. Coflow flames are frequently used for fundamental flame studies, particularly at elevated pressures. However, they are more susceptible to buoyancy induced instabilities at elevated pressures. The velocity of the coflow is known to have an effect on flame stability and soot formation, though these have not been characterized at elevated pressures. A series of flames are investigated covering a range of flowrates, pressures, and nozzle diameters. The stability limits of coflow flames in this range is investigated. Additionally, an alternative strategy for scaling these flames to elevated pressures is proposed. Finally, the effect of coflow rate on soot formation is evaluated.

Identification of fundamental flames for coordinated research can facilitate our understanding of soot formation. The next study of this work focuses on adding soot

concentration and particle size information to an existing fundamental flame dataset for the purpose of numerical model validation. Soot volume fraction and average particle diameters are successfully measured in nitrogen-diluted ethylene-air laminar coflow flames at pressures of 4, 8, 12, and 16 atm. An increase in particle size with pressure is found up to 12 atm, where particle sizes plateau. Particle size in the annulus is more sensitive to pressure.

Next, the development of an alternative particle size measuring technique is studied. Time Resolved Laser Induced Incandescence (TiRe-LII) is a commonly used technique to measure soot concentrations and particle size at atmospheric pressure. However, Laser Induced Incandescence (LII) models suffer from an incomplete understanding of the effects of elevated pressures on the absorption, annealing, and cooling of soot. The present study focuses on what affect the laser temporal pulse shape and duration may have on particle sizing. TiRe-LII in flames at 1 and 15 bar is carried out, using laser pulses with tophat or Gaussian temporal profiles of varying duration. Mono-disperse equivalent primary particle diameters are calculated using the KAUST LII model. Little difference in particle sizing is found for different laser pulses. However, this data will be useful for validating the KAUST LII model when absorption and poly-dispersion are accounted for.

In an effort to move one step closer to logistical fuel studies, the sooting tendencies of a number of liquid fuels are studied at pressures up to 10. Of parallel relevance, a sooting index for surrogate development is evaluated for elevated pressure applications. The Yield Sooting Index (YSI) methodology is applied to 11 normal, cyclic, and branched alkanes. When referencing to two n-alkane fuels, the YSI of n-alkanes determined at atmospheric pressures accurately reflects the relative sooting tendencies of these fuels at elevated pressures. The relative sooting tendencies of cyclo- and methyl-alkanes have a lower pressure sensitivity than n-alkanes.

TABLE OF CONTENTS

LIST OF ABBREVIATIONS

AR	Anti-Reflective
BPR	Back-Pressure Regulator
CCD	Charge-Coupled Device
CTA	Constant Temperature Anemometry
DLE	Diffuse Light Extinction
FWHM	Full Width at Half Maximum
GC	Gas Chromotography
HAB	Height Above Burner
HeNe	Helium-Neon
ISF	International Sooting Flame Workshop
LCC	L-Curve Criterion
LES	Laser Extinction and Scattering
LE	Laser Extinction
LIF	Laser Induced Fluorescence
LII	Laser Induced Incandescence
LOSA	Line-of-Sight Attenuation
MFC	Mass Flow Controller
Nd:YAG	Neodymium-doped Yttrium Aluminum Garnet
PAH	Polycyclic Aromatic Hydrocarbons
PMT	Photomultiplier Tube
RDG-PFA	Rayleigh-Debye-Gans Polydisperse Fractal Aggregates
RDG	Rayleigh-Debye-Gans
SSE	Spectral Soot Emisison
STI	Soot Temperature Index
TEM	Transmission Electron Microscopy
TERF	Two-Exponential Reverse Fitting
TSI	Threshold Soot Index
TiRe-LII	Time Resolved Laser Induced Incandescence

YSI Yield Sooting Index

LIST OF SYMBOLS

a	Acceleration constant - 32 [m/s^2]
c	Speed of light constant - 3.00$\times 10^8$ [m/s]
C_{CO}	Molar specific heat of carbon monoxide
c_p	Mass specific heat
$c_{p,s}$	Mass specific heat of soot
D	Particle diameter
d	Nozzle diameter
D_{63}	Volume-weighted particle diameter
D_f	Fractal dimension
d_p	Primary particle diameter
$d_{p,eff}$	Effective primary particle diameter
$E(m)$	Imaginary refractive index function
F	Laser fluence
f	Focal length
$F(m)$	Real refractive index function
Fr	Froude number
f_{sv}	Soot surface are per unit volume of gas
f_v	Soot volume fraction
$f_{v,a}$	Path averaged soot volume fraction
g	Gravitational constant - 9.81 [m/s^2]
Gr	Grashof number
H	Flame Height
h	Planck constant - 6.626$\times 10^{-24}$ [m^{2}kg/s]
$\triangle H_{ox}$	Enthalpy of reaction

$\triangle H_v$	Enthalpy of formation
I	Intensity
k	$2\pi/\lambda$
k_B	Boltzmann constant - 1.381×10^{-23} [m^2kg/s^2K]
k_f	Fractal prefactor
k_g	Thermal conductivity
k_{ox}	Reaction rate on soot surface
k_s	Soot surface growth/oxidation rate
L	Path length
M	Particle mass
m	Refractive index
$\dot{m}$	Mass flow rate
m_e	Mass of electron
mw	Molecular Weight
N	Soot particle number density
N_A	Avogadro's number - 6.02×10^{23}
P	Pressure
Pr	Prandtl number
$\dot{Q}$	Energy transfer rate
Q	Standard volumetric flowrate
q	Scattering wave vector - $2k\sin\theta/2$
q_1	Normalization constant
$q(t)$	Temporal profile of laser pulse normalized to 1
Q_{vv}	Differential scattering cross section
R	Universal gas constant - 8.314 [kJ/kmol K]
Re	Reynolds number

R_g	Radius of gyration
Ri	Richardson number
r_u	Velocity ratio - U_{coflow}/U_{nozzle}
S	Inverse Stoichiometric ratio
T	Temperature
t	Time
T_0	Inlet temperature
$\overline{T}$	Film temperature
T_δ	Limiting sphere temperature
T_f	Flame temperature
T_g	Gas temperature
T_p	Particle temperature
U	Bulk velocity
$U_{internal}$	Internal energy
v_z	Axial velocity
W_1	Average molecular weight of carbon atom
W_g	Average molecular weight of gas
W_v	Average molecular weight of sublimed cluster
Z	Mixture fraction
α	Thermal diffusivity
α_m	Mass accommodation coefficient
α_T	Thermal accommodation coefficient
χ	Scalar dissipation rate
δ	Langmuir layer thickness
ϵ_λ	Spectral emissivity of soot
η_s	Soot yield
γ^*	Mean specific heat ratio
κ_a	Absorption coefficient
κ_e	Extinction coefficient
κ_s	Scattering coefficient

λ	Wavelength
λ_r	Regularization parameter
μ	Dynamic viscosity
ν	Kinematic viscosity
ϕ	Work function
ρ	Gas density
ρ_s	Density of soot
ρ_{sa}	Ratio of scattering to absorption coefficients
ρ_v	Average saturation partial pressure of sublimed cluster
τ	Transmissivity

LIST OF FIGURES

LIST OF TABLES

Chapter 1

Introduction

This chapter provides an introduction to the current challenge, why we are interested in overcoming it, and what steps have been taken thus far. Key areas that need addressing are highlighted, as well as the specific objectives of this work. Further background information is provided in the introductions to the individual studies (Chapters 4, 5, 6, and 7).

1.1 Motivation

One byproduct of hydrocarbon combustion is the formation of soot; carbonaceous particulate which is both a human health and environmental hazard [1–3]. Soot contributes to climate change by increasing solar radiation absorption by the ground and oceans, and altering cloud formation and stability [3–5]. Soot production can also lead to deacreased engine performance [6]. However, soot serves a beneficial role as an effective radiator of heat in furnace applications [7]. The formation of soot is governed by complex coupled processes [8, 9], and in order to control it, a better understanding of these processes is necessary. Numerous experimental and computational studies have been carried out with this goal, often focusing on measuring and simulating temperature fields, gas-phase species concentrations, and soot concentrations under different conditions. The ultimate goal is predictive capability of soot formation in real devices.

Diffusion-flame based combustion devices, such as diesel and gas-turbine engines,

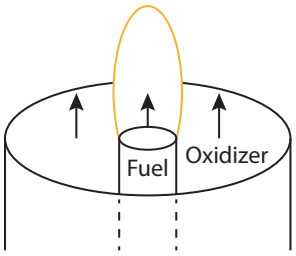

Figure 1.1: Typical coflow configuration.

are used for their stability and efficiency, and are major sources of soot production. While these devices are generally operated in a turbulent regime for decreased length- and time-scales, laminar flames are often more advantageous to study. Due to their steady nature, laminar flames allow fluid dynamics to be more easily characterized and separated from other combustion processes. The laminar flamelet concept allows us to apply our understanding of laminar flames to turbulent flames. Therefore, laminar diffusion flames are ideal for fundamental soot studies. The coflow jet configuration is a simple representation of diesel and gas turbine flames, making laminar coflow flames ideal for fundamental studies. In a coflow burner, a central fuel stream is surrounded by a coflowing oxidizer stream. A typical coflow burner is depicted in Fig. 1.1. A flame will stabilize in a conical shape close to the central nozzle, with the flame front located where the fuel and oxidizer are mixed stoichiometrically. The axisymmetric geometry makes experimental and numerical investigations much easier.

One parameter which has an important impact on soot formation is the ambient pressure in which the combustion is taking place. In engines, high pressure operation is desired for increased thermal efficiency. Gas turbine operating pressures are typically in the range of 15 to 45 bar, and diesel engines can achieve intermittent pressures of 100 bar. However, the majority of fundamental research on soot formation is done in flames under atmospheric conditions. The high cost and safety concerns associated with pressure vessels, and the additional complications and uncertainties in conducting experiments in a high pressure environment, make this type of research

unattractive. This has resulted in a large knowledge gap in our understanding of the effects of pressure on soot formation, though this gap has slowly been filled in recent years.

1.2 Previous Studies at Elevated Pressures

There have been various studies of soot in super-atmospheric flames, whether premixed or diffusion based, in both turbulent and laminar regimes [10–17]. The discussion here will focus on experimental studies in laminar diffusion flames at elevated pressure. One of the earliest studies of soot in pressurized diffusion flames was conducted by Schalla et al. [18]. They investigated smoke heights in wick-fed diffusion flames of liquid fuels up to 20 atm. They found an inverse relationship between pressure and smoke height, which is proportional to fuel flow rate, indicating an increase in sooting tendency with pressure. They also observed different sensitivities to pressure depending on fuel. Miller and Maahs [19] carried out methane-air diffusion flame experiments up to 50 atm investigating NO_x formation. They measured soot temperature using two-color pyrometry, and estimated soot concentrations based on this temperature. While maintaining constant fuel flow rate, they observed a narrowing of the flame with pressure, but an almost constant flame height. They observed a large increase in soot concentrations with pressure up to 40 atm, where concentrations leveled off. The location of soot was also found to move lower into the flame as pressure increased. Flower and Bowman [20–23] used Laser Extinction and Scattering (LES) to measure soot volume fraction, f_v, and size in ethylene-air flames in a Wolfhard-Parker burner up to 2.5 atm. They maintained fuel velocities as pressure was increased to keep constant residence times at a given flame height. Accounting for increased fuel flow rate, they conclude soot yield scaled with pressure as $P^{0.7}$. They also conclude that increased inception rates at elevated pressures result in increased soot surface area, leading to faster growth [23]. Flower and Bowman [24]

also investigated ethylene coflow diffusion flames from 1 to 10 atm using LES. In this study, mass flow rate was held constant as pressure was varied, and peak path averaged soot volume fractions, $f_{v,a}$, were found to scale with pressure as $P^{1.2}$, with this scaling decreasing near 10 atm.

Recently, high pressure soot studies have become more common, with researchers often focusing on determining the scaling power of soot yield with pressure. Lee and Na [25] measured soot temperature and f_v in ethylene and ethylene mixture flames up to 4 bar using two-color pyrometry. In addition to finding a lower temperature limit for soot oxidation of 1400 K, they obtained the first radially resolved measurements of f_v at elevated pressures. They report a similar $P^{1.3}$ scaling for $f_{v,a}$ as in [24], in addition to a P^2 scaling for local f_v for a pressure range of 2 to 4 bar. McCrain and Roberts investigated methane-air and ethylene-air flames from 1-25 atm and 1-16 atm, respectively, using Laser Extinction (LE) calibrated Laser Induced Incandescence (LII) [26]. They observed the same $P^{1.2}$ scaling of peak $f_{v,a}$ in ethylene flames, and a $P^{1.7}$ scaling in local peak f_v. For methane flames, the average and local pressure scaling exponents were 1 and 1.2, respectively. Berry and Roberts [27] investigated smoke point in pure ethylene flames up to 16 atm, confirming the inverse relationship between pressure and smoke height of [18]. They also observed a increase in smoke point fuel flow rate with pressure, which is contrary the the observations of [18]. They later investigated the effect of dilution on ethylene and methane flame smoke points using a number of diluents [28]. They observed large differences in the impact on dilution depending on fuel nozzle exit velocity profile, with a parabolic velocity profile resulting in higher sensitivity of the smoke point to diluent. Berry Yelverton and Roberts [29] also used two-color pyrometry to investigate soot temperature in diluted ethylene flames from 1-8 atm.

Thomson et al. [30] used Line-of-Sight Attenuation (LOSA) and Spectral Soot Emisison (SSE) to measure soot temperature and f_v in methane flames from 5-40

atm. It was observed that $f_{v,a}$ scales with pressures as $P^{1.3}$ in the range of 5-20 atm, but as $P^{0.9}$ in the range of 20-40 atm. Due to the decrease in flame cross section with pressure, f_v will naturally increase even if the soot yield is the same. The percent of carbon converted to soot, evaluated over the entire cross section, is a better measure of soot yield. In these experiments, carbon conversion was found to scale with pressure as $P^{1.0}$ from 5-20 atm, and $P^{0.1}$ from 20-40 atm. These measurements show a diminishing effect of pressure above 20 atm. Joo and Gülder [31] extended this work up to 60 atm, finding a scaling of $P^{0.33}$ from 30-60 atm for peak carbon conversion. They attributed the slight increase compared to [30] to incorrect flow rate calibration in that work. Bento et al. [32] next investigated propane flames from 1-7.3 atm on the same experimental setup, again with LOSA and SSE. They found $f_{v,a}$ and peak carbon conversion, η_s, scaled with pressure exponents of 1.4 and 1.1, respectively, in the range of 2-7.3 atm. Mandatori and Gülder [33] then used SSE to measure temperature and f_v in ethane flames from 1-33 atm. Peak $f_{v,a}$ was found to scale with pressure exponents of 2.3 from 2-5 atm, 1.1 from 5-15 atm, and 1.0 from 15-33 atm, while peak carbon conversion scaled with exponents of 2.2, 1.1, and 0.4 for the same pressure ranges, respectively. Joo and Gülder [34] also investigated ethylene flames, diluted 5:1 by volume with nitrogen. Peak $f_{v,a}$ scaled with pressure as $P^{1.62}$, and peak carbon conversion scaled as $P^{1.36}$ in the range of 10-30 atm.

Gülder et al. [35] summarized the relationship between pressure and η_s for the aliphatic compounds in [30–33]. They found that when soot yields are normalized to those of a reference fuel, methane used as an example, they collapse onto a single curve as a function of reduced pressure, pressure normalized by the critical pressure of the mixture. This reduced soot yield demonstrates an exponential dependence on reduced pressure, where the pressure dependence asymptotes near the critical pressure. The authors question whether this normalization would also work for flames of liquid fuels.

Typically, these experiments are carried out in burners of fixed geometry, with a

constant mass flowrate of fuel. Some common observations in these previous studies include a narrowing of the flame with pressure, constant flame height with pressure for constant fuel flow rate, increase in f_v with pressure, and a shift in the location of peak soot from flame tip to annulus. Soot concentrations increase due to flame constriction and increased soot formation rates. The strength of the pressure dependance is fuel dependent, and this strength reduces approaching the critical pressure of the fuel mixture. The current state of the art is well summarized by Karataş and Gülder [36].

1.3 Current Knowledge Gaps

As most work has focused on the pressure sensitivity of f_v, there are still several areas that need to be addressed. The International Sooting Flame Workshop (ISF) was formed with the following aims, as listed on their website [37]:

- To identify common research priorities in the development and validation of accurate, predictive models of flames with soot and to coordinate research programs to address them.
- To identify and coordinate well-defined target flames that are suitable for model development and validation, spanning a variety of flame types and fuels in each of the Research Programs.
- To establish an archive of the detailed data sets of target flames with defined accuracy; and to provide a forum for the exchange and dissemination of these data.

One of the aforementioned research programs focuses on pressurized flames. Previous studies have established a data set for the target pressurized laminar coflow diffusion flame [38, 39]. To facilitate the goals of the ISF, further data needs to be added to this dataset.

One aspect of soot that has yet to be sufficiently addressed in high pressure environments is morphological information. Particle size is known to be important in relation to a particle's toxicity [40]. Upcoming regulations will focus on particle mass and number densities (and hence size). However, there are a few studies investigating these issues.

Thomson et al. [41] used auto-compensating LII to measure f_v and effective primary particle diameter ($d_{p,eff}$) in the same 5-40 atm methane flames previously studied [30]. They found good agreement with the previous f_v measurements, and provide some of the first measurements of particle size in high pressure flames. They observed an increase in primary particle diameter, d_p, with pressure, but point out the large uncertainties in the LII model and analysis in high pressure environments. Kim et al. [42] did an extensive study of diluted ethylene flames up to 8 atm using a combination of LOSA, multi-wavelength pryometry, isokinetic gas sampling and analysis by Gas Chromotography (GC), Li/LiOH atomic absorption, thermophoretic sampling and Transmission Electron Microscopy (TEM) analysis, and laser velocimetry to measure f_v, temperature, major hydrocarbon species and radicals, d_p, and velocity. They found a small increase in d_p with pressure. Amin et al. (waiting for citation) measured f_v, d_p, and Radius of gyration, R_g, in counterflow ethylene flames at pressures up to 5 bar. Vargas and Gülder (waiting for citation) used thermophoretic sampling and TEM analysis to measure d_p in methane diffusion flames at pressures up to 10 bar.

One of the reason morphological information is lacking in elevated pressure flames is diagnostic difficulties. Laser based techniques suffer from increased beam steering at elevated pressures [36], and physical access becomes more difficult. However, Time Resolved Laser Induced Incandescence (TiRe-LII) has the potential to measure soot concentrations and particle sizes at elevated pressures, as was done by Thomson et al. [41]. However, as noted in [41], the diagnostic suffers from uncertainties when

applied to flames at elevated pressures. Development of TiRe-LII for these conditions would help contribute to the measurement of morphological parameters.

Until now, most high-pressure research has focused on gaseous fuels, except for the early work of Schalla et al. [18], and the recent works of Mouis et al. [43, 44], Karataş et al. [45], and Zhou et al. [46, 47]. Mouis et al. [43, 44] doped small quantities of m-xylene, JP-8, and its surrogates into a diluted ethylene base flame, keeping total carbon flow rate constant. Doping in this manner allows the flame to experience roughly constant time-temperature history. Using a combination of LOSA, LII, and Laser Induced Fluorescence (LIF), they measured f_v and obtained qualitative aromatic concentrations. Karataş et al. [45] and Zhou et al. [46] both investigated flames of pre-vaporized n-heptane, up to 7 atm and 3 bar, respectively. Zhou et al. [47] also investigated the effect of molecular structure at elevated pressures. The investigated normal and cyclic hexane and hexanol at pressures up to 2 bar, finding cyclic and non-oxygenated produced more soot. All three groups note the difficulty in producing stable flames of pure pre-vaporized liquid fuels, which is especially problematic for multi-component fuels. If soot formation in practical devices is to be understood, more "real" fuels need to be investigated, and to higher pressures.

Additionally, as laminar coflow flames are commonly used for studies at elevated pressures, fundamental studies on the the coflow configuration itself could be useful. As most previous experiments have been scaled in pressure in flames established on a fixed geometry with constant mass flowrates [45], other scaling strategies could be investigated. It has been observed that coflow flames are more difficult to stabilize at elevated pressures [36, 48]. Defining the limits of this stability can facilitate future experiments. Additionally, coflow velocity has found to have stabilizing [49] and soot suppressing [50, 51] characteristics at atmospheric pressures, and these should be explored in an elevated pressure environment.

1.4 Objectives

The objectives of the current work can be summarized as follows:

- Characterize the stability, hydrodynamic suppression of soot, and scaling with pressure of the coflow configuration
- Add soot volume fraction and particle size to the existing International Sooting Flame workshop target flame data set.
- Improve the Time-Resolved Laser Induced Incandescence technique for high-pressure applications.
- Characterize the sooting tendency of liquid fuels at elevated pressures.

Chapters 2 and 3 introduce the experimental apparatus and methods of investigation. Chapters 4, 5, 6, and 7 discuss the individual investigations. Chapter 8 summarizes the findings from each investigation, and suggests paths of future work.

Chapter 2

Apparatus

This chapter describes the experimental facility in which the work is carried out. This includes the coflow burners, pressure vessel, and reactant delivery systems.

2.1 Coflow Burner

The coflow configuration is commonly used in soot studies. While coflow burners share the same basic features, there can be significant variation in the geometry and method of flow conditioning between coflow burners. Some shortcomings in the original burner used by the group were identified in the course of this work. The increased susceptibility of coflow flames to instability at elevated pressures necessitated redesigning of the burner. The coflow burner has undergone numerous iterations throughout the present work, and the final design is reported here.

2.1.1 Original Burner

The original burner, referred to as burner A, was designed by [52]. A diagram of the burner is shown in Fig. 2.1. The burner consists of a fuel nozzle with a 4 mm inside diameter which extends 5 mm beyond the exit plane of a 50 mm diameter coflow section. The knife-edged fuel nozzle tip tapers out to a 6.1 mm outside diameter where it meets the coflow exit plane. The coflow section contains 1.5 mm glass beads, and the fuel nozzle contains gauge-0000 steel wool 8 mm below the exit plane. Different iterations of burner A had either ceramic honeycomb, with 1 mm

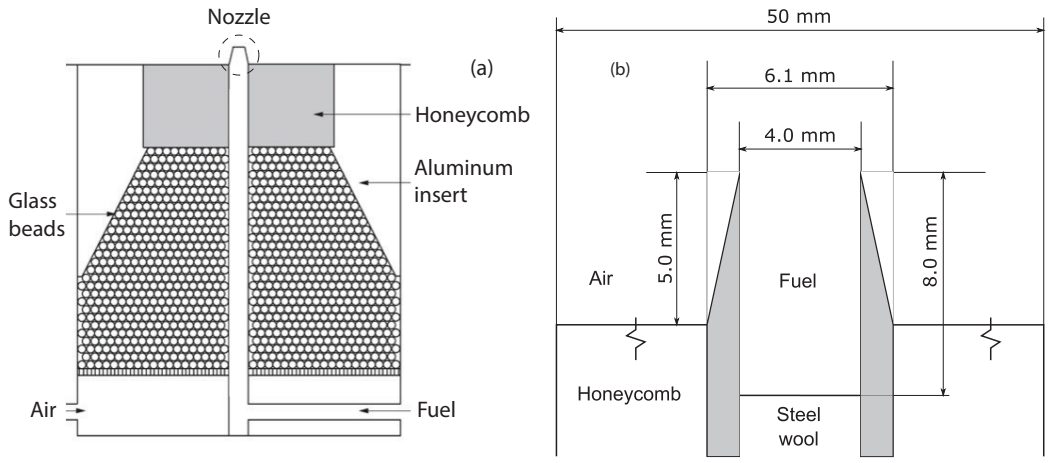

Figure 2.1: Burner A (a) geometry, (b) nozzle geometry.

channels, or aluminum foam, with 50 pores per inch, downstream of the glass beads. These restrictions evenly distribute the flow across the outlet area and limit acoustic interactions between the flame and pressure vessel. Due to several shortcomings with burner A, a new burner was designed.

Coflow burners are often used in conjunction with a "chimney" [30, 53]. Typically, these are cylinders placed around the burner to prevent ambient or in-vessel currents from disturbing the flame. The trade-off to using a chimney is limited access to the flame. Burner A used a pyrex cylinder as a chimney. Pyrex was used to provide optical access.

2.1.2 New Burner

A new coflow burner, shown in Fig. 2.2 and referred to as burner B, was designed and fabricated to meet several criteria. First, it was observed that repeated disassembly and reassembly of burner A resulted in degradation of the flow straightening materials. The result was the formation of gaps between the nozzle and coflow straightening material. This caused asymmetries in the flame, such as liftoff or tilt. Therefore, burner B was designed such that the entire nozzle/coflow assembly could be removed together. Additionally, the modular design allows for different configurations of flow

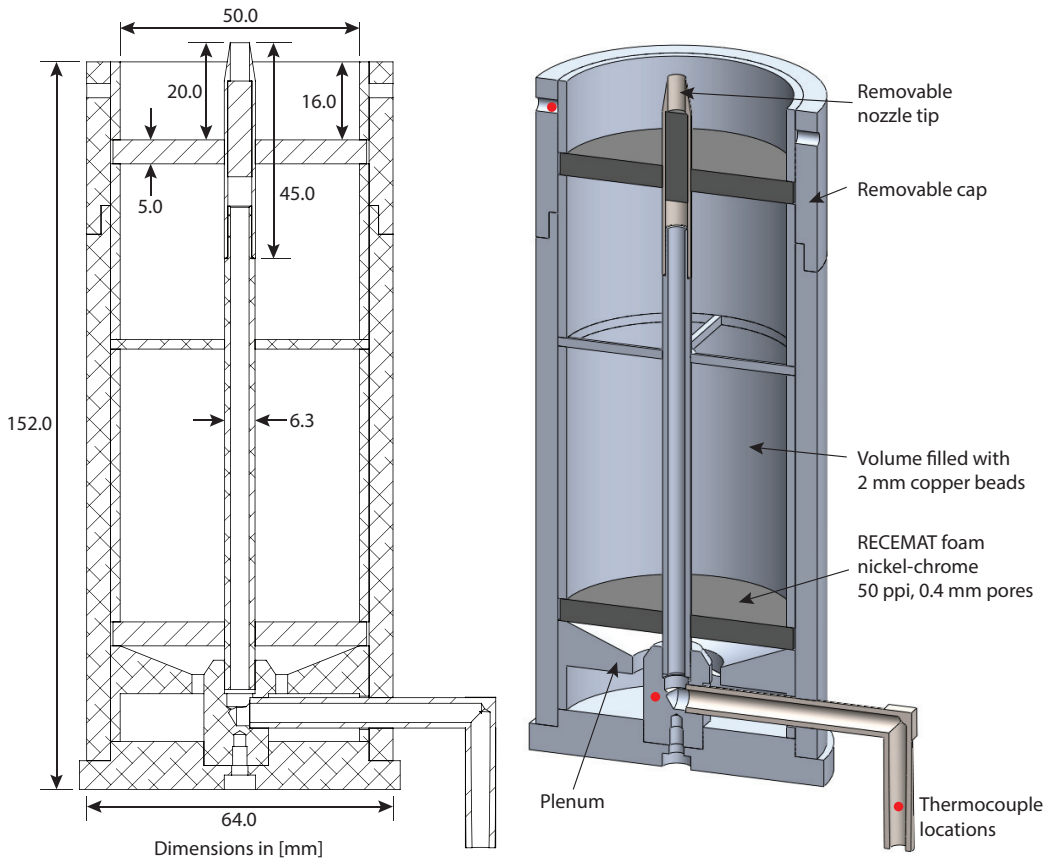

Figure 2.2: Burner B geometry with tapered nozzle.

straighteners in the coflow section to be utilized with minimal modification. Present experiments utilized two 5 mm thick RECEMAT nickel-chrome foam disks, with 50 0.4 mm pores per inch. Due to the way the central nozzle was tapped into the base of burner A, the nozzle was tilted slightly relative to the coflow section. Burner B was designed with nozzle supports to keep the nozzle centered within the coflow. Discussion with numerical modelers revealed the desire for alternate nozzle geometries, for example, without tapering. Additionally, past research has shown the impact nozzle material can have on flame temperatures and soot volume fraction [54]. Therefore, burner B was designed such that the nozzle tip can be replaced, allowing different geometries or materials to be used with minimal burner modification necessary. To provide a more uniform distribution of flow, burner B features dual coflow entry ports, on opposite sides of the burner 90° relative to the fuel entry point, an entry

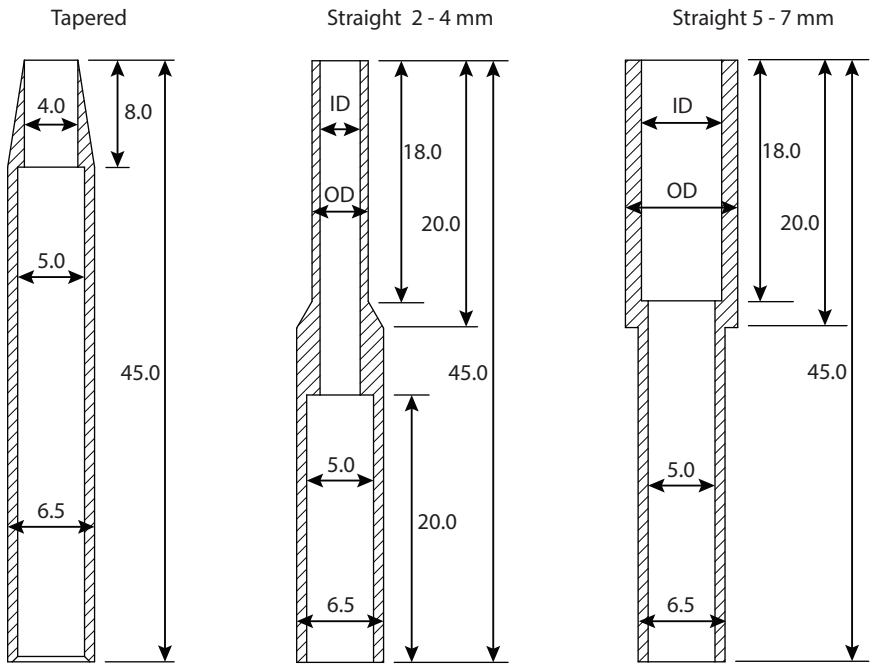

Figure 2.3: Burner B nozzle dimensions [mm].

plenum, and is much longer compared to burner A. Finally, the new burner was also designed specifically with the use of liquid fuels in mind. As burner heating would be necessary to pre-vaporize liquids before exiting the burner, thermocouples are placed in key locations to monitor temperature, and the volume is filled with 2 mm copper beads. The beads act both as a flow conditioner, and as a conductive medium for a uniform temperature profile.

Present experiments are conducted using stainless steel nozzles of similar, though varying dimensions. Figure 2.3 shows the dimensions of the nozzles. The variable dimensions shown in 2.3 are defined in Table 2.1, along with nozzle wall thickness. Burner B configurations will be referred to with the nozzle specified. For example, burner B3 is burner B with the 3 mm ID nozzle. Previous experiments used tapered nozzles [36, 38, 39, 55, 56], thought to minimize heat transfer from the flame to the nozzle. A tapered nozzle, B4t, was also designed for the new burner. However, straight nozzles are easier to represent in a computational domain. To maintain a self-similar geometry, straight nozzle wall thickness was selected such that wall/ID is

constant (0.2), with this constant chosen based on the smallest thickness that could be machined for the 2 mm nozzle. The "step" inside nozzle B4t is to provide a resting surface for 20 mm thick RECEMAT nickel-chrome foam. Straight nozzles had no such foam, and length was chosen such that flows would be fully developed at the investigated flowrates.

Table 2.1: Burner B nozzle variable dimensions.

Designation	ID [mm]	OD [mm]	wall [mm]
B2	2.0	2.8	0.4
B3	3.0	4.2	0.6
B4	4.0	5.6	0.8
B4t	4.0	6.5	*
B5	5.0	7.0	1.0
B6	6.0	8.4	1.2
B7	7.0	9.8	1.4

A new chimney, shown in Fig. 2.4, was also designed to accommodate burner B. The design is similar to that of Thomson [57]. The chimney body is fabricated from aluminum. It minimizes the dead space between the outside edge of the coflow section, and the inside wall of the chimney. Three faces of the chimney are designed to fit custom flat windows, to allow optical access, which can be coated with various Anti-Reflective (AR) coatings. Separate windows were purchased with AR coatings for visible and infrared wavelengths. The fourth side of the chimney is slotted for igniter, sampling probe, and thermocouple access. To prevent air entrainment though this slot, which was particularly problematic when the burner was heated, a "door" was designed which could be closed when the slot was not in use.

2.2 Pressure Vessel

The cost of building a pressure vessel is one of the major barriers responsible for the lack of high pressure soot information. A vessel, shown in Fig. 7.1(a), is used to

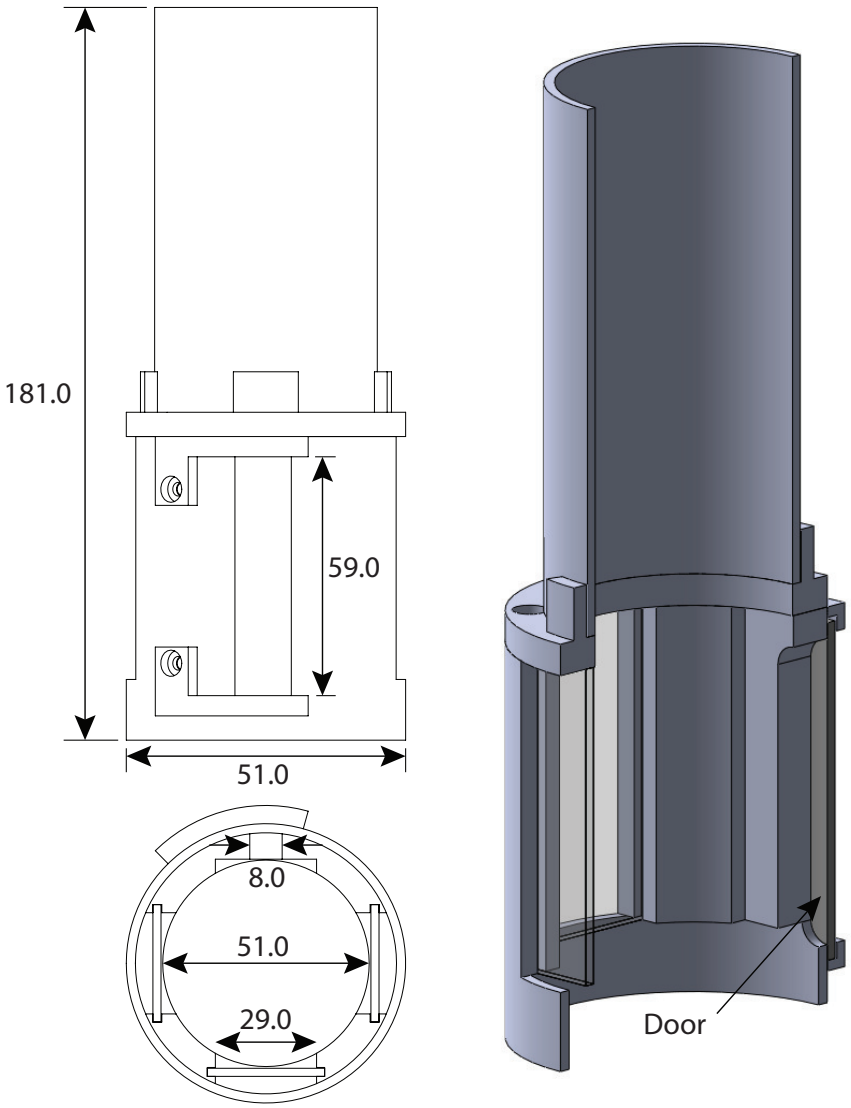

Figure 2.4: Chimney for burner B, with dimensions [mm].

simulate an elevated pressure environment. The vessel was originally designed and constructed by Li [58], and has since been modified and improved by subsequent researchers [52, 59]. The vessel is constructed of AMSE/ANSI B16.5 class 300 and 400 flanges, and is rated for continuous operation at 45 bar. The vessel is constructed with an outer layer which can serve as a water jacket for vessel cooling. Several improvement have been made for the present work:

The original optical window assembles, which included two class 400 flanges and one optical window, were replaced with a single-flange design. In the original design,

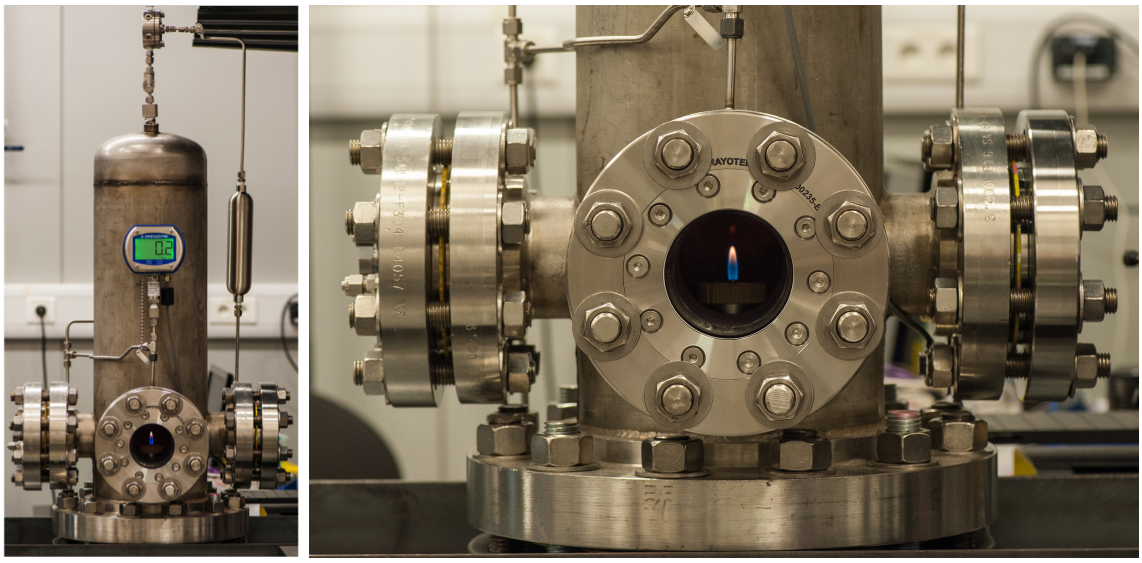

(a) Pressure vessel (b) Optical access

Figure 2.5: Pressure Vessel.

the clear aperture was approximately 50 mm, and vacuum grease was necessary to provide sealing. This sealing method required constant maintenance, which involved removing the windows, cleaning them with solvent, and resealing them. In addition to providing a larger clear aperture (75 mm diameter), the new window assembly uses a gasket seal, without the need to vacuum grease. Two sets of windows were purchased. One set has an AR coating for visible wavelengths, and the other is uncoated.

The entire burner assembly was mounted on a new two-axis translation stage. Combined with the existing axial translation capabilities, this allows full translation control. A custom Sigma-Koki two-axis translation device was used, providing 12 mm travel in each direction. Maximum translation is limited, as the inside diameter of the vessel is only 146 mm. The existing axial translation stage (Ultra Motion 3B.125SM172B/4) allows for 50 mm of translation.

In order to accommodate heated reactants entering the vessel, new delivery ports were designed. To limit heat loss to the base flange, teflon insulation inserts were fabricated to fit into the base flange. Inserts are held in place with a bracket bolted to the base flange. The vessel was also modified to accommodate liquid fuels (Section

2.3.2).

Pressure control in the original design was a tedious process. A needle valve, placed at the vessel outlet, was slowly closed to build pressure inside the vessel. If the valve was closed too quickly, the flame could extinguish. Additionally, the valve could heat up or accumulate soot during operation, requiring frequent adjustment to maintain a desired pressure. This valve was replaced with an electronically controlled Back-Pressure Regulator (BPR) system. The BPR system consists of a dome-loaded BPR, and an electronically controlled pressure regulator. The desired vessel pressure is set through a LabView program. This controls the outlet pressure of the pressure regulator, and hence, the pressure on the dome-side of the BPR. Exhaust flow is then regulated such that the vessel pressure matches the dome pressure. A damping volume was added downstream (see Fig. 2.6) of the electronic regulator to allow more precise control.

2.3 Experimental Control

2.3.1 Gas Delivery

A diagram of the gas delivery system is shown in Fig. 2.6. Gaseous fuel, diluent, and oxidizer were controlled using Brooks thermal Mass Flow Controllers (MFCs). Thermal MFCs measure the energy needed to increase the temperature of the flowing gas by a known amount, and by calibration, this can be related to the mass flowrate. Conversion or calibration factors can be used when the process gas is different than the calibrated gas. These factors are the ratios of molar specific heat of the gases at operating pressure and temperature. Since operating pressure affects these factors, and hence the accuracy of the MFC, a constant upstream and downstream pressure must be maintained. To accomplish this, the upstream pressure is controlled by a pressure regulator, and the downstream pressure is controlled by a BPR, similar to that used for vessel pressure control (Section 2.2).

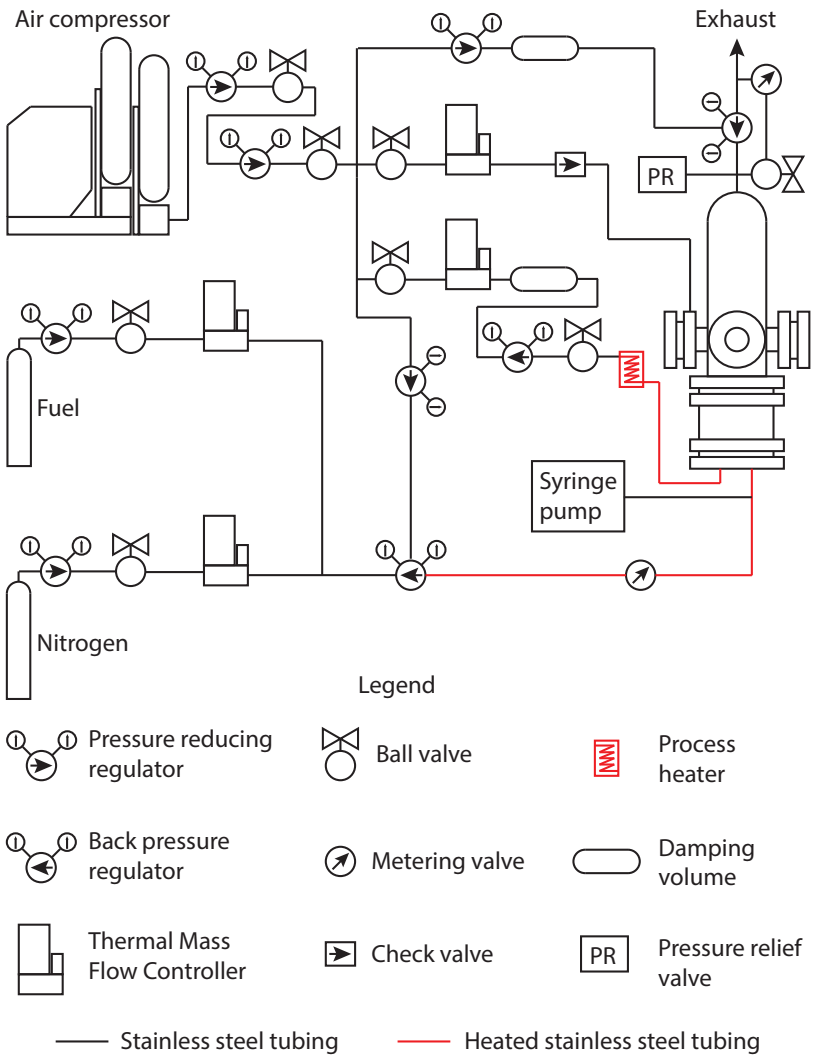

Figure 2.6: Gas delivery system.

Previously, four coupled cylinders were used to provide air for this experiment. Due to the frequency of refills necessary, a high pressure compressor was purchased. A Bauer mini-verticus III (MV-I 120-4-3), shown in Fig. 2.7, is able to provide up to 170 standard liters per minute of air at 270 bar. The outlet of the compressor is attached to four 80 L cylinders for air storage when the compressor is not running. The compressor automatically runs as necessary to maintain a minimum pressure in these cylinders. The outlet of the compressor system is stepped down in pressure in two stages. The first reduces the pressure to 100 bar, the second reduces the pressure to the calibration pressure of the MFCs, 35 bar. Reducing pressure in two steps

Figure 2.7: Bauer MV-I 120-4-3 air compressor.

prevents freezing of the pressure regulator, which occurs when the pressure drop is too large at high flowrates.

Air is used for three purposes in this experiment: 1) to provide air for the coflow, 2) to provide air to remove condensation from the vessel windows, and 3) to provide the setpoint of dome-loaded BPRs. The pressure vessel exhaust and the nozzle flow BPRs are both dome-loaded. One Brooks 5850 thermal MFC is used to provide air to the vessel windows. A check valve downstream of this MFC prevents flow out of the vessel. One Brooks 5850 thermal MFC is used to control coflow rate. Downstream of the coflow MFC, a stainless steel tank is used to provide a damping volume. This limits oscillations due to acoustic coupling with the pressure vessel. Coflow air then passes through a 1500 W process heater, which is able to heat the coflow up to 200 °C. The coflow stream temperature is maintained as it passes to the vessel with Unique Heated Products sampling line, which is able to heat flows to 300 °C.

Fuel and diluent streams are each controlled by Brooks 5853 thermal MFCs, and are mixed downstream of the MFCs. The nozzle mixture passes through an additional metering valve to dampen oscillations due to acoustic coupling with the pressure vessel. A Unique Heated Products sampling line is used to preheat the nozzle mixture before it enters the vessel. Details of liquid fuel delivery are given in Section 2.3.2.

2.3.2 Liquid Fuel Delivery

Liquid fuels are often pre-vaporized for use in coflow flames. In order to prevent liquid fuels from condensing in elevated pressure environments, they need to be sufficiently heated or diluted with carrier gas. For the low flowrates characteristic of these flames, heat loss is major concern. At temperatures appropriate for vaporization, heat loss can be greater than the enthalpy carried by the heated fuel. Therefore, the entire liquid fuel delivery system must be heated post vaporization. As sufficient heating or insulation was not possible in the section of tubing passing through the base flange, vaporization had to be carried out within the vessel. To accomplish this, a liquid fuel injector was designed, and is shown in Fig. 2.8. It consists of a 1/16" SS tube concentric to the 1/4" SS gas delivery tube. The tip of the 1/16" tube is embedded in an aluminum foam. The foam wicks liquid fuel from the 1/16" tube out onto a larger surface area for vaporization. Liquid fuels are fed to this 1/16" tube using a Harvard Apparatus PHD2000 syringe pump. A gaseous fuel/diluent mixture enters the injector in the location shown in Fig. 2.8.

All tubing inside the vessel downstream of the teflon insert is heated with rope heaters, and the temperature is monitored with thermocouples. The location of the injector thermocouple is indicated in Fig. 2.8. To prevent condensation within the coflow burner, it is heated externally and insulated. The aluminum body and copper beads ensure minimal thermal gradient within the burner. It has been tested at up to 250 °C. However, increasing the burner temperature causes seemingly random instabilities in the flame.

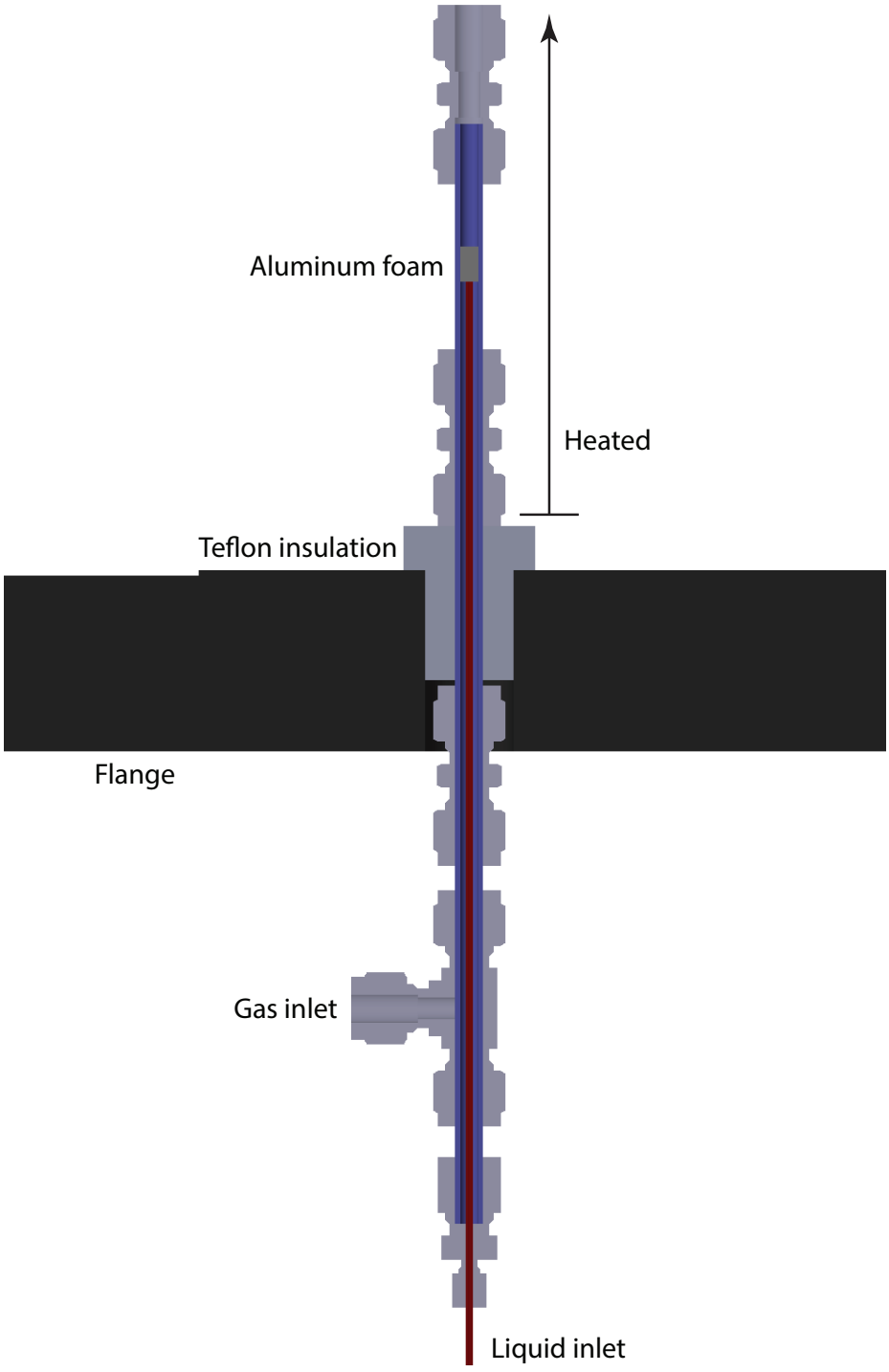

Figure 2.8: Liquid fuel injector.

Chapter 3

Diagnostics

This chapter describes the diagnostic methods used in these investigations. The theory behind each method is first presented, followed by details of the setup used. Some details, including analysis of the uncertainties, are specific to individual investigations, and are presented with the results in Chapters 4, 5, 6, and 7.

3.1 Laser Extinction and Scattering

3.1.1 Theory

LES is a commonly used technique for measuring soot concentrations and particle size [53, 60–63]. Extinction measurements allow for determination of soot concentrations, while scattering measurement (usually simultaneously) gives particle size information.

The intensity of a light source before (I_0) and after (I) passing through an absorbing medium, such as a sooty flame, is measured. Beer's law

$$\tau = \frac{I}{I_0} = \exp(-\kappa_e L) \tag{3.1}$$

relates the transmissivity of light, τ, to the integral of the local extinction coefficient, κ_e, over the path length, L. Path averaged soot volume fraction, $f_{v,a}$, can be found using Rayleigh-Debye-Gans (RDG) theory

$$f_{v,a} = \frac{1}{L}\frac{-\ln(\tau)\lambda}{6\pi(1+\rho_{sa})E(m)} \tag{3.2}$$

whereλ is the wavelength of light, ρ_{sa} is the ratio of scattering (κ_s) and absorption (κ_a) coefficients, m is the soot refractive index, and $E(m)$ is the imaginary soot refractive index function. $E(m)$ can be found from

$$E(m) = -\mathrm{Im}\left(\frac{m^2-1}{m^2+2}\right) \tag{3.3}$$

Assuming extinction occurs only within the axisymmetric flame, local κ_e can be determined by Abel inversion (Section 3.5). The local extinction coefficient is similarly related to soot volume fraction, f_v

$$f_v = \frac{\kappa_e \lambda}{6\pi(1+\rho_{sa})E(m)} = \frac{\kappa_a \lambda}{6\pi E(m)} \tag{3.4}$$

The optical properties of soot (m, ρ_{sa}) are not well known. In general, they are functions of morphology, particle diameter, D, and λ, and will vary throughout a flame due to differences in residence time, temperature, and chemistry [64].

By measuring the intensity of vertically polarized light scattered from a vertically polarized incident beam, Q_{vv}, and assuming the particles are within the Rayleigh regime ($D \ll \lambda$), an average weighted primary particle diameter can be found from the sixth to third moment ratio of particle probability functions [53, 60] and is given by

$$D_{63} = \lambda\left(\frac{4}{\pi^2}\frac{E(m)}{F(m)}\frac{Q_{vv}}{\kappa_a}\right)^{\frac{1}{3}} \tag{3.5}$$

where $F(m)$ is the real refractive index function, which can be found from

$$F(m) = \left|\frac{m^2-1}{m^2+2}\right|^2 \tag{3.6}$$

In addition to being biased to larger particles, a major limitation of this Rayleigh analysis is the neglecting of aggregation, thereby assuming that light is scattered by individual soot spherules. Research has shown that this limitation results in large

overestimates of primary particle diameters [63]. For a more representative analysis, Rayleigh-Debye-Gans Polydisperse Fractal Aggregates (RDG-PFA) theory is used, assuming $\pi D|m-1| \ll \lambda$. The modulus of the scattering wave vector, q, can be found from $q = 2k\sin\theta/2$, where $k = 2\pi/\lambda$. Its inverse, q^{-1}, represents a length scale of the scattering measurements [65]. The Guinier regime corresponds to instances where this resolution is larger than the radius of gyration of the aggregate, R_g. In the power-law regime, $qR_g > 1$, and an average primary particle diameter can be calculated from

$$d_p = \frac{\lambda}{\pi}\left(4\pi\frac{E(m)}{F(m)}\frac{Q_{vv}}{\kappa_a}\frac{(q/k)^{D_f}}{k_f}\right)^{\frac{1}{3-D_f}} \tag{3.7}$$

While more representative of soot physics, RDG-PFA analysis requires additional knowledge of the aggregate; namely, fractal prefactor, k_f, and fractal dimension, D_f. Since scattering intensity scales with $(qR_g)^2$ in the Guinier regime and with q^{-D_f} in the power-law regime, D_f, R_g (and hence k_f) can be inferred through measurements over a range of q. This is typically accomplished by scattering measurements at multiple angles.

3.1.2 Setup

The layout of the LES setup can be found in Fig. 3.1. The laser, optics, and detectors are mounted on motorized linear translation stages, which allowed the beam to be horizontally translated relative to the flame. The stepper motor inside the vessel supports the burner and translates it vertically. A 21 mW Helium-Neon (HeNe) laser produces a vertically polarized beam at 632.8 nm. The 0.7 mm beam is expanded to 4 mm before focusing to reduce the beam focal waist to 100 μm and reduce the effect of variations in window transmissivity. A portion of the beam is sampled to provide continuous reference intensity, and a quartz diffuser plate mounted on the photodiode detector limits the effect of spatial variation in detection. After being focused through the pressure vessel, the transmitted beam passes through a 50 mm diameter lens into

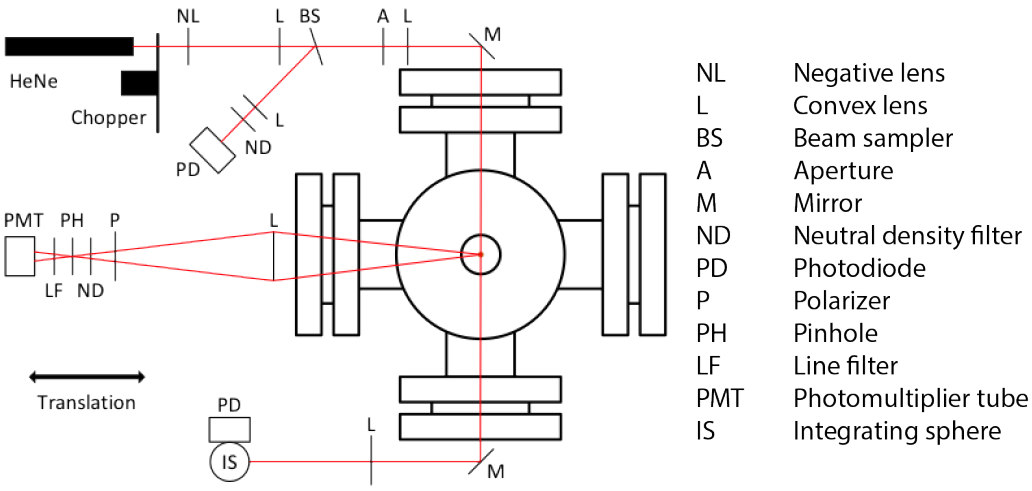

Figure 3.1: Layout of the LES setup.

an integrating sphere, which are critical to reduce the effect of beam steering. A photodiode mounted to the integrating sphere measures the transmission intensity. In order to relate reference laser intensity to local intensity in the pressure vessel, a point-by-point transmission measurement is made at each horizontal position of each window.

Due to limitations in optical access, scattering is only collected at one angle. A 50 mm diameter lens collects light scattered 90° relative to the beam, with a solid angle of collection of 85×10^{-3} sr. Scattered light is focused through a polarizer onto a 150 μm pinhole and line filter (632.8±1.0 nm) mounted to a Photomultiplier Tube (PMT). Neutral density filters are used as needed, and linearity of the PMT is found to be within 10%. The PMT is mounted to a 3-axis manual translation stage for precise positioning. The scattering signal is corrected for extinction and signal trapping, and then correlated to Q_{vv} using the Rayleigh scattering of two gases with known scattering cross-sections, propane and nitrogen [53]. Three lock-in amplifiers measure the signal from the two photodiodes and one PMT.

3.2 Diffuse-Light 2D Line of Sight Attenuation

3.2.1 Theory

Diffuse-light 2D line-of-sight attenuation, or Diffuse Light Extinction (DLE), is based on the same underlying theory as LE (Section 3.1). The extinction caused by an absorbing medium (soot), can be related to its concentration (equation 3.4). Frequently, LE is extended to two dimensions by using a collimated light source. For example, a laser beam could be expanded and recollimated. A camera can then be used to measure transmissivity in a 2D field simultaneously. All optical elements, including the windows of a pressure vessel, will have small spatial variations in transmissivity and reflectivity. This difference in transmissivity may only be a few percent or less. For most applications, the only consequence of this is slightly diminished intensity of laser propagation or light emission. In LE, the total extinction from flames with low optical thickness may only be a few percent. As such, measurement of the background transmissivity without the absorbing medium present is necessary, and often sufficient, for accurate extinction measurements at atmospheric pressures.

In the case of flames at elevated pressures, density gradients in the measurement medium cause a lensing effect, which diverts the beam from its path in the absence of the flame. Each chord of a collimated beam will then pass through different points on each optic with and without the flame present. As a result, the beam experiences different levels of transmissivity with and without a flame present, from the optics alone. Replacing the collimated light source with a diffuse one can alleviate this problem [66–68].

In DLE [66], a diffuse light source is used instead of a collimated one. An ideal diffuse light source will be Lambertian, radiating with the same power per unit solid angle when viewed from any angle. The port of an illuminated integrating sphere can approximate a Lambertian reflector. This port is imaged onto the center plane of the

absorbing medium, or flame. This image is then collected by a focusing lens, and re-imaged onto the surface of a Charge-Coupled Device (CCD). In the presence of beam steering, the paths of individual light rays will change. However, the image of a single point on the image plane is comprised of light rays from the entire diffuse source, and all of these light rays are of equal intensity. Thus, as long as the collection lens is overfilled, any change in transmissivity from one ray will ideally be compensated by another. To ensure the lens is overfilled, the f-number of the collection lens should be higher than the imaging lens. The trade-off of using a diffuse source is that the attenuation is no longer truly line of sight. This can also be mitigated by ensuring a high f-number on the collection side. However, a higher f-number increases the likelihood of steered beams completely missing the collection optics.

3.2.2 Setup

The setup for DLE is shown in Fig. 3.2. An LED lamp, with a color temperature of 6500 K, is used to illuminate a 2 inch integrating sphere. The integrating sphere removes spatial information from the light source, producing a Lambertian distribution of intensity. A pair of achromatic lenses, of 50 mm diameter and focal lengths 300 mm and 100 m, image the 12 mm exit port onto the center plane of the burner, with a magnification of 3. This magnification is chosen to fully illuminate the detector. A pair of achromatic lenses, of 50 mm diameter (apertured to 12.5 mm to increase f-number) and focal lengths of 750 mm, re-image the magnified light source onto a PIXIS 400F CCD camera. The CCD is 26 mm $\times$ 8 mm (1340 $\times$ 400 pixels of 20 μm). A bandpass filter of 400 nm $\pm$20 nm is mounted to the camera. Exposure time and gain of the CCD is chosen to maximize dynamic range without saturating. The vessel and chimney windows have AR coatings effective for visible wavelengths.

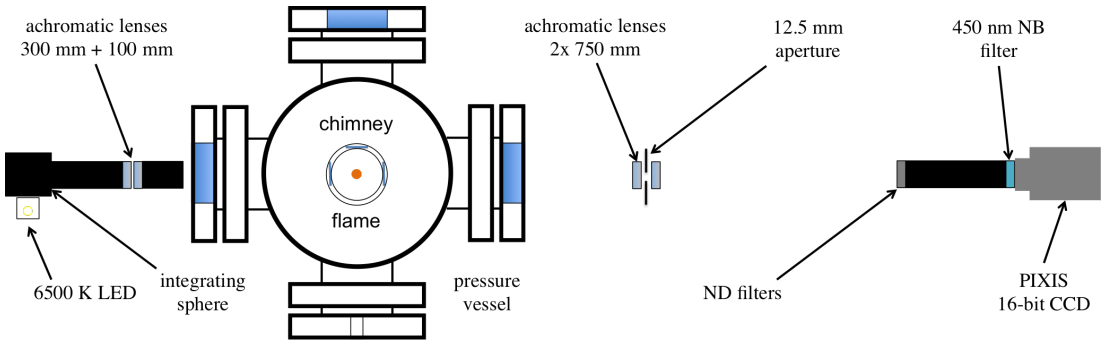

Figure 3.2: Layout of the DLE setup.

3.3 Two-Color Time Resolved Laser Induced Incandescence

3.3.1 Theory

In LII, a high-energy laser pulse is used to superheat soot to high temperatures ($\geq$ 2500 K). The resulting incandescence of this superheated soot can be distinguished from background flame emissions, and with calibration, can be related to the concentration of soot in the probe volume. As the soot cools through a number of processes following the laser pulse, the incandescence signal intensity decays. As decay rate is dependent on soot surface area, it can be related to soot particle size. To accomplish this, numerical models which solve an energy balance on soot particles are typically used to predict the decay rate for a range of particle sizes under the experimental conditions. The decay rate that best matches the observed decay is used to determine particle size.

A summary of current LII models is given in [69]. These models seek to solve the coupled differential equations for changes in soot particle size and temperature with time. Though the specifics of each model vary, in general, the energy balance can be written as

$$\frac{\mathrm{d}U_{internal}}{\mathrm{d}t} = \dot{Q}_{Absorption} - \dot{Q}_{Conduction} - \dot{Q}_{Radiation} - \dot{Q}_{Sublimation} - \dot{Q}_{Thermionic} + \dot{Q}_{Oxidation} \tag{3.8}$$

where $U_{internal}$ is the internal energy of a particle, and $\dot{Q}$ represents the energy lost or gained through various phenomena. The change in internal energy can be expressed as

$$\frac{\mathrm{d}U_{internal}}{\mathrm{d}t} = \rho_s c_{p,s} \frac{\pi}{6} D^3 \frac{\mathrm{d}T_p}{\mathrm{d}t} \tag{3.9}$$

where ρ_s and $c_{p,s}$ are the density and specific heat of soot, D is the particle diameter, and T is the particle temperature. The energy absorbed from the laser pulse can be expressed as

$$\dot{Q}_{Absorption} = \frac{\pi^2 D^3 E(m)}{\lambda} \frac{F q(t)}{q_1} \tag{3.10}$$

where F is the laser fluence, $q(t)$ is the temporal profile normalized to 1, and q_1 is a constant which normalizes the total energy to 1.

Conduction is the most dominant mode of heat loss, particularly at elevated pressures. At atmospheric pressures, the mean free path is much greater than the particle size, while at elevated pressures, this may not be the case. As such, a conduction model which is accurate in the free molecular flow, continuum, and transition regimes is required. The Fuchs model [70] has been found to be the most accurate for these conditions. In the Fuchs model, heat conduction is separated into two parts; heat is conducted in the free molecular flow regime from the particle to a limiting sphere surrounding the particle

$$\dot{Q}_{Conduction} = \alpha_T \pi D^2 \frac{P}{8} \sqrt{\frac{8 k_B T_\delta}{\pi W_g}} \frac{\gamma^* + 1}{\gamma^* - 1} \left(\frac{T_p}{T_\delta} - 1 \right) \tag{3.11}$$

the same heat is also conducted from this sphere to the surrounding gas in a continuum regime

$$\dot{Q}_{Conduction} = 4\pi \left(\frac{D}{2} + \delta \right) \int_{T_g}^{T_\delta} k_g \mathrm{d}T \tag{3.12}$$

where α_T is the thermal accommodation coefficient, P is the pressure, k_B is the Boltzmann constant, W_g is the average mass of the gas molecules, γ^* is the mean specific

heat ratio, T_p is the particle temperature, T_δ is the limiting sphere temperature, and k_g is the thermal conductivity [70]. Equations 3.11 and 3.12 are solved iteratively to determine T_δ, then $\dot{Q}_{Conduction}$ can be solved.

The energy lost due to radiation is typically negligible compared to conduction, but is found by integrating the Planck distribution

$$\dot{Q}_{Radiation} = \pi D^2 \int_0^\infty \epsilon_\lambda \frac{2\pi h c^2}{\lambda'^5 \left[\exp\left(\frac{hc}{\lambda' k_B T}\right) - 1\right]} \mathrm{d}\lambda' \tag{3.13}$$

where ϵ_λ is the wavelength dependent emissivity of soot, h and c are the Planck and speed of light constants, respectively. At sufficiently high fluences, soot will sublimate from the solid phase to the gas phase, resulting in loss of energy and mass

$$\dot{Q}_{Sublimation} = -\frac{\triangle H_v}{W_v} \left(\frac{\mathrm{d}M}{\mathrm{d}t}\right)_{\text{sublimation}} \tag{3.14}$$

$$\left(\frac{\mathrm{d}M}{\mathrm{d}t}\right)_{\text{sublimation}} = \frac{-\pi D^2 W_v \alpha_m \rho_v}{RT} \left(\frac{RT}{2\pi W_v}\right)^{0.5} \tag{3.15}$$

where $\triangle H_v$ is the enthalpy of formation of carbon clusters, W_v is the molecular weight of the sublimed clusters, M is the particle mass, α_m is the mass accommodation coefficient, R is the Universal gas constant, and ρ_v is the average saturation partial pressure of the sublimed cluster. At high fluences, sublimation is the dominant mode of energy and mass loss, though these processes are not well understood [71]. The internal energy of particles may increase due to oxidation, and the energy gained and mass lost can be expressed as

$$\dot{Q}_{Oxidation} = \frac{(\triangle H_{ox} + \alpha_T C_{CO} T)}{W_1} \left(\frac{\mathrm{d}M}{\mathrm{d}t}\right)_{\text{oxidation}} \tag{3.16}$$

$$\left(\frac{\mathrm{d}M}{\mathrm{d}t}\right)_{\text{oxidation}} = \frac{-\pi D^2 W_1 2 k_{ox}}{N_A} \tag{3.17}$$

where $\triangle H_{ox}$ is the enthalpy of reaction, C_{CO} is the molar heat capacity of CO, W_1 is the molecular weight of carbon, k_{ox} is the reaction of oxygen at the surface, and N_A is Avogadro's number. Finally, energy can be lost to thermally ejected electrons

$$\dot{Q}_{Thermionic} = \frac{4\phi m_e(\pi D k_B T)^2}{h^3}\exp\left(\frac{-\phi}{k_B T}\right) \tag{3.18}$$

where ϕ is the work function, and m_e is the electron mass. The above energy balance is coupled to the mass balance,

$$\frac{\mathrm{d}M}{\mathrm{d}t} = \left(\frac{\mathrm{d}M}{\mathrm{d}t}\right)_{\text{sublimation}} + \left(\frac{\mathrm{d}M}{\mathrm{d}t}\right)_{\text{oxidation}} \tag{3.19}$$

In order to accurately model the decay rate of soot particles, the temperature of the soot and surrounding gas must be known. In particular, the peak temperature of the soot after the laser pulse, and the initial temperature of the soot before heating. To determine soot temperature, two-color pyrometry can be used. Soot spectral emissions are related to the Planck distribution (see Equation 3.13). The emission detected is given by

$$S = \Omega\pi D^2 \int_\lambda \epsilon_\lambda \frac{2\pi hc^2}{\lambda^5\left[\exp\left(\frac{hc}{\lambda k_B T}\right) - 1\right]}\Sigma_\lambda \mathrm{d}\lambda \tag{3.20}$$

where Ω is the solid angle of detection, and Σ_λ is the spectral detector efficiency [71]. The spectral emissivity of soot can be written as

$$\epsilon_\lambda = \frac{4\pi DE(m)}{\lambda} \tag{3.21}$$

Therefore, by measuring emission of the soot at two different wavelengths and taking the ratio of Equation 3.20, all terms in Equation 3.20 are known or cancel, except T and Σ_λ. If calibration of $\frac{\Sigma_{\lambda,1}}{\Sigma_{\lambda,2}}$ is done with a source of known emission, the temperature

can be determined.

3.3.2 Setup

A diagram of the two-color TiRe-LII setup is shown in Fig. 3.3. The optics are arranged to accommodate the use of two Neodymium-doped Yttrium Aluminum Garnet (Nd:YAG) lasers. A Quantel Q-Smart 850 Nd:YAG outputs a 1 cm diameter beam, with a wavelength of 1064 nm, at 10 Hz. The beam is attenuated with a LaserOptik AVACS attenuator. A custom Ekspla NL909-5-SH Nd:YAG laser outputs a 1 cm diameter beam, with a wavelength of 1064 nm, at 5 Hz. The beam is attenuated with the combination of a Glan-laser polarizing cube and a 1/2 waveplate mounted on a rotation stage. The fundamental 1064 nm beams are used to limit interference of large molecules absorbing or fluorescing from the use of shorter wavelengths. The beams of both lasers are directed with dichroic mirrors towards a 1 mm aperture counterbored into an aluminum block. A relay lens, of focal length 150 mm, is placed between this aperture and the burner axis, a distance of $2f$ from each. This ensures each beam passes through the same point of the flame. A power meter placed after this aperture is used to measure pulse energy. A fast photodiode (New Focus model 1454, 18.5 ps rise time) is placed beyond the flame to measure the temporal profile of each pulse, or any indication of significant changes in soot absorption. A beam profiler (Gentec-EO Beamage) is placed inside the vessel, coinciding with the burner axis, to measure beam spatial profiles. Chimney windows have AR coatings effective for 1064 nm. Vessel windows along the beam path are uncoated, while the window on the detector side has an AR coating effective for visible wavelengths.

The incandescence signal from the flame is collected 90° relative to the beam path. A pair of 750 mm focal length acromatic lenses collect the light, and form an image of the flame on an adjustable aperture. This aperture is mounted to a sealed detector box containing two PMTs (Hamamatsu models R9880U-210 and R9880U-20, MEA

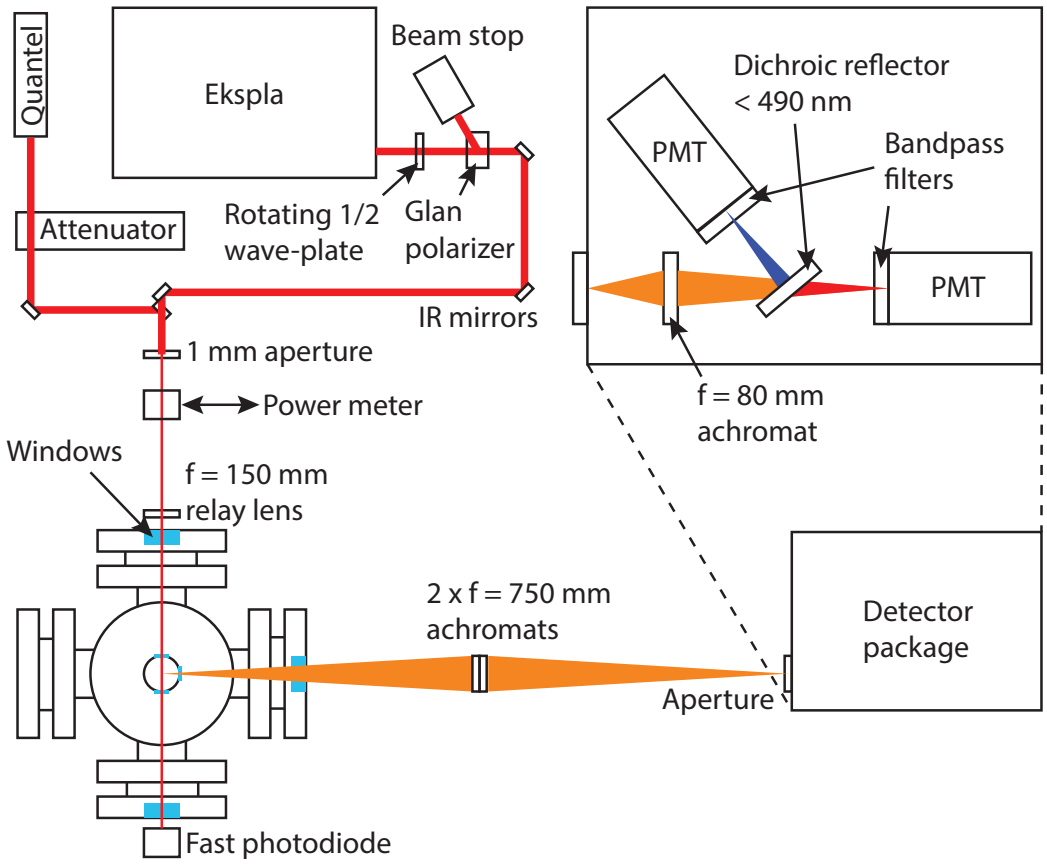

Figure 3.3: Layout of the two-color TiRe-LII.

1030V8DA1100 amplifiers, 0.75 ns combined rise time). The aperture is adjusted to select the probe volume, and the box is positioned vertically to align with the laser, and horizontally to chose the probe location. The detector box makes the detector package portable, and shields the PMTs from background light. Inside the box, a dichroic mirror reflects wavelengths less than 490 nm towards PMT1. The remaining light passes through the dichroic mirror to PMT2. A bandpass filter (Semrock) of 400 $\pm$ 20 nm is placed in front of PMT1, and a bandpass filter (Semrock) of 655 $\pm$ 20 nm is placed in front of PMT2. An achromatic lens of 80 mm focal length focuses light passing through the aperture onto both PMTs. This ensures a constant diameter of light incident on the PMT sensors, regardless of aperture size. All lenses are 50 mm diameter. The output of the PMTs and photodiodes is read by a Keysight DSO-S 804A oscilloscope with a 10 GSa/s sampling rate.

A Gamma Scientific RS-10D calibration light source, with known spectral radiance, is used to calibrate the detectors. Since it can not be fit inside the vessel, it is placed between the vessel and the 750 mm relay lenses. An identical chimney and vessel window are placed between it and the detectors. As the ratio of spectral radiance at the chosen wavelengths is known, the ratio of detector collection efficiencies can be determined. The theoretical ratio of emission intensities for soot is calculated for a range of temperatures to produce a look-up table. This table is interpolated with the ratio measured during experiments to determine the soot temperature. TiRe-LII signals are simulated by the KAUST LII simulator (reference).

3.4 Constant Temperature Anemometry

3.4.1 Theory

In hot-wire anemometry, a bridge and amplifier circuit is used to heat a fine sensor. This sensor, whose resistance is a function of temperature, is one leg of the circuit bridge. As a fluid passes over this sensor, the cooling effect must be balanced by a change in voltage or current in the other leg of the bridge. With properties of the fluid known, this change can be related to the velocity or temperature of the fluid. Anemometers can be operated at Constant Current (CCA), Constant Voltage (CVA), or Constant Temperature Anemometry (CTA). These techniques offer the advantage of high response rate and frequency [72].

CTA can be used to measure the velocity in non-reacting flows of homogeneous composition. In a CTA circuit, the bridge voltage is adjusted to maintain a constant temperature in the sensor. This voltage change, after calibration, is related to the velocity of the fluid. As this technique can only measure the velocity normal to the sensor, either multiple sensors or measurements are needed at orthogonal angles to resolve the velocity vector.

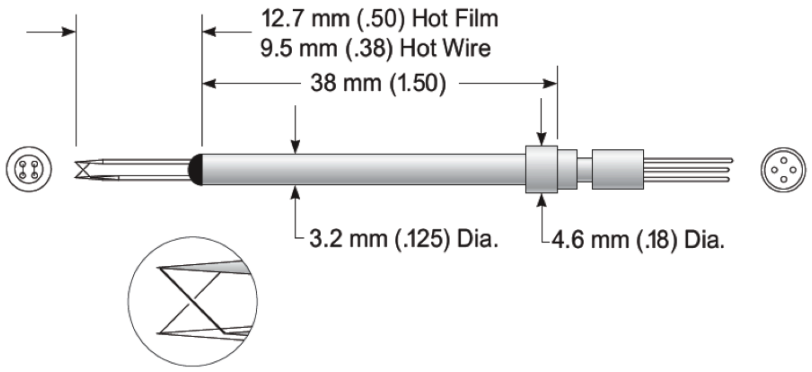

Figure 3.4: TSI model 1241-T1.5 end-flow CTA probe. The wire diameter is 3.8 μm. Adapted from TSI Thermal Anemometry Probes catalog.

3.4.2 Setup

A TSI IFA-300 CTA system is used. It has a frequency response of 260 kHz, though the steady flows measured here do not necessitate fast sampling. This system is used with model 1241-T1.5 end-flow probes, which have a temperature limit of 150 C. These probes, shown in Fig. 3.4, allow for two-dimensional measurement of velocity, ideal for axis-symmetric flows. Due to the orthogonal sensor wires and support geometry, the probe volume is approximately 3.4 mm^3. A TSI model 1129 Air Velocity Calibrator is used to calibrate the system over the range of velocities to be measured.

The probes are mounted axially, above the coflow burner. The probe tip is placed approximately 1 mm above the nozzle tip in order to measure as close as possible to the flow boundaries without damaging the probe. The burner is mounted on rotational and horizontal translation stages. Radial sweeps of measurements are made in 100 μm increments, and are repeated at 6 azimuthal angles. A thermocouple is mounted parallel to the probes to monitor the gas temperature. The gas used for calibration and measurement is air.

3.5 Tomographic Inversion

Optical based measurements frequently measure line-of-sight integrated quantities. For example, the extinction coefficients measured in LES and DLE (Sections 3.1 and 3.2). However, knowledge of local quantities is usually desired. A tomographic inversion is used to determine local quantities from a set of projected quantities. In the case of axis-symmetric fields, local values can be extracted from the field of line-of-sight measurements using an Abel inversion.

An example of an axis-symmetric field is shown in Fig. 3.5. $z = f(r)$ gives the value of this field at radius r. The observed value, at $x = \infty$ a distance y from the center, is $Z = F(y)$. It represents the integrated values of $f(r)$ along the path parallel to x, at a distance $r \geq y$, as shown in equation 3.22, known as the Abel transform.

$$F(y) = 2 \int_y^\infty \frac{f(r)r}{\sqrt{r^2 - y^2}} dr \tag{3.22}$$

If $F(y)$ is known, the local values of $f(r)$ can be determined from equation 3.23, the inverse Abel transform.

$$f(r) = -\frac{1}{\pi} \int_r^\infty \frac{dF}{dy} \frac{dy}{\sqrt{y^2 - r^2}} \tag{3.23}$$

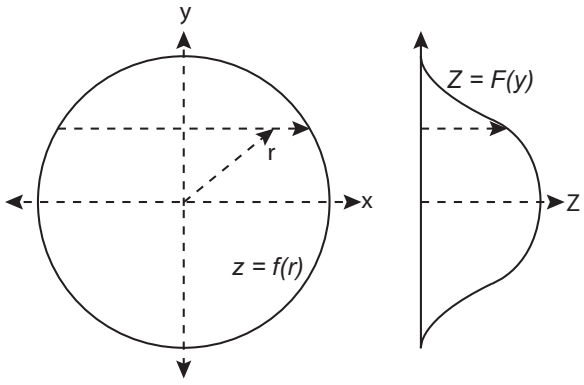

Figure 3.5: An axis-symmetric field, $z = f(r)$, and its projection, $Z = F(y)$, as viewed from an observer at $x = \infty$.

Numerous numerical techniques have been developed to solve the Abel transform and its inverse, summarized by Dasch in [73]. These methods typically recast equations 3.22 and 3.23 as in equations 3.24 and 3.25, respectively

$$\mathbf{b}(y_i) = \sum_{j=0}^{\infty} \mathbf{A}_{ij}\mathbf{x}(r_j) \tag{3.24}$$

$$\mathbf{x}(r_i) = \sum_{j=0}^{\infty} \mathbf{D}_{ij}\mathbf{b}(y_j) \tag{3.25}$$

where $\mathbf{x}$ and $\mathbf{b}$ are discrete sets of radial and projected data, f and F, and $\mathbf{A}_{ij}$ and $\mathbf{D}_{ij}$ are linear operators which differ with each method [73].

In practical applications, the derivative of $F(y)$ is not well known, owing to inevitable errors in measurement of $\mathbf{b}(y)$. As such, the Abel inversion is an ill-posed problem. In an experimental setting, the degree of ill-posedness will increase with finer measurement spacing. The problem can be regularlized, where the solution is found for a well posed problem that approximates the ill-posed problem. Tikonov regularized onion peeling has been shown to be an attractive method [74–76]. For onion-peeling, the linear operator is given by

$$\mathbf{A}_{ij} = \begin{cases} 0 & j < i \\ 2\triangle r[(j+1/2)]^2 - i^2]^{1/2} & j = i \\ 2\triangle r[(j+1/2)]^2 - i^2]^{1/2} - [(j-1/2)^2 - i^2]^{1/2} & j > i \end{cases} \tag{3.26}$$

Rather than solving the equation $\mathbf{Ax} = \mathbf{b}$, the augmented equation

$$\begin{bmatrix} \mathbf{A} \\ \lambda_r \mathbf{L} \end{bmatrix} \mathbf{x} = \begin{bmatrix} \mathbf{b} \\ 0 \end{bmatrix} \tag{3.27}$$

is solved [76], where λ_r is the regularization parameter and $\mathbf{L}$ is a smoothing matrix,

defined as in equation 3.28 for diffusion driven processes.

$$\mathbf{L} = \begin{bmatrix} 1 & -1 & 0 & \dots & 0 \\ 0 & 1 & -1 & & 0 \\ \vdots & & \ddots & \ddots & 0 \\ 0 & \dots & 0 & 1 & -1 \end{bmatrix} \tag{3.28}$$

The regularization parameter, λ_r, should be large enough to stabilize the inversion process, but not so large as to reduce accuracy. Selecting λ_r can be done using the L-Curve Criterion (LCC) [75, 76]. The L-Curve is produced by plotting the norms $||\mathbf{L}\mathbf{x}_\lambda||$ vs. $||\mathbf{A}\mathbf{x}_\lambda - \mathbf{b}||$ on a log-log scale for different values of λ_r, as shown in Fig. 3.6a. The curve consists of a noise dominate vertical portion, and an over-regularized horizontal portion. An ideal λ_r is the transition between these two, and can be found at the point of maximum curvature, shown in the red circle in Fig. 3.6a. Figure 3.6b shows curvature of the L-curve vs. λ_r, and the λ_r corresponding to maximum curvature is shown with the dotted line. Figure 3.6c shows an example of peak normalized projected extinction coefficient, as well as the local extinction coefficient after applying Tikonov regularized onion peeling using optimal λ_r.

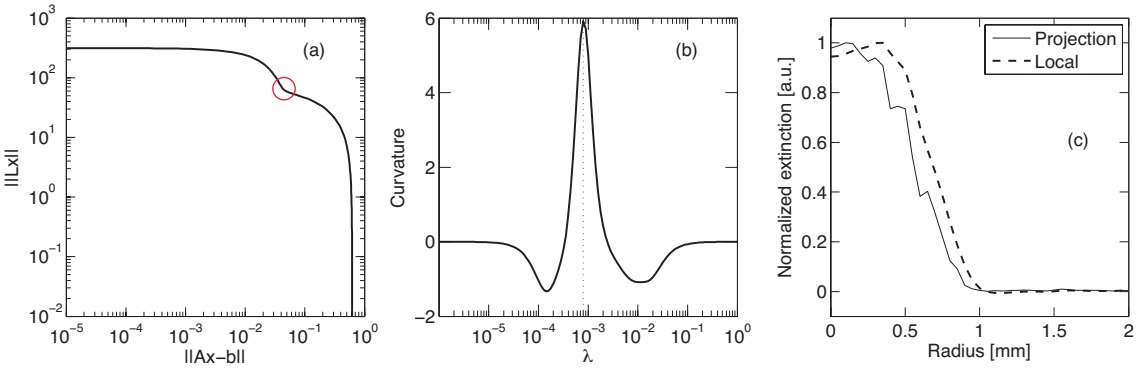

Figure 3.6: (a) The L-curve, (b) curvature of the L-curve, (c) projected and local values for regularization corresponding to max curvature.

Chapter 4

Coflow Characterization

4.1 Introduction

If the governing equations of a coflow flame are non-dimensionalized, several key quantities are revealed. One important non-dimensional quantity is the Reynolds number. The Reynolds number represents the relative importance of the momentum of a flow compared to its viscosity, and can be expressed as

$$\mathrm{Re} = \frac{\rho U d}{\mu} = \frac{U d}{\nu} \tag{4.1}$$

where U is the freestream velocity, d is the nozzle diameter, ρ is gas density, and μ and ν are the dynamic and kinematic viscosity, respectively. Roper has shown theoretically and experimentally [77, 78] that for a circular port burner, the ratio of flame height, H, to standard volumetric flowrate, Q, is well approximated by

$$\frac{H}{Q} = \left[4\pi\alpha_0 \ln\left(1+\frac{1}{S}\right)\right]^{-1}\left(\frac{T_0}{T_f}\right)^{0.67} \tag{4.2}$$

where S is inverse of stoichiometric mixture fraction, T_0 and T_f are equal to the inlet and flame temperatures, and α_0 is the thermal diffusivity at inlet conditions [77, 78]. α_0 is defined as $\alpha = k_g/\rho c_p$, where k_g is the thermal conductivity, and c_p is the specific heat. Using the definition of Re (equation 4.1) and defining the Prandtl

number $\mathrm{Pr} = \nu/\alpha$, equation 4.2 can be rewritten as

$$\frac{H}{d} = \mathrm{PrRe}\left[16\ln\left(1+\frac{1}{S}\right)\right]^{-1}\left(\frac{T_0}{T_f}\right)^{0.67} \tag{4.3}$$

Pr is independent of pressure, as both ν_0 and α_0 have inverse pressure dependence. To first approximation, for a given nozzle and fuel composition, d, S, T_0, and T_f are constant. Therefore, flame height is a funciton only of Re. For a circular nozzle, mass flowrate can be expressed $\dot{m} = \rho U \pi d^2/4$, and from Equation 4.1

$$\mathrm{Re} = \frac{4\dot{m}}{\pi\mu d} \tag{4.4}$$

and H is a function only of $\dot{m}$. This phenomena is frequently exploited when studying coflow flames at elevated pressures. As both flame cross-sectional area and nozzle exit velocity have inverse pressure dependence, the residence time at each height in the flame will be constant with pressure [36]. In principle, this allows meaningful comparisons at fixed heights above burner for flames at different pressures. A constant mass flowrate also implies constant carbon flowrate and flame power. In practice, H is not entirely independent of pressure [45], and Roper's analysis provides only an approximation to H.

4.1.1 Stability

As mentioned previously, one disadvantage of using coflow flames for study at elevated pressures is their tendency towards instability (Section 1.3)[48]. This instability is a result of buoyancy. The effect of gravity on the flame can be parameterized with the Grashof number, Gr [48]. The Grashof number indicates the relative importance of buoyancy compared to viscosity, and can be expressed as

$$\mathrm{Gr} = \left(\frac{\triangle T}{\overline{T}}\right)\frac{gH^3}{\nu^2} \tag{4.5}$$

where g is the gravitational constant, and $\triangle T = T_f - T_0$, $\overline{T} = (T_f + T_0)/2$. It is also sometimes convenient to use the Richardson number

$$\mathrm{Ri} = \frac{\mathrm{Gr}}{\mathrm{Re}^2} = \left(\frac{\triangle T}{\overline{T}}\right)\frac{gH^3}{U^2 d^2} \tag{4.6}$$

which represents the ratio of buoyant to inertial forces. Alternatively, the Froude number can be used

$$\mathrm{Fr} = \frac{U^2}{aH} \tag{4.7}$$

which indicates the ratio of inertial to buoyant forces. a is an acceleration constant, which for these flames is assumed to be $a = 41$ m/s^2 [78, 79]. This acceleration constant is based on the observed increase in axial velocity with Height Above Burner (HAB) in similar flames.

For a fixed Re and geometry, as pressure is increased, H is constant (Eq. 4.3). However, since both U and ν have inverse pressure dependance, Gr and Ri increase $\sim P^2$ (Eq. 4.5 and 4.6). As Gr and Ri are both $\sim g$, pressure can be used to simulate low or high gravity environements [80, 81]. From Eq. 4.1, 4.5, and 4.3, it is evident that shorter flames, produced with either low flowrates or on small burners, will have lower Gr, and hence be less influenced by bouyancy. This makes these flames more attractive for high pressure studies, as they can be scaled to higher pressures before suffering bouyant instabilities. For this reason, high pressure studies are often conducted with comparatively small flames [38, 39, 45, 55]. While limiting the relative importance of buoyancy is known to result in more stable flames, it has not been quantified in a general way.

The type of instabilites relevant here are Kelvin-Helmholtz instabilites, which arise due to a difference in velocities at the interface of two fluids [49, 82]. One method of suppressing coflow flame instabilities is to increase coflow rate [49]. This can be explained by Fig. 4.1, which shows a coflow nozzle and the velocities of

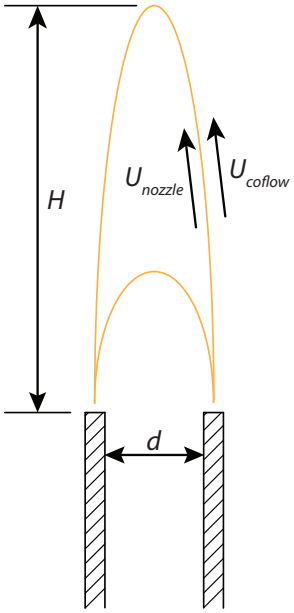

Figure 4.1: Coflow nozzle with some instability-relevant parameters indicated.

gases inside and outside the flame. Instabilities arise due to a difference in these velocities, and velocities inside the flame are accelerating due to buoyancy. Therefore, increasing velocity outside the flame should suppress the instability. This suggests the ratio of coflow to nozzle velocities, r_u, could also be an important dimensionless quantity governing these flames. Similar observations have been made in non-reacting flows [83]. To facilitate future coflow experiments at elevated pressures, the limits of stability in Gr/Re/r_u space should be explored. If the flame and its stability is well parameterized by these groups, these limits should hold for various fuels, geometries, and pressures.

4.1.2 Scaling

The increased buoyancy also affects the shape of the flame. Simulations, with and without gravity, demonstrate that the narrowing of the flame is due to gravity [84, 85]. So, in addition buoyant instabilities, the mixing field of the flame will change significantly with pressure. This change in mixing field could in part be responsible for observed changes in soot formation. Abdelgadir et al. [86] performed numerical

simulations of the ISF flames (Chapter 5). They found that increasing pressure while maintaining a constant mass flow rate (and hence Re) results in a decrease in scalar dissipation rate, χ. Scalar dissipation rate represents a local mixing time, and can be written as

$$\chi = 2\alpha|\nabla Z|^2 \tag{4.8}$$

where α is the thermal diffusivity, and Z is the mixture fraction. χ has been shown to be strongly correlated with the formation of Polycyclic Aromatic Hydrocarbons (PAH) [87–89]. The work of Abdelgadir et al. [86] concludes that the reduction in χ from increases in pressure promotes PAH formation and hence soot formation. When α and ∇Z are non-dimensionalized (the latter by U/d, another representation of mixing time), it is shown that the change in ∇Z is responsible for the change in dimensionless mixing field. This is a consequence of scaling flames with pressure at constant mass flowrate and geometry. If Re and Gr are the most important dimensionless quantities in characterizing these flames, and alternative method of scaling these flames in pressure would be at constant Re and Gr. Flames of similar Gr and Re would have χ fields scaled in a controlled way, by U and d. Therefore, the scaling of flames in Gr/Re space should be investigated. For the same reactants, maintaining constant Gr as pressure increases implies a reduction in H (Equation 4.5), and hence d (Equation 4.3).

4.1.3 Soot Suppression

Previous research has shown that, in addition to stabilizing flames, increased coflow velocity ratios suppress soot formation. Lin and Faeth and Dai and Faeth investigated the smoke point length for a number of different fuels, d, and Re at sub-atmospheric pressures [50, 51]. They found that increased coflow velocities increase the smoke point height, or even eliminate soot entirely, in non-bouyant flames. The mechanism for this was concluded to be a decrease in the residence time for soot production. In

non-buoyant flames or where $U_{coflow} > U_{nozzle}$, the direction of the normal component of the velocity across the flame sheet is from the fuel-rich side to the fuel-lean side, and the flame is said to be the "soot-formation-oxidation" configuration. In this configuration, increased U_{coflow} decreases residence time for soot formation proportional to H/U_{coflow}. In buoyancy dominated flames or where $U_{coflow} < U_{nozzle}$, flames are said to be in the "soot formation" configuration, with velocities from fuel-lean to fuel-rich. In this configuration, increased U_{coflow} cause the flame to transition to the "soot-formation-oxidation" configuration, resulting in earlier soot oxidation. However, these investigations were limited to 0.5 bar.

At the pressures investigated in this work, buoyancy will cause velocities above the nozzle to increase more than those outside of the flame. As a result, the "soot formation" configuration is expected, even with $r_u > 1$. Parallel to the studies of flame stability and scaling in Gr/Re/r_u space, soot suppression should also be investigated. While the focus of previous studies was on smoke points [50, 51], the focus of present studies is on quantifying the effect of r_u on f_v.

4.2 Methodology

A set of flames is investigated covering a range of Gr, Re and r_u space. In order to accomplish this, mass flowrates of fuel, diluent, and coflow are varied, as are d and P. The limits of stability within this space is first investigated. Next, the feasibility of rescaling the mixing field of flames at fixed points in this space is demonstrated. Finally, the effect of r_u on f_v is investigated for fixed configurations and Gr/Re pairs.

A summary of experimental conditions for this study is given in Table 4.1. Flames are established on burners B3, B4, and B6 (Section 2.1.2). These nozzle diameters are chosen to allow a range of Re and Gr to be investigated, and produce flames sized appropriately for DLE measurements (Section 3.2). Mass flowrates of methane, nitrogen, and air are limited by the specifications of the MFCs. Nozzle flows are either

pure methane or methane diluted 50% by mass with nitrogen. Methane fuels are used to facilitate parallel numerical studies, as the chemistry model is then consistent for each case, while allowing different fuels to be investigated. Nozzle Re from 15 to 105, in increments of 10, are investigated within the MFC limitations. This range of Re covers the range typically investigated in these types of high-pressure coflow flames. Coflow rates are set to r_u of 1, 3, 5, and 10. As the flame height cannot be known *a priori*, and for experimental simplicity, flames are investigated at fixed pressures, rather than fixed Gr. All flames are investigated at pressures of 1, 2, 4, 8, and 16 bar.

Table 4.1: Experimental conditions for stability and soot suppression study.

Fuel	d	Re										r_u
	[mm]	15	25	35	45	55	65	75	85	95	105	
Methane	3	×	×	×	×	×	×	×	×			1, 3, 5
	4	×	×	×	×	×	×					1, 3, 5
	6	×	×	×	×							1, 3, 5, 10
50% methane/ 50% nitrogen by mass	3	×	×	×	×	×	×	×	×	×		1, 3, 5
	4	×	×	×	×	×	×	×	×	×	×	1, 3, 5
	6	×	×	×	×	×	×					1, 3, 5, 10
P	1, 2, 4, 8, and 16 bar for all cases above											

In addition to these conditions, another set of flames is investigated specifically to examine the scaling of flames at constant Re and Gr. These conditions are shown in Table 4.2. As Gr is not known *a priori*, Gr is approximated by using Roper's approximation (Eq. 4.3) to estimate H. The difference between actual Gr and Gr_{Roper} is not important as long as the difference is similar for each nozzle.

Table 4.2: Experimental conditions for scaling study.

Designation	Re	Gr_{Roper}	P [bar]			r_u
			3 mm	4 mm	6mm	
A	15	1E6	12.1	8.1	4.4	5
B	25	2.2E5	2.7	1.7	1.0	5

Soot volume fraction is measured by DLE (Section 3.2). f_v is measured for flames

which are stable, sufficiently sooting, with $H < 26$ mm, as this is the detector height. Each measurement consists of 50 images with and without the flame present, and with and without the light source present. Flame shape is characterized by imaging with a Nikon D700 CMOS camera. The camera is fitted with a 105 mm lens, and mounted as close as possible to an optical port in the vessel.

4.3 Results

4.3.1 Stability

Observed flame behaviors are categorized as follows:

- stable flames display no discernible motion
- transition flames display some motion in the upper 2 mm of the flame
- flickering flames display Kelvin-Helmholz instabilities beyond the upper 2 mm
- lifted flames display significant asymmetrical lift from the nozzle, or cannot be stabilized due to blowoff
- wavy flames display a seemingly sporadic side-to-side motion not related to Kelvin-Helmholtz instabilities

An example of each of these behaviors is shown in Fig. 4.2. All flames pictured are of pure methane. The example stable, transition, and flickering flames are all established on nozzles of $d = 6$ mm, with Re = 35, and $r_u = 5$. Nominally, these flames should each have the same H (Equation 4.3). However, as the pressure is increased from 2, to 4, to 8 bar, the flame goes from stable, to transition, to flickering due to increased Gr. The "tip cutting" characteristic of Kelvin-Helmholtz instabilities is evident in the center image. While wavy flames often appear stable, they will eventually display a sideways motion, likely caused by re-circulation currents within the vessel.

Figure 4.2: From (l) to (r): stable, transition, flickering, lifted, and wavy flames.

The stability limits of all flames investigated in Gr/Re space is shown in Fig. 4.3. Stability maps are shown for r_u of 1, 3, and 5. Closed symbols represent flames of pure methane, while open symbols represent diluted flames. Symbol shapes represent different values of d, while colors indicate flame behavior.

The vertical axis (Gr) is log-scale, as Gr changes by many orders of magnitude over the currently investigated pressure range. The horizontal axis (Re) is linear-scale, as the range of Re is small, though still representative of the range of Re over which high pressure coflow flames have been investigated in the literature [36]. At a fixed pressure and d, an increase in Gr accompanies an increase in Re (Eq. 4.1, 4.5). Therefore, the lower limit on Gr which can be investigated at each Re in this work increases with Re, which explains the lack of measurements at high Re and low Gr. The lowest values of Gr represent 1 bar flames, while the highest Gr represent 16 bar flames.

First, a general observation can be made by looking at Fig. 4.3a-c: The behavior of a flame is fairly well characterized by the region of Gr/Re/r_u space it occupies, regardless of fuel and nozzle size (and consequently flame size). This demonstrates

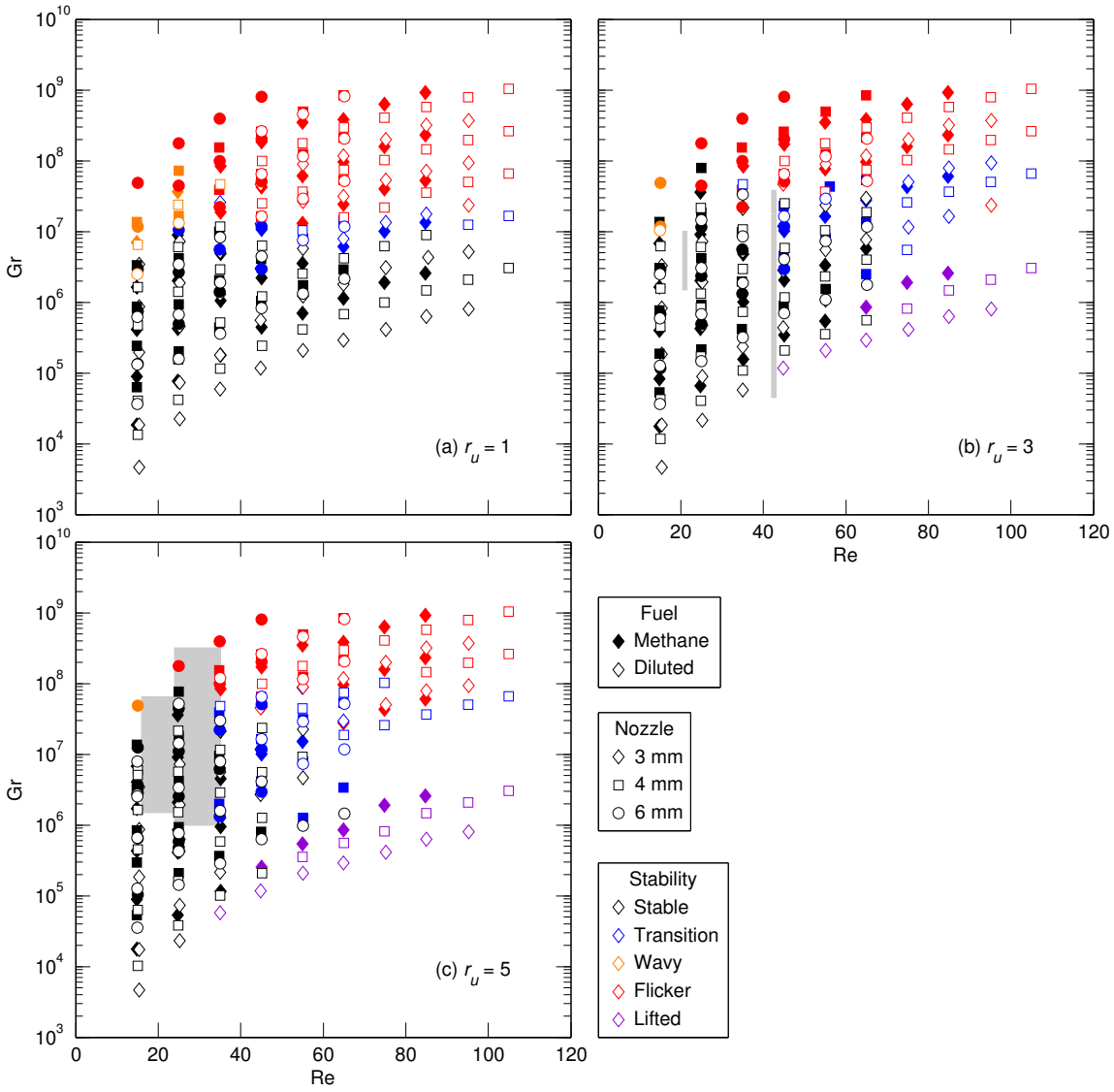

Figure 4.3: Behavior of coflow flames in Gr vs. Re space for $r_u = 1$, 3 and 5.

that, to first order, Gr, Re, and r_u can be used to characterize stability. Therefore, the information from Fig. 4.3 is simplified in Fig. 4.4 with each region separated by lines. Stable regions are those which contained only stable flames. Flicker regions show the furthest extent of where flickering flames are observed. Transition regions show the space between stable and flickering regions, and may contain some stable flames.

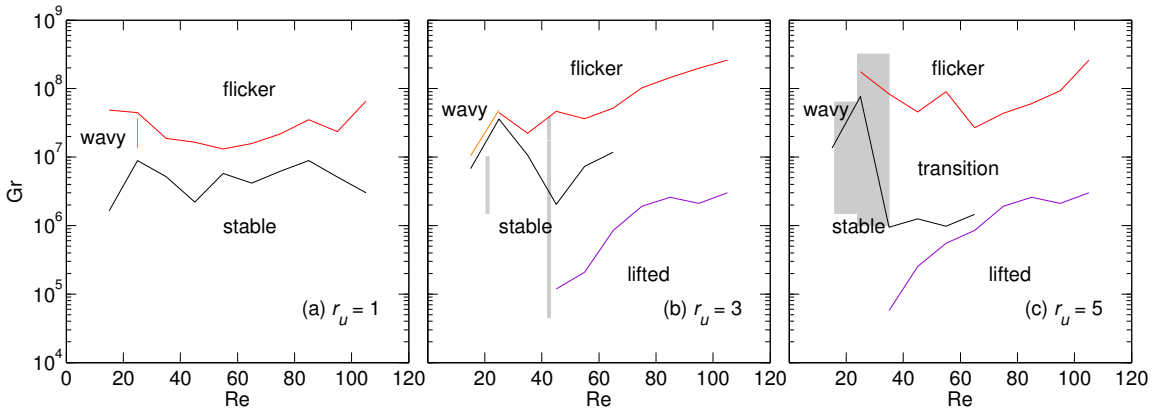

Figure 4.4: Behavior regions of coflow flames in Gr vs. Re space for $r_u = 1$, 3 and 5.

Figures 4.3a and 4.4a shows flames with $r_u = 1$. For these conditions, Gr is a reasonable indicator for when a flame will transition from stable to flickering, which occurs for Gr $\sim 10^7$. For very low Re, since $r_u = 1$, Re_{coflow} is also very low. As a result, the flames are susceptible to re-circulation within the vessel, and display a wavy behavior.

When r_u is increased to 3 (Fig. 4.3b and 4.4b), the onset of instabilities can be suppressed somewhat to Gr $> 2 \times 10^7$, and even to Gr $> 10^8$ for Re of 15 and 25. However, for flames of the largest diameter, coflow velocities are still too low to shield the flames. At $r_u = 3$, flames at 1 bar and Re ≥ 45 are lifted for smaller nozzle sizes. As U is higher for a given Re and smaller d, U_{coflow} will be higher as well. This suggests a limiting U_{coflow} to prevent liftoff, similar to the observations of [51] for sub-atmospheric flames.

A further increase in r_u to 5 (Fig. 4.3c and 4.4c) stabilizes a few cases which otherwise are unstable, either due to buoyancy or currents within the vessel. Some flames could not be run at 2 bar due to backpressure in the vessel exhaust system. However, some cases which are stable with $r_u = 3$ now become unstable. This is due to the now turbulent coflow. The Re range where flames are lifted also increases. The optimal r_u then depends on which Re and P range is to be investigated.

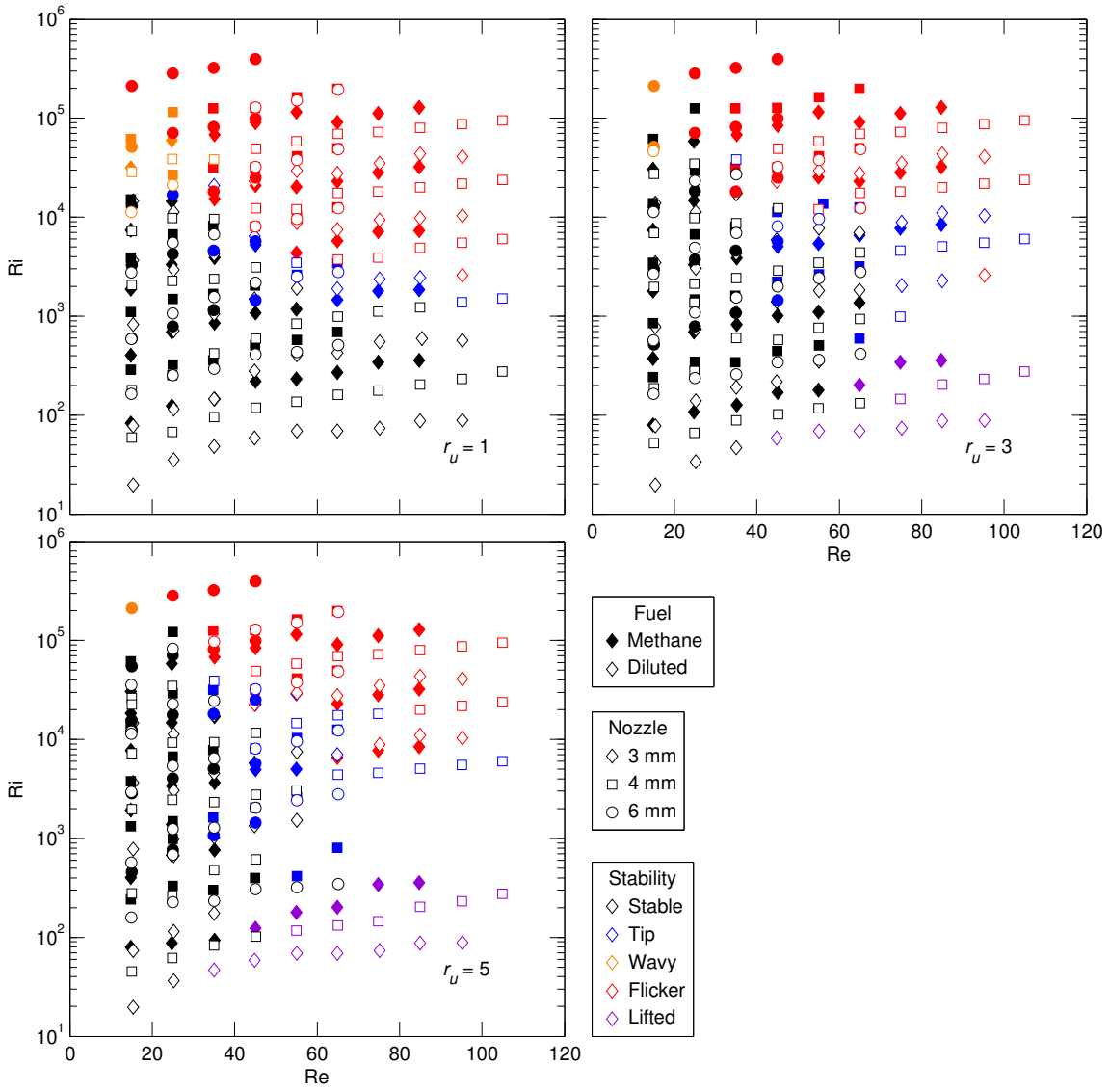

Figure 4.5: Stability of coflow flames in Ri vs. Re space for $r_u = 1$, 3 and 5.

Much of the work on high pressure laminar diffusion flames has been done by the group of Gülder. The shaded regions of Fig. 4.3 and 4.4 indicate the range covered by the experiments of Gülder et al. [30–35, 90]. Note that r_u varies from 3 to > 6 in the Gülder flames. The shaded regions in Fig. 4.3b represent ethylene and diluted-ethylene flames. The shaded regions in Fig. 4.3c correspond to methane, ethane, and propane flames. In general, the Gülder flames are established in regions of Gr/Re that are found to be stable in this work. The exception is the ethane flames

(Fig. 4.3c), which extend into the "unstable" region of the present work. It is not explicitly stated if stability prevented experiments at higher pressures. However, Joo and Gülder do discuss the problem of flame liftoff at pressures lower than measured [34], consistent with the observed liftoff region in 4.3b.

The inconsistency with the Gülder ethane flames could be due to differences in nozzle shape or flow boundary conditions (tophat velocity profile). All experiments here are conducted with nozzles of self-similar geometry. Present experiments are with only methane and diluted methane to facilitate numerical modeling. The main effects of fuel are on the location of the stoichiometric contour, which is accounted for in S, and the carbon massflowrate, which would affect sooting tendency. However, use of more sooty fuels, such as alkenes, may have a noticeable effect on flame shape due to significant radiation heat losses. While there is consistency between Gr and flame stability, it cannot be concluded if it can be applied universally.

The ISF flames (not shown) occupy the region from $\mathrm{Gr} = 1.4 \times 10^7$ to 2.2×10^8 at $\mathrm{Re} = 153$. r_u for the ISF flames varies from 1 to 3.5 (see Table 5.1). However, the flames are consistent with the present stability mapping, including the presence of small flickering at 8 and 16 bar.

Figure 4.5 shows the map of flame behavior in Ri/Re space, which is related to Gr/Re space as indicated in Eq. 4.6. The same stability regimes can be seen in this figure. However, the limiting Ri for flickering flames has a Re dependence. This suggests that Gr is a better overall indicator of possible flame instability.

4.3.2 Scaling

Figure 4.6 shows A flames with $\mathrm{Re} = 15$, and $\mathrm{Gr}_{Roper} = 10^6$. When adjusted for actual H, Gr varies from 3.2 to 4.1×10^6 for nozzles from 3 to 6 mm. The top row shows each flame on the same scale. Consistent with previous discussion, flames at higher pressures must be smaller to maintain a similar Gr. In the bottom row of

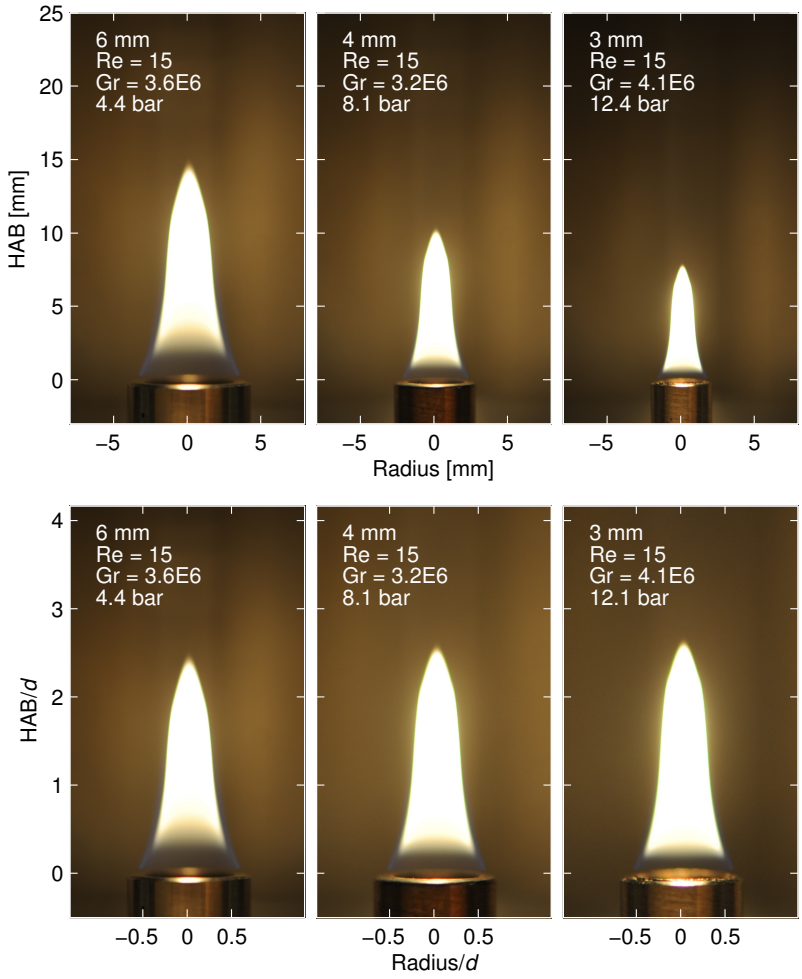

Figure 4.6: Flames at Re = 15 and Gr $\sim 3.6 \times 10^6$ (case A). The top row is dimensional, the bottom row is non-dimensionalized by d.

Fig. 4.6, each flame is non-dimensionalized by d in the axial and radial direction and plotted on the same dimensionless scale. It is evident that when re-scaled in this way, the flames have an almost identical shape. This confirms experimentally that Gr (or Ri) and Re can sufficiently describe coflow flame shape, for a given fuel. As the images are saturated, flame luminosity cannot be compared even qualitatively. However, the blue chemiluminescent flame region near the nozzle is less pronounced at lower pressures due to the strong soot luminosity. This is indicative of soot forming at lower HAB at higher pressures.

Measured f_v for flame A is shown in Fig. 4.7, both dimensional and dimensionless.

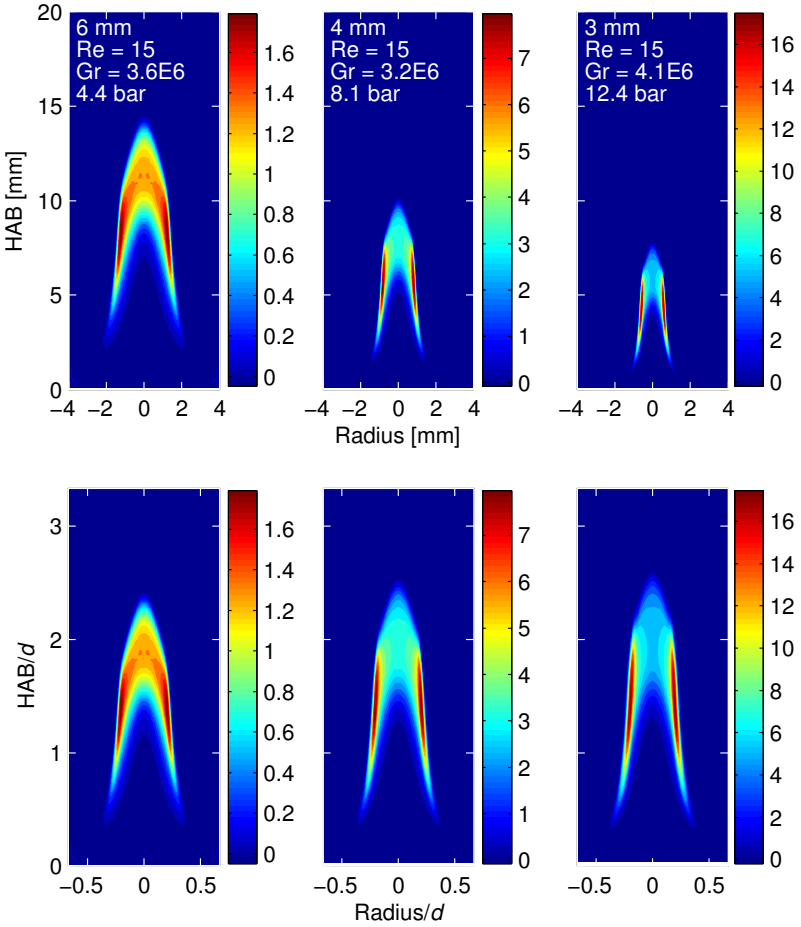

Figure 4.7: Soot fields [ppm] at Re = 15 and Gr $\sim 3.6 \times 10^6$ (case A). The top row is dimensional, the bottom row is non-dimensionalized by d.

As with flame shape, the distribution of soot within the flame is very similar for these flames at $\sim$ Gr and Re. The distribution of soot does become more annular at elevated pressures.

A similar comparison is made of B flames in Fig. 4.8. Here, the flames span a much lower pressure range. The rescaled flames shows reasonable similarity. At these pressures, H is much more sensitive to pressure [30]. The similarity of flames at constant Gr and Re assumes H is a function of Re only. This demonstrates that for low pressure ranges, the flame shapes are not completely defined by Gr and Re.

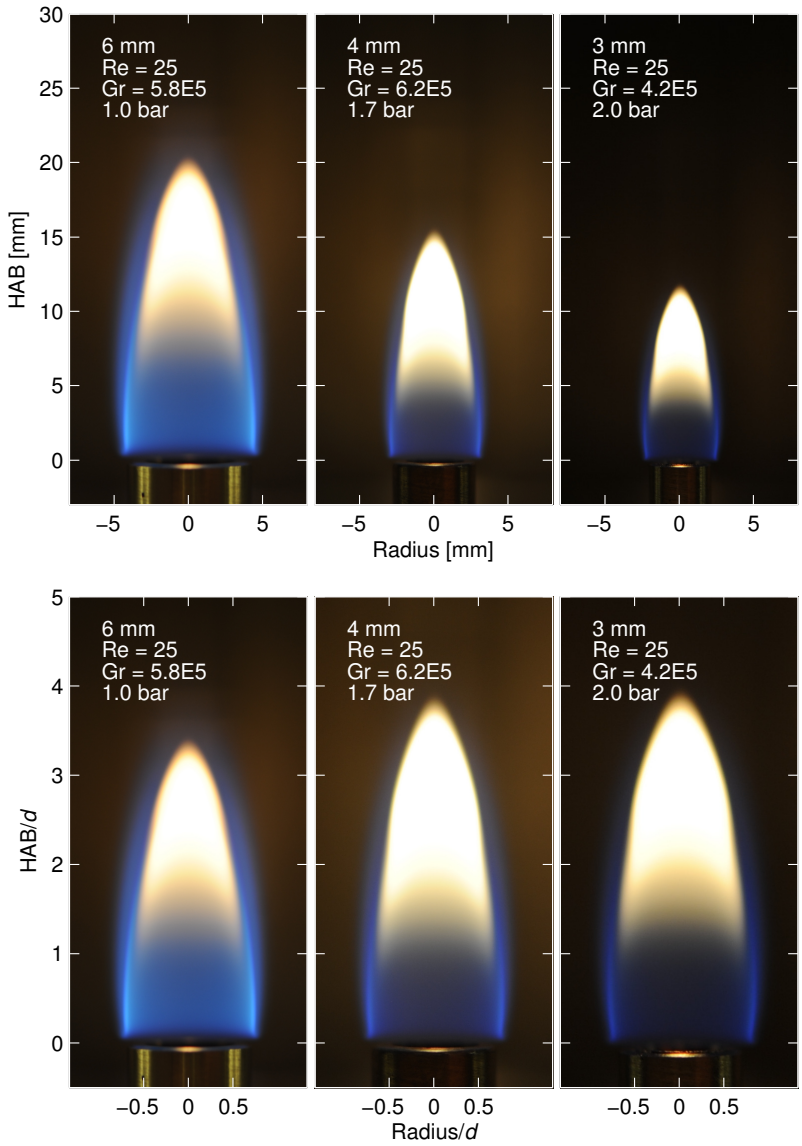

Figure 4.8: Flames at Re = 25 and Gr $\sim 6\times10^5$ (case B). The top row is dimensional, the bottom row is non-dimensionalized by d.

Integrated carbon conversion, or soot yield, is a frequently used metric for comparing the sootiness of coflow flames [30, 34, 36, 90, 91]. Soot yield (η_s) represents the fraction of fuel carbon as soot, and is found from $\eta_s = \dot{m}_s/\dot{m}_c$, where $\dot{m}_s$ and $\dot{m}_c$ are the soot and total carbon mass flowrates, respectively. $\dot{m}_s$ is defined as

$$\dot{m}_s = \rho_s \int 2\pi r v_z f_v \mathrm{d}r \tag{4.9}$$

where $\rho_s = 1.9$ g/cm^3 is the density of soot and v_z is the axial velocity. As no in-flame velocity information is available, axial velocities are estimated using the relation $v_z = \sqrt{2az}$, where $a = 41$ m/s^2 [79, 90].

Since η_s is normalized by fuel carbon flowrate, it is useful for comparing different coflow flames. Figure 4.9 shows axial profiles of η_s as a function of normalized HAB for A and B flames. Profiles are identified by the diameter of the nozzle used, as the pressure differs between diluted and undiluted cases. Diluted A and B flames could not be measured for all nozzle diameters. Similar to the observations of Fig. 4.7, the normalized profiles are remarkably similar. The first non-negligible η_s and peak η_s occur at the same number of nozzle diameters downstream for each nozzle/pressure. This is contrary to the observations of η_s in constant $\dot{m}$ flames (Fig. 5.5), where peak values occur earlier in the flame at elevated pressures. For a given Re and Gr, diluted flames are longer, hence the lower dimensionless HAB of peak η_s for the diluted flames.

The scaling of η_s with pressure is shown in Fig. 4.10. Scaling is shown for the A and B flames, diluted and undiluted. Additionally, black lines show the scaling of flames at constant $\dot{m}$, with $d = 3$ mm and Re = 15 and 25. The scaling of methane flames at constant $\dot{m}$ agrees well with the work of [30], whose flames are of $d = 3.06$ mm and Re ~ 21. If fitted to a power law, the present constant $\dot{m}$ flames scale with $P^{1.6}$, compared to a scaling of $P^{1.3}$ in [30]. The figure demonstrates that a constant Gr scaling yields a weaker pressure dependence than constant $\dot{m}$. This is expected, as [86] conclude that the suppression of scalar dissipation rate for constant $\dot{m}$ scaling promotes soot growth. A flames of pure methane scale as $P^{1.0}$ over the same pressure range. Diluted methane flames show a stronger pressure sensitivity, scaling with $P^{1.9}$. B flames of pure methane scale with $P^{2.4}$ over a much lower pressure range, where a stronger pressure dependence is expected.

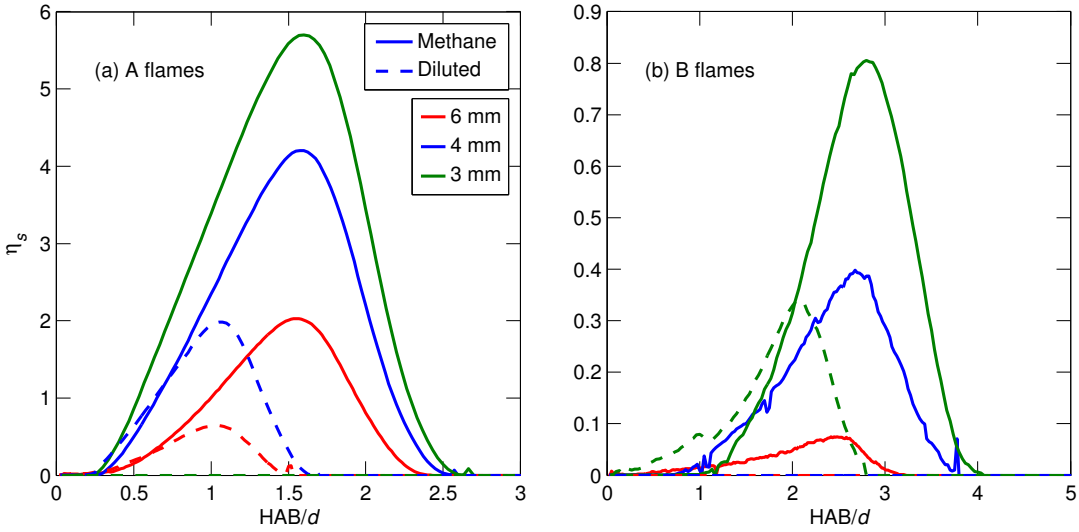

Figure 4.9: η_s as function of normalized HAB for A and B flames.

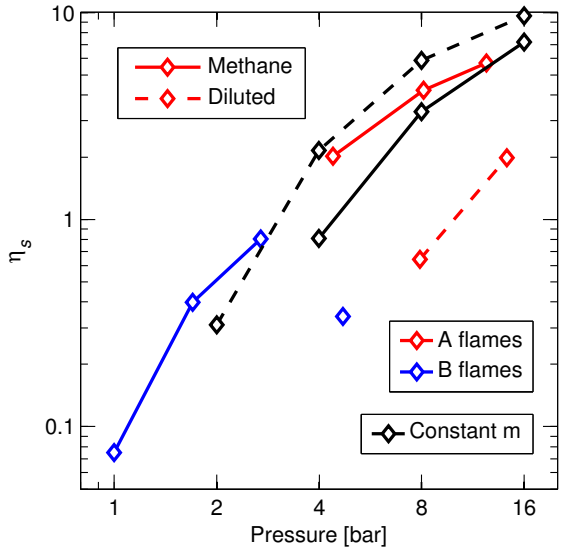

Figure 4.10: Scaling of η_s with pressure for A and B flames, diluted and undiluted.

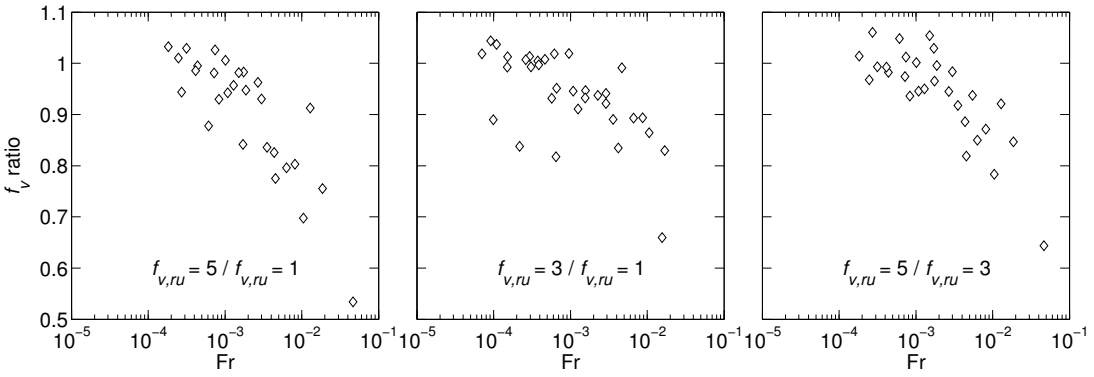

Figure 4.11: Soot suppression for r_u ratios of 5:1, 3:1, and 5:3 as a function of Fr.

4.3.3 Soot Suppression

Soot suppression for each of the flames measured at multiple r_u is shown in Fig. 4.11. As the work of [50, 51] suggests that soot suppression is strongest in non-buoyant flames, each panel shows the ratio of peak f_v for different r_u as a function of Fr. Similar trends can be observed as a function of Ri, though the correlation is weaker. Figure 4.11 shows a general correlation between the magnitude of suppression and Fr. For each f_v ratio, f_v in the less buoyant flames (high Fr) can be suppressed more with increased r_u. For the least buoyant flames, increased r_u actually increases peak f_v.

While the suppression of peak f_v has been shown, it is important to evaluate how the f_v field changes with r_u. Example soot fields at $r_u = 1$, 3 and 5 are shown in Fig. 4.12. In this flame, there is a significant change in soot concentrations with increased r_u, with soot concentrated at flame tip. However, in a more sooty flame, shown in Fig. 4.13, there is not a significant change in concentration. It is evident that peak f_v in these flames is located in the flame annulus.

Profiles of peak f_v, for the same flames in Fig. 4.13, along flame centerline and at each HAB, are shown as a function of HAB in Fig. 4.14. Figure 4.14a shows f_v, in ppm. It is evident that f_v along both the centerline and in the annulus decreases by the same relative amounts. This is consistent with the conclusions of [51], that

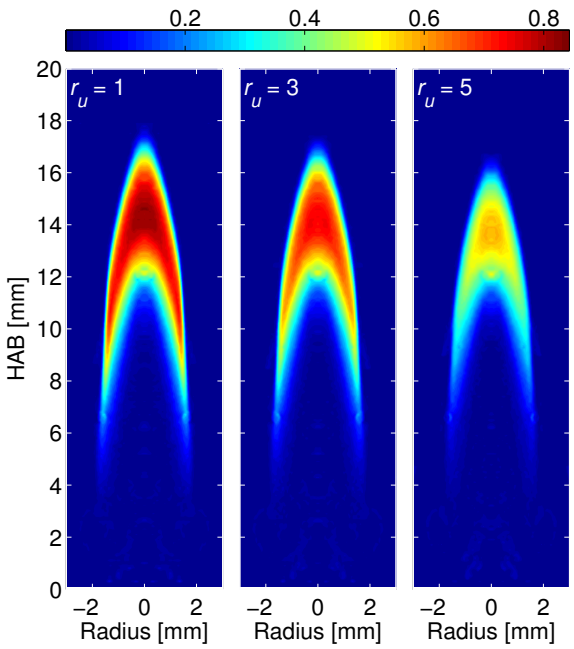

Figure 4.12: f_v [ppm] in diluted methane flames at Re = 55, Gr $\sim 5 \times 10^6$ (d = 3 mm, P = 4 bar), and r_u = 1, 3, and 5.

increasing r_u turns the flame streamlines from fuel-rich to the fuel-lean side of the flame. This increases oxidation rate along the annulus, and pulls precursor species from the core of the flame. In Fig. 4.14b, f_v is normalized by peak value for each case. Here, it can be seen that the HAB where soot starts to form does not change significantly. Oxidation does appear to start 0.4 mm earlier in the flame. This is also consistent with [51], which conclude that for buoyant flames, increased r_u results in earlier oxidation.

4.4 Conclusions

Images and soot volume fraction measurements are made in a number of flames spanning the three-dimensional space of Gr/Re/r_u. The limits of stability of coflow flames in this space is evaluated. The ability to scale flames in this space is investigated by changing pressure and nozzle diameter. The effect of r_u on soot is also investigated. The major outcomes of these investigations are the following:

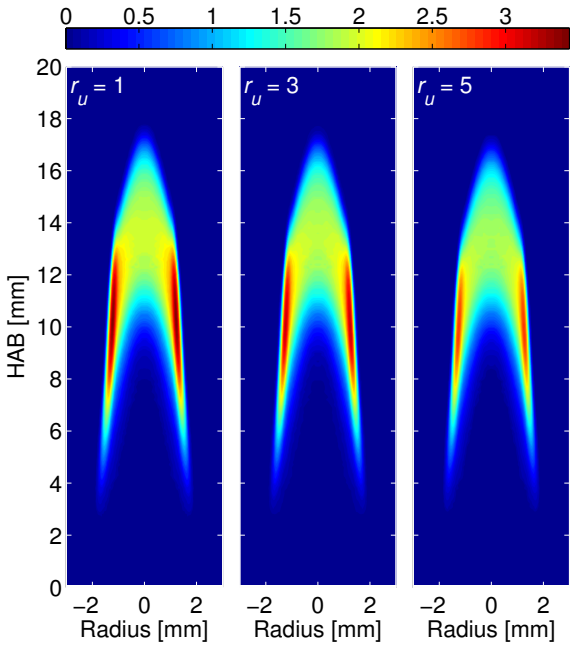

Figure 4.13: f_v [ppm] in methane flames at Re = 35, Gr $\sim 5 \times 10^6$ ($d = 3$ mm, $P = 4$ bar), and $r_u = 1$, 3, and 5.

Over the range of Re investigated, Gr is a reasonable predictor of flame stability. The limiting value of Gr for stable flames is dependent on r_u and Re, and may differ for burners of different design.

Flame shape, for a given fuel, can be sufficiently described by Gr (or Ri) and Re. Flames scaled in pressure by using nozzles of different diameters show self-similar shape, soot fields, and soot yield profiles.

An alternative method of scaling flames in pressure is proposed. Scaling flames at constant Re and Gr reduces the effect of hydrodynamic changes on soot yield by scaling scalar dissipation rate in a controlled way. Soot yield in flames scaled at constant Re and Gr have a weaker pressure dependence than flames scaled at constant $\dot{m}$ over the same pressure range.

The ratio of coflow to nozzle velocities plays an important role in stabilizing flames. Increased coflow rate can enhance flame stability and suppress soot. The suppression of soot is correlated to the relative importance of buoyancy of the flame, with less

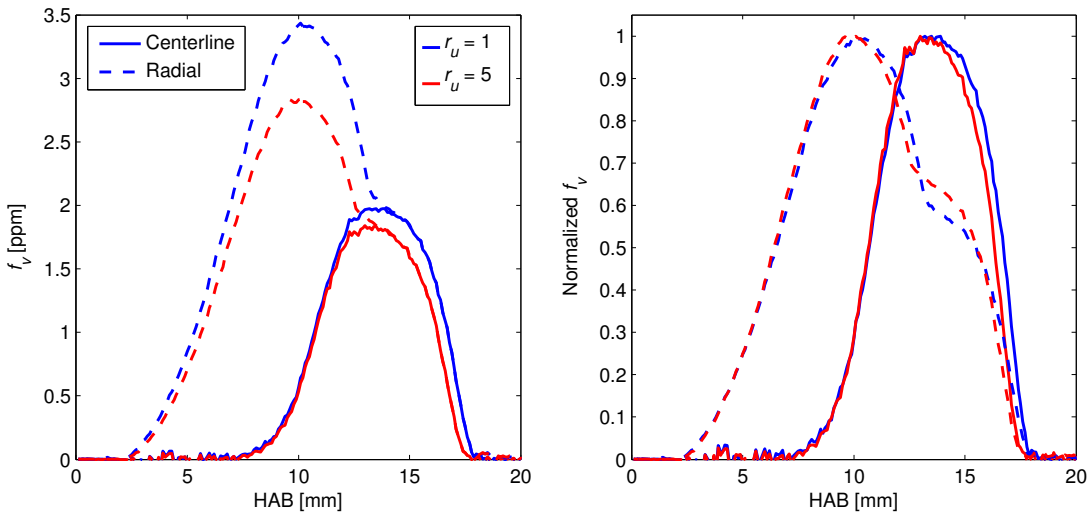

Figure 4.14: Peak centerline and radial f_v [ppm] and normalized f_v in methane flames at Re = 35, Gr $\sim 4.8 \times 10^6$ ($d = 3$ mm, $P = 4$ bar), and $r_u = 1$ and 5.

buoyant flames more susceptible to soot. The most suitable r_u depends on the P and Re of interest.

Chapter 5

Soot Particle Size in Diffusion Flames at Elevated Pressures

5.1 Introduction

As outlined in the Introduction (Sections 1.3 and 1.4), enhancement of the data set for the ISF's target pressurized laminar diffusion flame is one of the contributions of this work. This chapter discusses the addition of soot concentration and particle size. Predictive capability of soot mass produced is of fundamental importance for advanced combustion models. Particle size has more recently been identified as an important soot parameter, as airborne particulate size affects its toxicity [40]. The present measurements are done using LES. While LE generally performs poorly at elevated pressures [36], simultaneous scattering offers one of the few methods for measuring particle size. Until such time that a more advanced particle size measurement technique could be applied (such as TiRe-LII, Chapter 6), LES is able to provide useful information where there is otherwise a dearth of data.

5.2 Methodology

Flames are established on burner A. A summary of mass flowrates ($\dot{m}$), bulk velocities (U), and dimensionless quantities in the nozzle (noz) and coflow (cof) is given in Table 5.1. Ethylene and nitrogen mass flow rates from the nozzle are fixed at all pressures, producing a fuel stream diluted 82.5% by volume. Air coflow rates are adjusted at each pressure to compensate for pressure-scaled buoyancy. While increasing coflow rate may suppress soot formation [51], it is necessary to maintain flame stability

at elevated pressures. The implications of this are further discussed in Chapter 4, and the overall effects is expected to be a less than 20% reduction in f_v. The Re (Equation 4.1) of the nozzle flow is fixed at 153, and Re of the coflow is calculated using hydraulic diameter. The Froude number (Equation 4.7) of the nozzle flow is calculated using flame height, $H = 27$ mm, and assuming the acceleration due to buoyancy, $a = 32\ \mathrm{m/s^2}$ [78, 90]. The Fr numbers indicate that the flames are buoyancy dominated. Nozzle temperature is measured on the outside surface of the nozzle, 2 mm below exit, with a 130 μm diameter K-type thermocouple. One measurement is made at operating conditions, and a second is made 10 s after reducing the coflow rate significantly. There is <1 C difference between these two values. Coflow temperature is measured on the honeycomb surface with a similar thermocouple 25 mm from centerline.

Table 5.1: ISF flame flow parameters

P [atm]	$\dot{m}_{C_2H_4}$ [mg/s]	$\dot{m}_{N_2}$ [mg/s]	$\dot{m}_{air}$ [g/s]	U_{noz} [cm/s]	U_{cof} [cm/s]	r_u	Re_{noz}	Re_{cof}	Fr_{noz}	T_{noz} [C]	T_{cof} [C]
4	1.37	6.41	1.25	13.3	13.3	1.0	153	1980	0.143	62	21
8	1.37	6.41	2.51	6.6	13.3	2.0	153	3960	0.071	59	20
12	1.37	6.41	4.04	4.4	14.2	3.2	153	6350	0.048	56	20
16	1.37	6.41	4.42	3.3	11.7	3.5	153	7000	0.036	52	20

Mean velocity profiles for the atmospheric pressure cold flow, using Re for the 4 atm case, are shown in Fig. 5.1. Velocities over the nozzle and coflow are normalized by the respective bulk velocities. Measurements are made 1 mm above nozzle exit by CTA (Section 3.4). 1000 samples are taken at each point, in radial increments of 100 μm. Measurements at 6 azimuthal angles are averaged. RMS velocity profiles are almost identical, though a few percent higher outside of $r = 22$ mm. Integration of these velocities around the axis of symmetry results in calculated flow rates about 10% higher than actual. Based on this and probe calibration, the uncertainty in these velocities is estimated to be 10%. When examining these profiles, one should

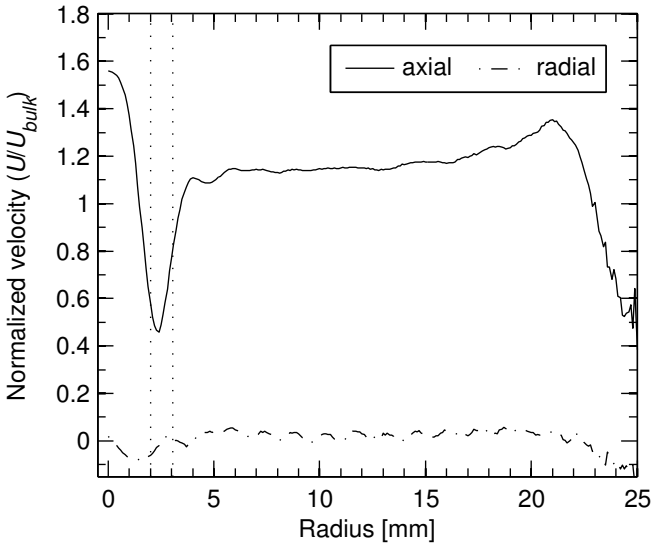

Figure 5.1: Axial and radial mean velocity profiles of the cold flow, measured 1 mm above the nozzle outlet, with Re of the nozzle = 153, and Re of the coflow = 1980. Velocities are normalized by the corresponding bulk velocity. The dotted lines indicate the inner and outer radii of the nozzle.

consider that measurements are made 1 mm downsteam of the nozzle and 6 mm downstream of the coflow, and that the probe volume (3.4 mm^3, see Fig. 3.4) is not small compared to the nozzle diameter. The nozzle flow is seen to be parabolic in shape, while the coflow profile can be approximated as top-hat. The coflow bulk velocity can be estimated using an effective coflow diameter of 47 mm.

Soot volume fraction and particle size are measured by LES (Section 3.1). As there has been very little investigation on soot morphology and optical properties at elevated pressures, values typical of atmospheric in-flame soot are used. Soot optical properties are assumed to be $\rho_{sa} = 0.26 \pm 0.05$, $E(m) = 0.37$, and $F(m) = 0.65 \pm 0.17$ based on dimensionless extinction coefficient measurements in ethylene coflow flames [64], with the uncertainties estimated based on the ranges of values measured in [64]. For measurements at 632.8 nm and $\theta = 90°$, $q^{-1} = 70$ nm. Optical access limitations of the pressure vessel restricted scattering measurements to only one angle, and large variation of q through wavelength is impractical, requiring values of k_f and D_f to be assumed. The values used here ($D_f = 1.7 \pm 0.15$, and $k_f = 2.4 \pm 0.4$) were determined

in similar flames at atmospheric conditions [62]. While assuming fractal properties may limit the applicability of this analysis, as it may be the properties themselves are changing with pressure, it does allow some quantification of changes with pressure. Measurements are taken in radial increments of 50 μm and axial increments of 1 mm. A total of 150 measurements are done at each point during 3 sets of experiments.

There are three types of systematic errors accounted for: beam steering, non-linearity of the PMT, and uncertainties of the assumed optical properties ($F(m)$, ρ_{sa}, D_f, and k_f). Beam steering uncertainty in transmissivity is evaluated as a linear fit from measured extinction just outside the visible flame [30] to 0 at flame center-line. Non-linearity of the PMT is evaluated with neutral density filters. There are four random errors accounted for: precision of photodiode measurements, precision of PMT measurements, calibration of Q_{vv} by Raleigh scattering, and averaging of extinction coefficients in each flame half. The propagation of transmissivity uncertainty through the tomographic inversion is evaluated as in [73]. Uncertainties of indirect measurements are calculated using the square-root sum formula [92], and represent a 95% confidence interval. In addition to the quantified uncertainties, there are other uncertainties that deserve consideration. As previously mentioned, soot optical properties are unlikely to be constant throughout the flame. In fact, LES may not even detect nascent soot at all [93], which may be concentrated in the lower portion of the flame. This would result in an under-prediction of f_v and an over-prediction of particle size. Any effect of pressure on optical properties is also unknown. However, using Eq. 3.4-3.7, reported f_v, D_{63}, and d_p can easily be corrected for different values of ρ_{sa}, $E(m)$, $F(m)$, D_f and k_f if deemed more appropriate. The applicability of Rayleigh and RDG-PFA theories to large particles should also be considered.

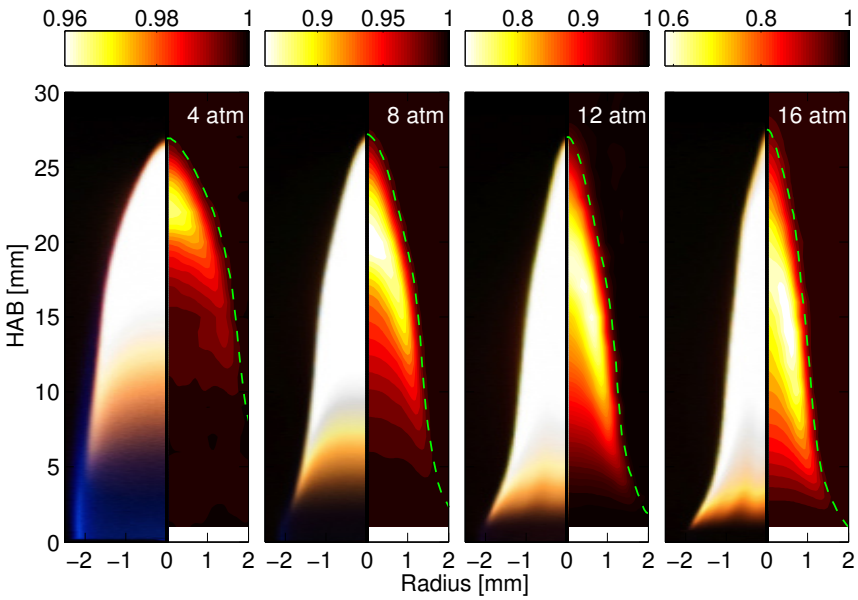

Figure 5.2: Qualitative flame images (left) taken with a Nikon camera, and transmissivity contours (right) for nitrogen-diluted ethylene flames from 4-16 atm. The green iso-contour indicates the edge of the luminous sooting region. The aspect ratio is adjusted for clarity.

5.3 Results

The flames are measured to be approximately 27 mm tall at all pressures, with a flicker in the top 1 mm of the flame at 12 and 16 atm. Figure 5.2 shows a comparison of flame images and transmissivity contours. A comparison of the images and measurements reveals two things. First, in the lower region of the flame, where luminosity is indicative of soot, the measurements indicate no extinction. This suggests very fine or nascent soot particles, undetectable by the extinction technique. Second, the effect of beam steering is noticeable from the measurement of extinction outside the visibly sooting region, highlighted by the green iso-contour. This effect becomes apparent as pressure is increased, and is one of the major limitations of LE and LOSA at elevated pressures [36].

5.3.1 Soot Concentration

Radial profiles of measured f_v are shown for several HAB in Fig. 5.3. Error bars are included for the measurements near centerline and peak values, where the errors are largest. Peak values of measured f_v are 1.5, 7.1, 16.8, and 33.3 ppm located 23, 22, 17, and 13 mm above the burner, at 4, 8, 12, and 16 atm, respectively. The peak values are located on the centerline at 4 and 8 atm, and in the annulus at 12 and 16 atm. If peak values are fit to a power law curve, measured peak values scale with pressure as $P^{2.2}$, though the location of peak value shifts with pressure. Peak values of f_v in only the annulus of the flame show a similar scaling of $P^{2.3}$, while peak values near centerline scale with $P^{2.0}$. The scaling of peak f_v on centerline and in the annulus can be seen in the inset of Fig. 5.3. It should be noted that necessary changes in coflow rate with pressure may affect this scaling, and could also be responsible for the shift in peak f_v location. Peak path-averaged f_v, with path lengths determined from the width of the luminous sooting region, are 1.1 and 5.6 ppm at 4 and 8 atm, respectively. In comparison, peak averaged f_v of these flames measured by two-color pyrometry were 1.8 and 7 ppm at 4 and 8 atm respectively [55]. The discrepancy at 8 atm could be a result of the increased velocity ratio in this work. Narrowing of the flame, constant flame height, formation of soot lower in the flame, and increase in soot concentrations as pressure increases are consistent with previous studies of these types of flames [26, 30, 34, 36, 38, 39, 41, 55].

The largest sources of error for f_v are beam steering and the averaging of flame halves. Typical uncertainties are demonstrated in Fig. 5.4, which shows a) f_v at 17 mm HAB in the 12 atm flame, and b) the contribution from each parameter to this uncertainty. It should be noted that these individual uncertainties are combined by the square-root sum formula to obtain the total uncertainty [92]. Uncertainty due to precision of transmissivity measurements is propagated through the tomographic inversion, resulting in larger errors on centerline. The discrepancy in f_v between

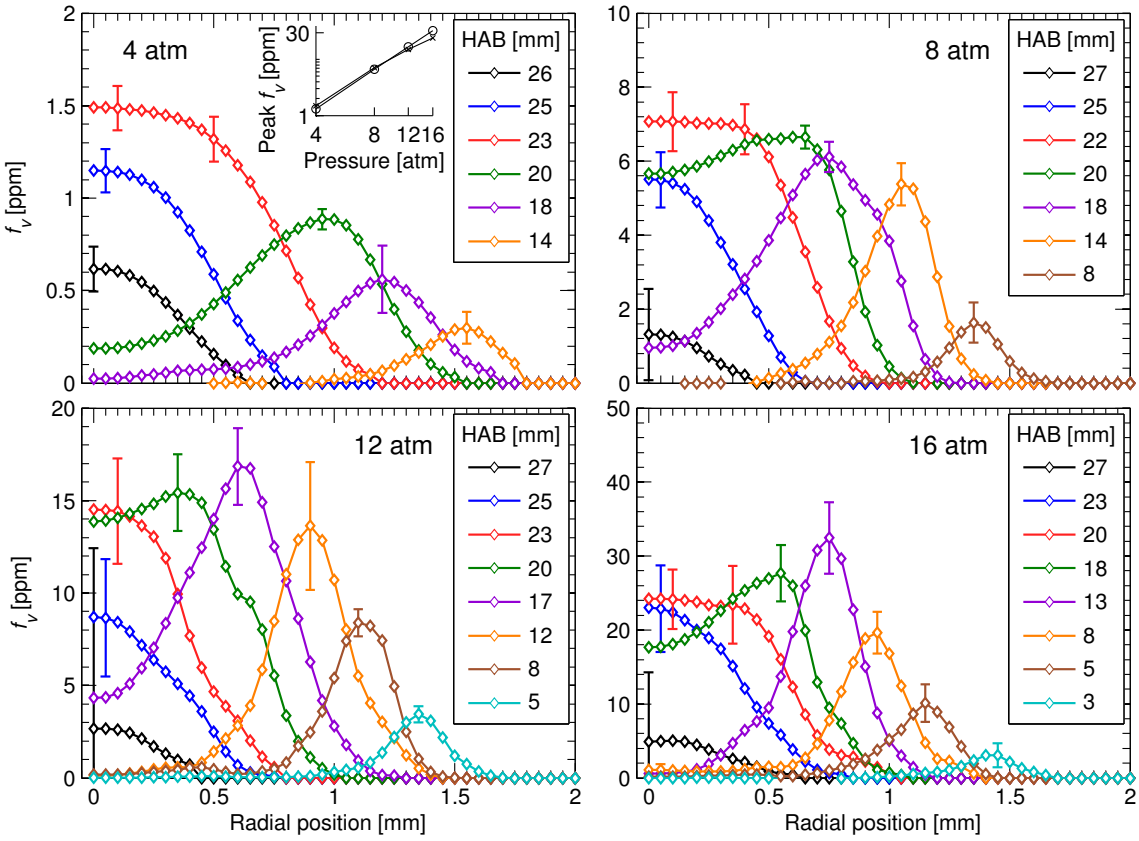

Figure 5.3: Local f_v at different HAB in nitrogen-diluted ethylene flames from 4-16 atm. Inset of 4 atm: Peak f_v on the centerline (x) and in the annulus (o) as a function of pressure on a log-log scale.

flame halves could be due to slight asymmetries magnified by tomographic inversion. Beam steering uncertainty is assumed to be largest at the edge of the flames, where gradients perpendicular to the laser beam are largest. At locations of peak f_v, the largest contributors to uncertainty are beam steering and measurement precision. Some locations have a local uncertainty of more than 100%, and a minimum of zero for the interval of uncertainty, particularly due to beam steering.

Figure 5.5 shows the integrated carbon conversion, or soot yield, as a function of HAB (Equation 4.9) [30, 34, 36, 90, 91]. As no in-flame velocity information is available, axial velocities are estimated using the relation $v_z = \sqrt{2az}$, where $a = 41$ m/s^2 [79, 90]. Due to a reduction in flame volume with pressure, η_s is a better indicator of sooting tendency than peak values of f_v. Fitting to a power law, peak

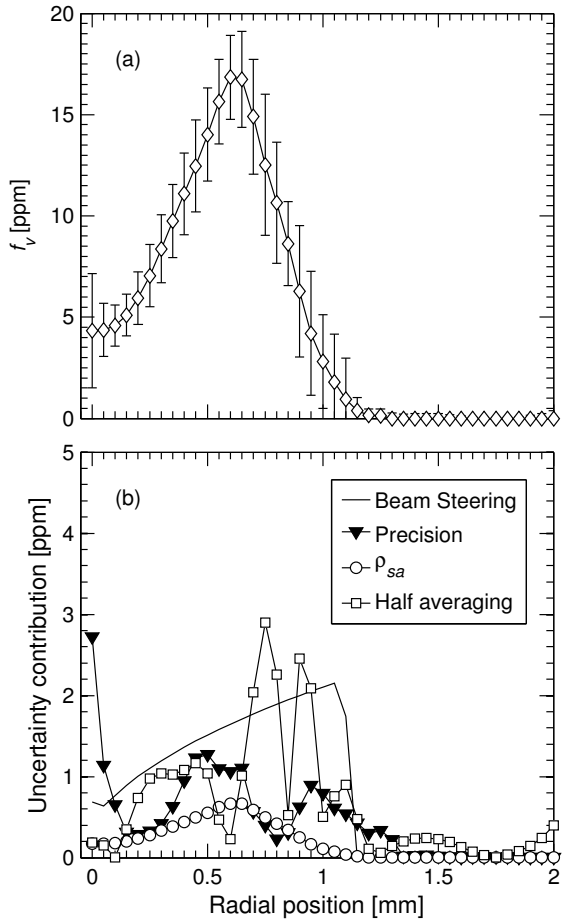

Figure 5.4: a) Local f_v 17 mm above burner in a nitrogen-diluted ethylene flame at 12 atm, b) Contributions to f_v uncertainty from beam steering, transmissivity measurement precision, ρ_{sa}, and averaging of left and right flame halves.

η_s scales as $P^{1.8}$, and this is demonstrated in the inset of Fig. 5.5. The flames most similar to these in the literature are those of [34]. While the flowrates in this work are about 5 times those of [34], the dilution ratio and velocity ratio at 16 atm are comparable. With these considerations, trends in soot concentrations and yield are consistent.

5.3.2 Particle Size

Assuming spherical soot particles, D_{63} can be directly calculated from the ratio of measured Q_{vv} and f_v. As it is aggregates, and not individual spherules, that are

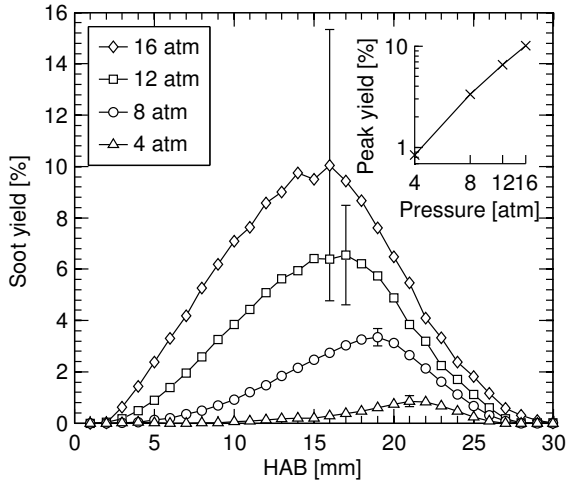

Figure 5.5: Soot yield as a function of HAB in nitrogen-diluted ethylene flames from 4-16 atm. Inset: Peak soot yield as a function of pressure on a log-log scale.

responsible for the observed scattering, D_{63} represents some intermediate average diameter between that of the primary particles and the aggregates. Radial profiles of D_{63} are shown in Fig. 5.6, with error bars. Errors are largest where f_v has the largest uncertainty (centerline), or where f_v is very small (edges of the annulus). Peak particle sizes, with respect to HAB, are nearly constant in areas of appreciable soot at 4 atm. Particle sizes increase with pressure, with the largest increase between 4 and 8 atm, and little increase in sizes between 12 and 16 atm. Like f_v, D_{63} is seen to increase faster with pressure in the annulus of the flame than near centerline, consistent with the observations of [41].

In general, D_{63} peaks are at the location of peak f_v at each flame height. However, at more elevated pressures, where gradients in f_v and Q_{vv} are higher, calculated D_{63} are larger near the edge of the flame. A possible reason for this is demonstrated in Fig. 5.7, which shows the radial profiles of normalized Q_{vv}, κ_a, and D_{63} at 4 mm HAB for the 16 atm case. The circled regions show areas of large gradients but low relative values. Due to the regularization of the tomographic inversion, the calculated edge of the sooting region may be shifted radially. As it is their ratio that is used to

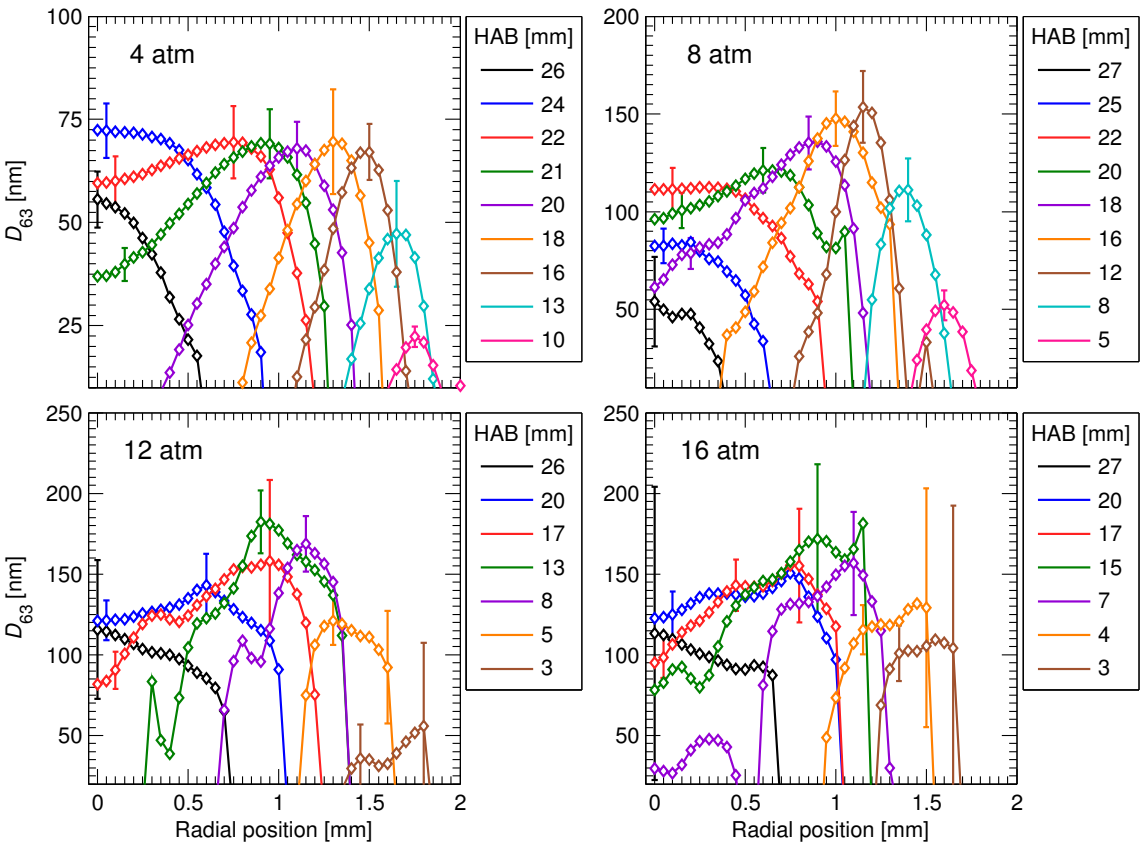

Figure 5.6: D_{63} at different HAB in nitrogen-diluted ethylene flames from 4-16 atm.

determine particle size, this shifting of κ_a relative to Q_{vv} in areas of large gradients, particularly where values are small, could result in large over- or under-estimation of D_{63}. This demonstrates the difficulty in obtaining reliable LES measurements in flames with large gradients, such as elevated pressure diffusion flames.

Figure 5.8 shows a) D_{63} at 17 mm HAB for the 12 atm flame, and b) the contributions from each parameter to this uncertainty. Uncertainty in D_{63} is largely driven by uncertainty in κ_a. The largest uncertainty tends to fall at the flame edge, where κ_a is small, yet uncertainty in κ_a is large. The uncertainties due to optical properties are relative uncertainties, and scale with D_{63}.

Figure 5.9 shows radial profiles of measured d_p. The trends in d_p, with the assumed fractal properties, are similar to those of D_{63}. Peak d_p are nearly constant at 4 atm.

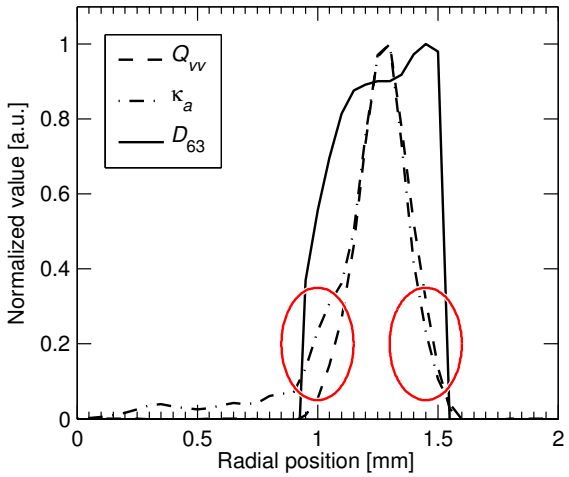

Figure 5.7: Q_{vv}, κ_a, and D_{63} (normalized by maximums) 4 mm above burner in a nitrogen-diluted ethylene flame at 16 atm. The circled regions show where a combination of uncertainty due to tomographic inversion and sharp gradients in Q_{vv} and κ_a may cause erroneous particle size calculation.

There is a large increase in d_p between 4 and 8 atm, and a continuing increase up to 16 atm. However, as with D_{63}, the increase between 12 and 16 atm is minimal. Thomson et al. [41] measured a similar increase in effective d_p in methane flames over the range of 5-40 bar, including the faster growth in the annulus. However, [41] did not observe a decrease in the growth with successive doublings of pressure. As the effective soot particle diameter of [41] is a function of d_p and N, and the measurements of this work assume D_f and k_f (and hence N), no conclusion can be drawn as to whether it is d_p, N, or both that is changing with pressure. Kim et. al [42] did observe a general increase in d_p with pressure, partially attributed to increased residence times, and partially due to increased reactant concentrations. However, the residence times in the fixed mass flowrate diffusion flames of this work are independent of pressure for a given HAB [36].

Figure 5.10 shows the peak values of f_v, D_{63}, and d_p, on flame centerline and in the annulus, as a function of pressure. While f_v and η_s have often been found to relate to pressure with a power-law scaling [26, 30, 34, 36, 41], here particle sizes can

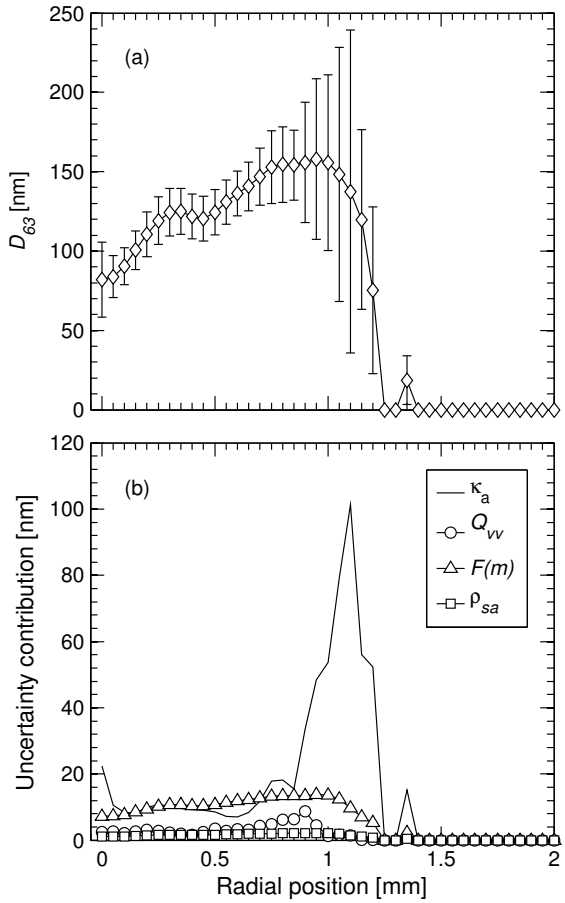

Figure 5.8: a) D_{63} 17 mm above burner in a nitrogen-diluted ethylene flame at 12 atm, b) Contributions to D_{63} uncertainty from absorption coefficient (κ_a), precision of scattering measurement (Q_{vv}), $F(m)$, and ρ_{sa}.

be seen to asymptote with pressure. Measured d_p on centerline are within the range of primary particle sizes that have been previously measured at atmospheric pressure.

Both D_{63} and d_p measurements indicate an increase in overall particle size with pressure, which is in agreement with previous high pressure studies [20, 41, 42]. Particle sizes increase more rapidly with pressure in the annulus of the flame. Growth with pressure was strongest at the lowest pressures (4-8 atm), and mostly ceases between 8 and 12 atm. This upper limit in particle size has not previously been observed in high pressure diffusion flames, though it has been observed in premixed flames. The differences in theses systems are too great to draw a comparative conclusion. Over-

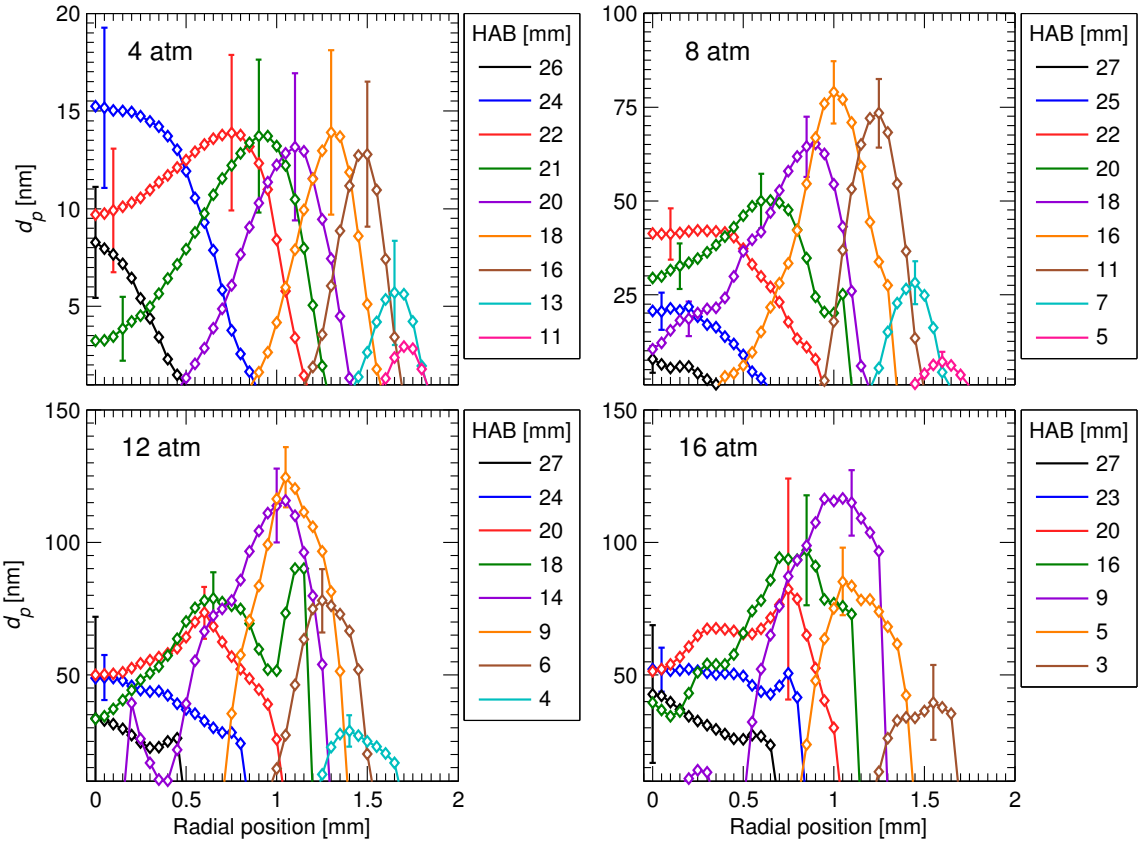

Figure 5.9: d_p at different HAB in nitrogen-diluted ethylene flames from 4-16 atm for $D_f = 1.7$ and $k_f = 2.4$.

all, the trends are similar to that of f_v: increasing pressure results in soot formation earlier in the flame, allowing more time for growth in size and concentration.

5.3.3 Growth and Oxidation Rates

With knowledge of soot concentrations and particle size, soot growth and oxidation rates can be calculated from

$$k_s = \pm \frac{\rho_s}{f_{sv}} \frac{\mathrm{d}f_v}{\mathrm{d}t} \tag{5.1}$$

where f_{sv} is the soot surface area per unit volume of gas, and the positive and negative values are considered to be the growth and oxidation, respectively [61]. Since D_{63} is an equivalent volume weighted diameter, it's surface area would not be representative.

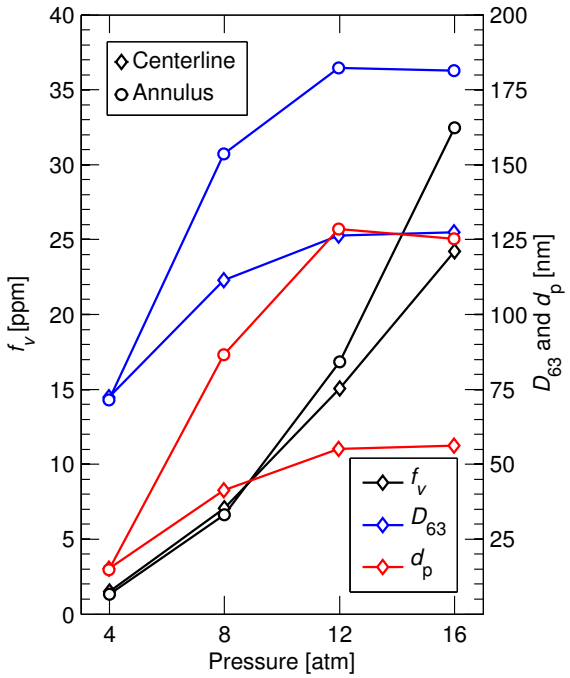

Figure 5.10: Peak values of f_v, D_{63}, and d_p (for $D_f = 1.7$ and $k_f = 2.4$) on the centerline and in the annulus of nitrogen-diluted ethylene flames from 4-16 atm.

Therefore, d_p is used to determine soot surface area. If particles are assumed to be comprised of spheres with no overlapping surface, particle surface area per unit volume can easily be determined as $f_{sv} = 6/d_p$. In order to relate f_v to residence time, it is assumed that axial velocity, $v_z = \sqrt{2az}$, where $a = 41$ m/s^2 [79, 90].

Figure 5.11 shows calculated growth and oxidation rates at 4 to 16 atm for centerline soot. Rates are plotted versus residence time, which has the same direct relation to HAB for each pressure. As pressures is increased from 4 to 12 atm, growth and oxidation both start earlier, and rates are higher. This is consistent with the increased reaction rates that accompany increases in pressure. However, while f_v is overall higher at 16 atm, growth rates are comparable between 12 and 16 atm.

Figure 5.12 shows the surface area of soot per unit volume in the flame at 12 and 16 atm. So, while growth rates are similar at both pressures, growth occurs earlier in time at 16 atm (Fig. 5.11), leading to more surface area for growth at a

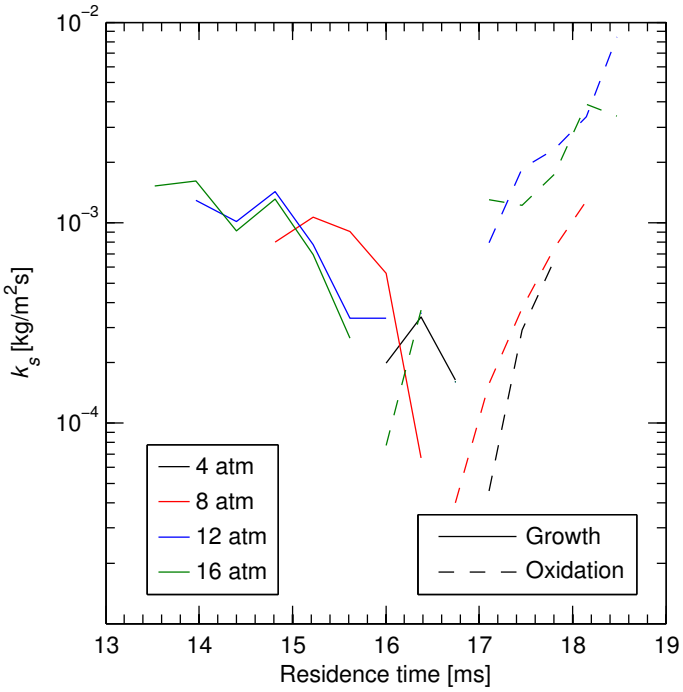

Figure 5.11: Growth and oxidation rates on particle surface of centerline soot for 4 to 16 atm.

given residence time. Similar growth rates will then lead to increased f_v at 16 atm compared to 12 atm.

5.4 Conclusions

This work includes the first measurements of two-dimensional soot volume fraction and particle size fields in nitrogen-diluted ethylene diffusion flames from 4-16 atm. This work, combined with previous studies in the same ISF target flame, provide further data for validation of numerical models. Major conclusions of the study are as follows:

In these flames, local peak f_v is found to scale with pressure as P^n with $n = 2.0$, 2.3, and 2.2 on the centerline, in the annulus, and globally, respectively, and peak soot yield is found to scale as $P^{1.8}$ over the pressure range of 4-16 atm. This scaling may differ from those in the literature, as the coflow velocity ratio was altered with

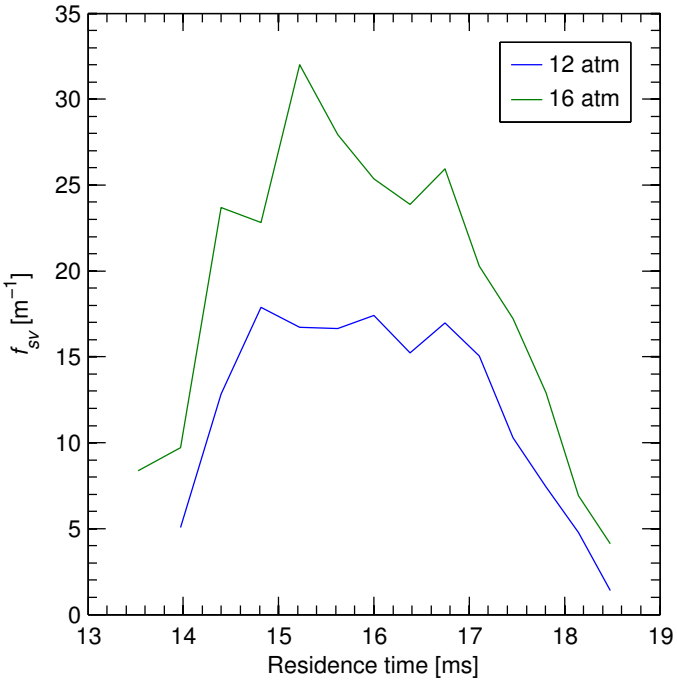

Figure 5.12: Soot surface area per unit volume of gas at 12 and 16 atm.

pressure.

Aggregate sizes are found to increase with pressure, consistent with previous studies [20, 41, 42]. Particle sizes increase more rapidly with pressure in the flame annulus. Large increases in particle sizes are observed between 4 and 8 atm, and little increase is observed between 12 and 16 atm. The observations combined with large uncertainties suggest the need for further experimental measurement.

Chapter 6

Time Resolved Laser Induced Incandescence at Elevated Pressures

6.1 Introduction

Understanding and improvement of LII is an active topic of research [94–99]. LII offers the ability to measure instantaneous 2-dimensional soot fields, even in unsteady flows. However, to accurately quantify soot concentrations or particle size, the complex physics of LII must be understood. One aspect of TiRe-LII that needs further examination is the influence of the laser pulse characteristics. Previous research has shown that spatial and temporal variations in a beam must be properly accounted for when selecting detection methodology [100]. However, little investigation has been done on the specific impacts of pulse duration and temporal shape.

LII simulations frequently assume mono-disperse particle sizes for simplicity. In cases where heat conduction is the main mode of energy loss (low fluence, high pressure), a single-exponential decay can accurately predict a monodisperse particle size from soot emissions [101]. However, realistic soot distributions are polydisperse, in both diameter and aggregate size. The contribution of a given particle classes emission to an overall LII signal is weighted by its f_v. When cooling from a given initial temperature, smaller particles cool faster than large particles due to their higher surface to volume ratio [99]. Therefore, the decay of LII signals does not follow a single-exponential decay. Emissions from small particles quickly become dominated by emissions from large particles. This results in a bias towards large particle classes

in single-exponential fitting.

Cenker et al. [99] proposed a novel particle sizing strategy, referred to as Two-Exponential Reverse Fitting (TERF). Since small particles cool faster, the early portions of LII signal decay can be thought of as small-particle dominant, while latter portions of the signal are dominated by large-particle emissions. In TERF, the latter portions of the signal are fit to determine a characteristic large particle diameter, $d_{p,large}$. The simulated LII signal for this particle size is extrapolated back to the end of the laser pulse. The difference between this extrapolated signal and the observed signal is attributed to the emission of small particles. From this, a characteristic small particle diameter, $d_{p,small}$ can be calculated, as well as the ratio of number densities of the two particle classes.

The peak temperature particles reach during LII depends on the balance of absorption and heat loss though various modes (see Section 3.3). Typically, a laser pulse of 6-10 ns Full Width at Half Maximum (FWHM) in duration is used. For pressures up to a few bar, absorption from the laser is dominant compared to cooling mechanisms, and all the particles being incandescenced will reach the same peak temperature at the end of the laser pulse. However, at elevated pressures energy loss through conduction is greatly enhanced (and hence timescales are greatly reduced), and all particles within an ensemble will not have the same final temperature [98, 102]. Due to their greater surface to volume ratio, small particles will be at a lower temperature. This non-uniformity in temperature must be accounted for to yield accurate particle size information. For single-exponential fitting, Cenker et al. [98] have shown that increased pressure enhances the bias towards large particles. In the case of TERF, the reduced timescales may make calculation of $d_{p,small}$ difficult, both due to shorter durations for fitting, and the unknown initial temperature of the small particles.

The simulations of Charwath et al. [102] suggest that LII pulses of shorter duration

could produce better results, as this effectively decouples the heating and cooling of the particle. However, good agreement between models and experiments was not achieved with a conventionl pico-second laser [103]. It has been suggested that short nano-second pulses, on the order of 1 ns, could be an ideal middle ground [97, 98].

In this work, laser pulses of varying duration, either Gaussian or tophat in temporal shape, are investigated in flames at 1 and 15 bar. The effect of pulse shape and duration on particle size calculations will be determined. The measurements will be used to validate the KAUST LII code.

6.2 Methodology

A description of the theory and setup of TiRe-LII is given in Section 3.3. In order to study the effect of pulse shape and duration, two lasers are used, and both lasers are tuned to produce variable beam pulse durations. By adjusting the delay between flashlamp and Q-switch timing, the duration of Gaussian pulses from the Quantel laser are set to 4, 6, and 10 ns (after aperture). Similarly, the delay between flashlamp and pulse-slicing in the Ekspla laser is adjusted to produce 1.6 and 6 ns tophat temporal profiles. The peak and area normalized temporal and spatial profiles of the beams, after aperturing, are shown in Fig. 6.1. It can be seen that the tophat temporal profiles, and those of shorter duration, deliver energy in a much shorter time-span, while the spatial variation between beams is negligible. Laser fluence is varied from 0.03 to 0.33 J/cm^2 as explained in Section 3.3. The minimum fluence is chosen based on where LII signals are first detected, and peak fluences are chosen to be well into the saturation regime, which will be explained in Section 6.3.

Flames are established on burner B4 (Section 2.1.2). The operating conditions are shown in Table 6.1. Pulse effects are investigated in a pure ethylene flame at 1 bar, and a nitrogen diluted ethylene flame at 15 bar. Ethylene and nitrogen are delivered through the burner nozzle, while the coflow is comprised of air. Figure 6.2 shows the

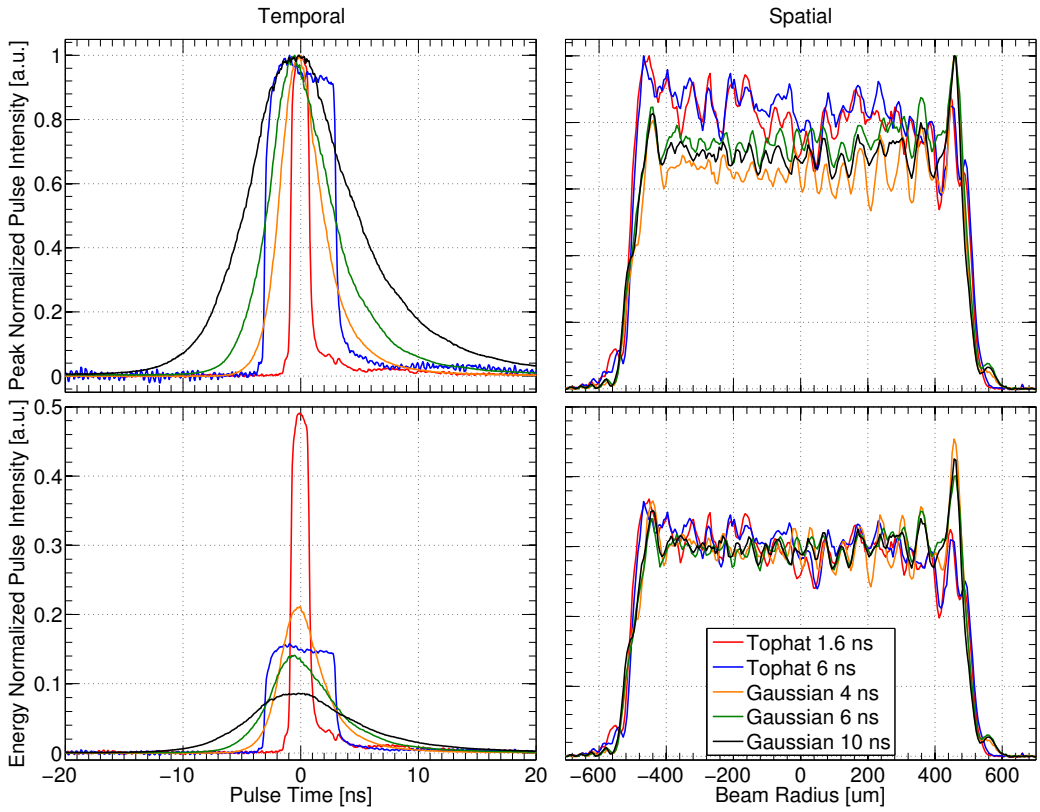

Figure 6.1: Peak and energy normalized temporal and spatial profiles of the laser pulses used in TiRe-LII.

soot field for each flame, with the region of interest shown with a black circle. The soot field is measured by DLE using Tikonov regularized onion peeling (Sections 3.2 and 3.5). The values of f_v listed in Table 6.1 are average values from the region of interest. TiRe-LII measurements are done 7 mm below flame tip at 1 bar, and 4 mm below flame tip at 15 bar. This is to ensure the soot is mature and is measured in an area of low gradients and high concentrations.

For each flame condition, each pulse is investigated sequentially. For each pulse, the entire range of fluences is investigated before switching to a different pulse. For each beam and fluence, 500 shots are averaged and recorded on the oscilloscope. Each measurement includes the temporal response of each PMT (red and blue LII channels) and the fast photodiode (beam temporal profile). During LII measurements, the detection system is tuned to accommodate the much higher intensities of

Table 6.1: Operating conditions for TiRe-LII experiments.

Pressure [bar]	$\dot{m}_{ethylene}$ [mg/s]	$Q_{ethylene}$ [sccm]	$\dot{m}_{nitrogen}$ [mg/s]	$Q_{nitrogen}$ [sccm]	$\dot{m}_{air}$ [g/s]	Q_{air} [slpm]	f_v [ppm]
1	1.46	70	0	0	0.65	30	3
15	0.94	45	4.58	220	1.5	70	30

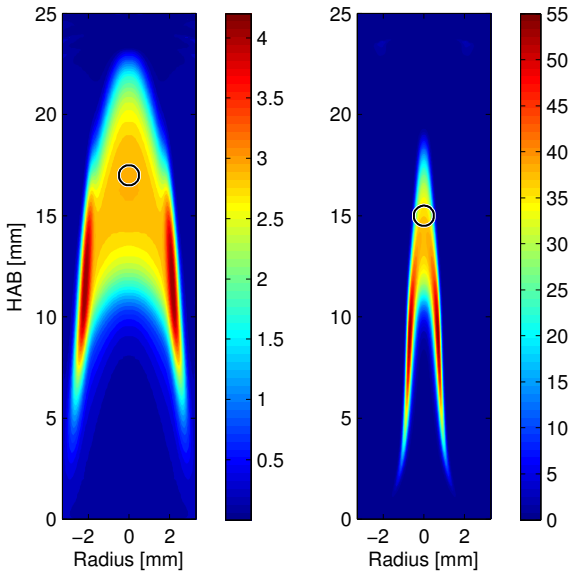

Figure 6.2: Soot volume fraction [ppm] measurements of the flames used for TiRe-LII experiments. Measurements done by DLE (Section 3.2). The proble volume for TiRe-LII is indicated with the black circles.

incandescence after laser heating, where the intensity scales with T^4. As a result, the baseline soot temperatures cannot be accurately measured simultaneously to LII measurement. Therefore, one measurement of baseline soot temperature is made for each laser shape/duration. Due to the low accuracy of temperature measurements when emissions are low compared to peak, temperature measurements during laser absorption are not accurate enough for meaningful assessment. Electronic noise is visible in the LII signals during tophat laser pulses. This is thought to be noise caused by the high voltage of the laser, which is in close proximity to the detectors.

6.3 Results

6.3.1 Incandescence Temperatures

Two-color pyrometry is first used to asses the baseline soot temperature in the probe volume. Measured soot temperatures range from 1940-1990 K at 1 bar, and 1860-1930 K at 15 bar. The average soot temperature is measured to be 1970 K at 1 bar, and 1900 K at 15 bar, and these temperatures are used as the assumed gas temperatures for LII simulations. A lower soot temperature is expected at elevated pressures, as the heat loss due to radiation increases with increasing f_v.

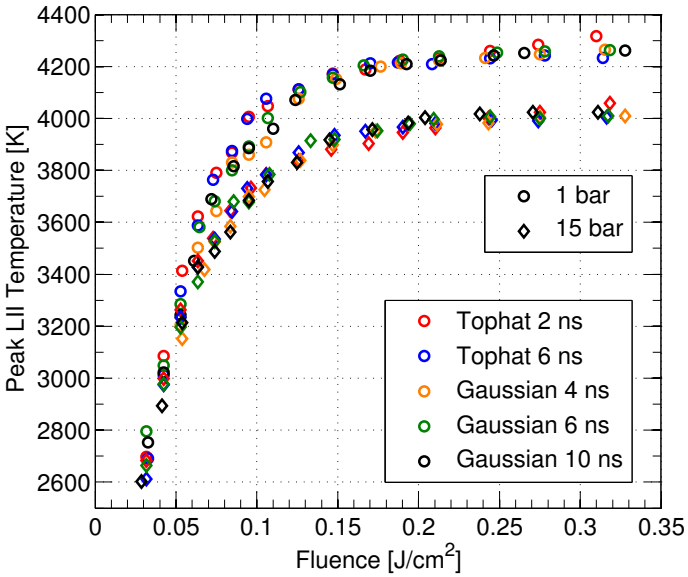

Figure 6.3: Peak soot temperatures during TiRe-LII.

The peak temperatures reached by the incandescent soot during LII are show Fig. 6.3. It should be noted that the two-color technique has an uncertainty of ±100 K. At both 1 and 15 bar, peak temperatures plateau above around 0.15 J/cm^2, where the soot reaches its sublimation temperature. Peak temperatures plateau at ∼4200 K at 1 bar, close to the sublimation temperature of C_3 (∼4140 K) [71]. In this saturation regime the dominant heat and mass loss mechanism is sublimation. The peak temperatures at 15 bar are lower than those at 1 bar for a given fluence. This is

expected, as enhanced cooling rates at elevated pressures limit the peak temperature [102]. The saturation temperature at 15 bar is ∼4000 K, whereas the sublimation temperature of graphite is expected to be higher than at 1 bar. However, Hofman et al. [104] suggest that simple thermodynamic consideration may not be sufficient to describe nano-second LII processes.

6.3.2 Incandescence Signals

Figure 6.4 shows the LII signals, relative to the laser pulse, for each pulse type at a low fluence of 0.053 J/cm^2. This fluence is chosen as significant soot sublimation may start occuring at around 3400 K [105]. Signals are aligned temporally such that time = 0 ns corresponds to an increase in normalized signal of 7%. The left column of plots is from experiments at 1 bar, and the right column is experiments at 15 bar. Each row represents a different laser pulse type. The pulse shape and duration has a noticeable effect on the heating of the soot particles. For tophat laser profiles, the increase in soot emissions is much quicker and more linear, at both pressures. There is an order of magnitude difference in the duration of this increase from the 1.6 ns pulse (∼2 ns) to the 10 ns Gaussian pulse (∼15 ns). For the Gaussian pulses, there is still laser absorption even after the point of peak emission. This indicates the heat loss due to conduction and radiation is greater than that absorbed. This phenomena is more noticeable at 15 bar, where the heat loss due to conduction is greatly enhanced. The increased conduction rates at 15 bar are also evident from the faster decay of both LII signals. To simplify TiRe-LII modeling, absorption is often neglected, and signal decays and temperatures are fit from a point after the laser pulse has ended. For long duration pulses at elevated pressures, the incandescence signal may have already decayed by 50% after just 40 ns. These plots suggest that for tophat laser profiles this may not be necessary, and more accurate fitting could be done from the point of peak temperature and emission.

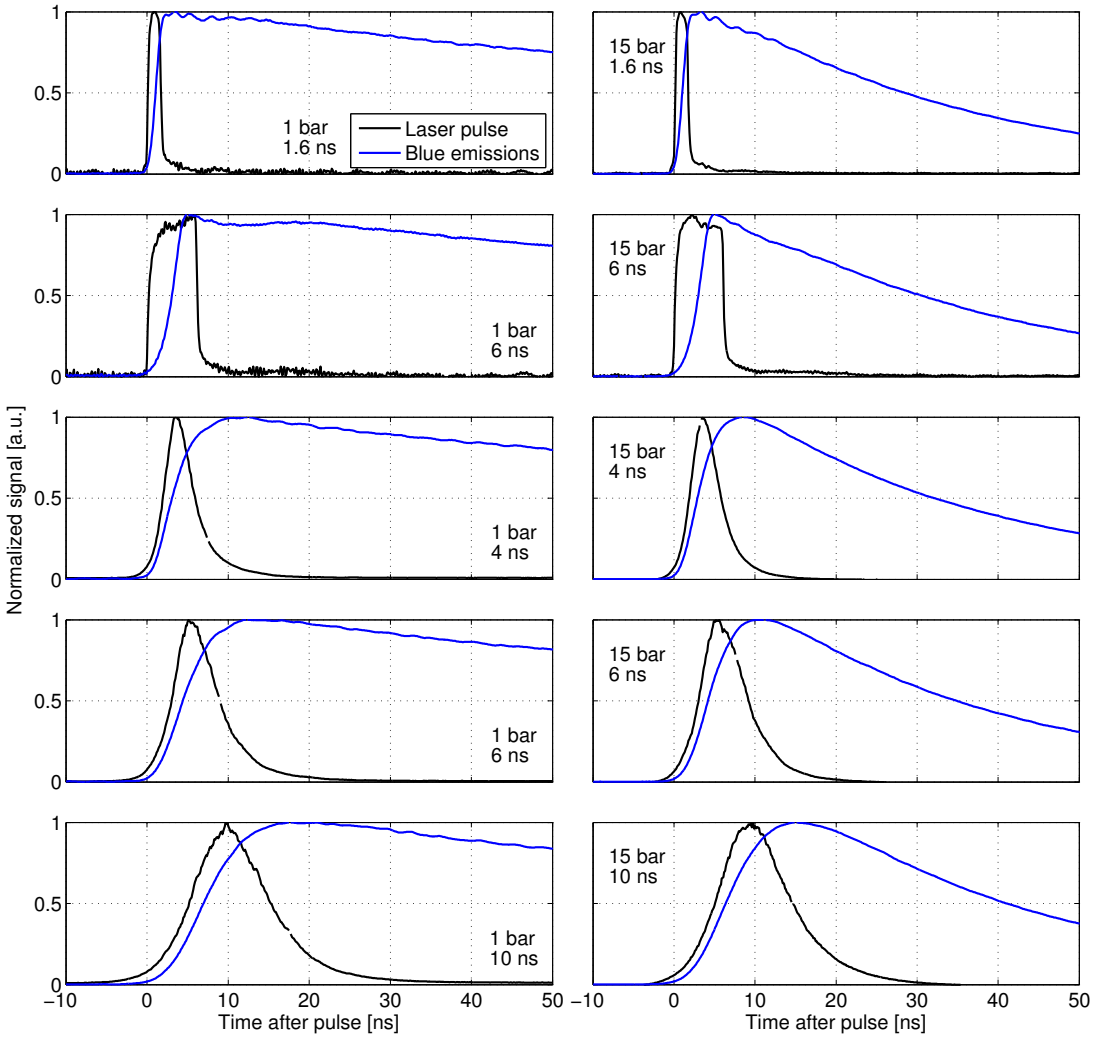

Figure 6.4: LII signals relative to laser pulse at a fluence of 0.053 J/cm^2.

Figure 6.5 shows LII signals at a higher fluence of 0.21 J/cm^2. At this fluence, sublimation is likely starting to occur (see Fig. 6.3). As with the low fluence cases, the rise in emission is much quicker and more linear for tophat laser profiles. However, here we start to see the effects of sublimation. At 1 bar, the soot emissions start to decrease during the laser pulses, and for the 10 ns pulse, even start to decay before the pulse has reached peak intensity. This is due to mass loss from sublimation. This effect is still visible at 15 bar with the 6 ns tophat pulse. For the longer pulses, the enhanced conduction rates may hide the reduction in emission due to mass loss.

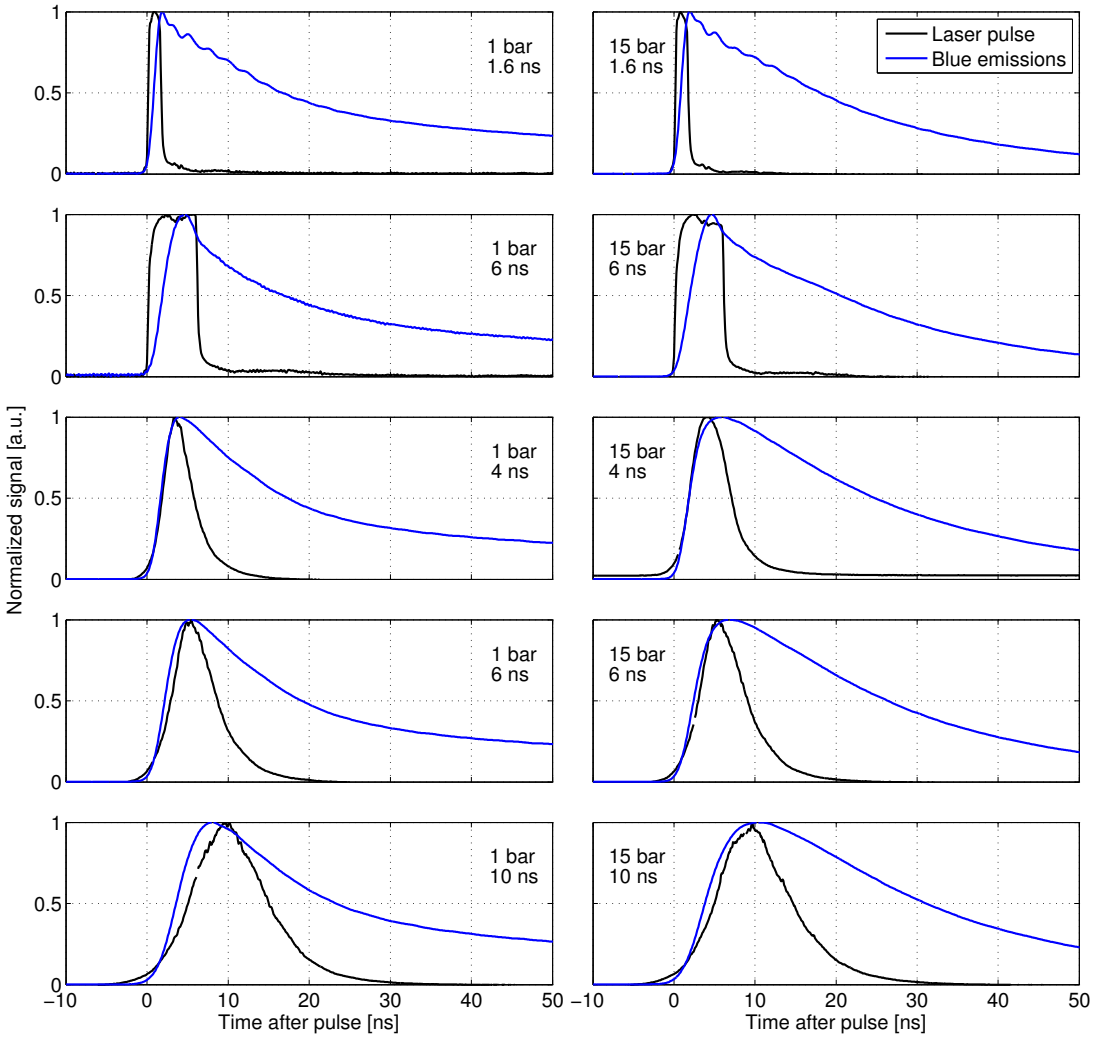

Figure 6.5: LII signals relative to laser pulse at a fluence of 0.21 J/cm^2.

6.3.3 Particle Size

Simulations are run using the KAUST LII code. For both 1 bar and 15 bar cases, fitting is done for sufficient time after peak temperatures for LII intensity to decay to 10% peak value. For 1 bar cases, simulations are run for $t = 20$ to $t = 300$ ns, and for 15 bar cases simulations are run for $t = 20$ to $t = 80$ ns. The McCoy and Cha conduction model is used for 1 bar cases, while the Fuchs model is used for 15 bar cases [69, 70]. For all simulations, $\alpha_T = 0.37$. The mono-disperse equivalent d_p for each laser pulse at a fluence of 0.053 J/cm^2 is shown in Table 6.3. The peak

temperatures (T_{peak}) and simulations initial temperatures, 20 ns after peak (T_{20}), are also shown.

Table 6.2: Mono-disperse equivalent d_p for varying laser pulse characteristics.

Pulse	Duration [ns]	1 bar T_{peak} [K]	1 bar T_{20} [K]	1 bar d_p [nm]	15 bar T_{peak} [K]	15 bar T_{20} [K]	15 bar d_p [nm]
Tophat	1.6	3413	3371	21.0	3263	3120	48.9
Tophat	6	3375	3295	21.1	3233	3104	49.1
Gaussian	4	3205	3170	23.0	3152	3013	49.8
Gaussian	6	3285	3252	22.3	3197	3053	49.9
Gaussian	10	3242	3205	22.2	3214	3090	50.2

Table 6.3: Mono-disperse equivalent d_p for varying laser pulse characteristics.

Pulse	Duration [ns]	1 bar T_{peak} [K]	1 bar T_{20} [K]	1 bar d_p [nm]	15 bar T_{peak} [K]	15 bar T_{20} [K]	15 bar d_p [nm]
Tophat	1.6	3413	3386	20.6	3263	3218	48.6
Tophat	6	3335	3296	21.2	3233	3194	

In general, tophat temporal profiles result in higher T_{peak}, at both 1 and 15 bar. This is expected, as absorption occurs over a shorter timescale. Regardless of pulse type, mono-disperse d_p is consistent for a given pressures. However, d_p is slightly smaller for tophat laser profiles. This could be a result of a more uniform temperature distribution within the poly-disperse ensemble after lasing, resulting in smaller bias towards the larger particles. Particles are measured to be much larger at 15 bar. As simulations start at $t = 20$ ns, small particles may have already significantly cooled by this point. This would cause a significant bias in d_p towards large particles. This could also explain why the difference in d_p between tophat and Gaussian profiles is smaller at 15 bar.

In order to fully realize the effect of pulse duration, the KAUST LII code must be adapted to include poly-dispersion. This is currently in progress.

6.4 Conclusions

A present time, the following conclusions can be drawn:

There is not a significant dependence of peak incandescence temperature on pulse shape or duration, though tophat profiles are generally $\sim$ 100 K higher. Saturation temperature is reached at the same fluence regardless of pulse shape or duration. Saturation temperature is lower in the 15 bar flame than the 1 bar flame. This could be due to differences in soot composition.

LII intensity increases much quicker, and more linearly, during absorption of tophat profiles, compared to Gaussian profiles. For Gaussian profiles, LII intensity starts to decay during the laser absoprtion, even at low fluences. The effect is more noticeable at elevated pressures.

Particle sizes are measured to be larger in the 15 bar flame. There could be a larger bias towards large particles due to the shorter timescales at elevated pressures. Poly-dispersity must be included in the KAUST LII model to further evaluate the effect of laser pulse duration.

Chapter 7

Sooting Tendencies of Liquid Fuels at Elevated Pressures

7.1 Introduction

Practical fuels, such as diesel and jet fuel, contain hundreds of species, which makes modeling of fuel chemistry very difficult. Fuel surrogates are often developed to facilitate modeling. Surrogates are simple fuels, comprised of a few individual components, which mimic the desired characteristics of a real fuel. One fuel characteristic that should be matched by its surrogate is sooting tendency. One way of characterizing sooting tendency is through a sooting index. Several indicies exist, including Threshold Soot Index (TSI) [106], Soot Temperature Index (STI) [107], and Yield Sooting Index (YSI) [108–110]. The most commonly used index is TSI, where the smoke point height of a fuel, H_{smoke}, is measured to determine TSI from its molecular weight, mw, and

$$\text{TSI} = \frac{mw}{H_{smoke}} \times A + B \tag{7.1}$$

A and B are constants which are selected to set the TSI of two reference fuels to desired values. This way, the *relative* sooting tendency of a fuel can be compared to the reference fuels or any others that are measured.

McEnally and Pfefferle [108] developed the YSI as an alternative to TSI. In YSI, the sooting tendency of a fuel is based on the peak soot volume fraction f_v measured in a methane coflow flame doped with the fuel of interest. f_v can be more reliably measured than smoke point. This is especially true of very soot fuels, as H_{smoke} is inversely proportional to sooting propensity. The use of small doping concentrations

(400 ppm of gas volume) allows for testing with fairly constant temperature and species fields at constant residence times. Methane, the simplest alkane, is used for the base flame as it should provide similar chemical pathways towards soot formation found in typical fuels, which are comprised largely of alkane components. In the study of McEnally [108–110], It was found that peak f_v would occur at a fixed HAB for all dopants. For this reason, f_v was measured by point-wise LII, at that fixed location. YSI is defined as

$$\text{YSI} = f_{v,max} \times C + D \tag{7.2}$$

where C and D are apparatus-specific parameters chosen to satisfy the YSI requirement of two reference fuels. Most recently [110], they were chosen to satisfy

$$\text{YSI} = \begin{cases} 0 & \text{for n-hexane} \\ 100 & \text{for benzene} \end{cases} \tag{7.3}$$

Another advantage of this method is that exact knowledge of soot optical properties is not needed, as these properties can be absorbed into the apparatus-specific constants. However, this still assumes that optical properties are consistent for each fuel, which may not be the case [111]. In general, YSI correlates well with TSI [108]. The flexibility of the YSI methodology has recently been investigated [111]. Kashif et al. demonstrated consistent YSI measurements even with much larger dopant concentrations (up to 6.14%). Additionally, they showed that evaluating YSI with peak $f_{v,a}$, peak centerline f_v, or global peak f_v produced comparable results [111].

While YSI has been useful in developing surrogates, the question still remains as to whether these YSI values are still representative of the relative sooting tendencies of fuels in real devices which operate at elevated pressures. As mentioned in the introduction (Section 1.3), there have been few investigations of liquid fuels in elevated pressure diffusion flames, though the number has grown recently. Pre-vaporization of

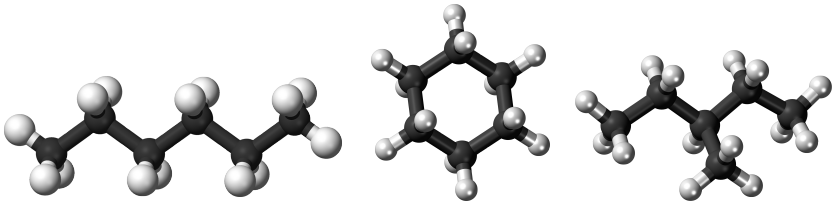

(a) n-hexane (b) cyclohexane (c) 3-methyl-pentane

Figure 7.1: Three C6-alkane isomers.

liquid fuels becomes problematic at elevated pressures, as the required vapor pressure for vaporization increases. Multi-component fuels make vaporization even more complex, as light species my vaporize before heavier species, altering the composition of the fuel, if care is not taken. The vaporization process has been reported to result in unstable flames [45]. One potential way to alleviate these problems is to dope liquid fuels into base flames of a gaseous fuel [43, 44, 46, 47].

While the literature on liquid fuel sooting tendencies at elevated pressures is growing, there is limited information on the effect of fuel structure [47]. For example, alkanes are saturated hydrocarbon chains featuring single-bonded carbons. These fuels can take various isomer forms, characterized in this study as either "normal", "cyclic", or "branched", as shown in Fig. 7.1. Normal and branched alkanes are acyclic, and have the form C_nH_{2n+2}. Normal alkanes, such as n-hexane (depicted in Fig. 7.1a), are the straight chain isomers. In methyl-alkanes, one or more of the hydrogen atoms is replaced by a methyl group (CH_3^-). Figure 7.1c shows a pentane molecule where a hydrogen atom on the third carbon is replaced with a methyl group, forming the C6 alkane 3-methyl-pentane. Cyclo-alkanes are the cyclic saturated hydrocarbons featuring single-bonded carbons, and have the form C_nH_{2n}. Cyclohexane is shown in Fig. 7.1b. All three molecules in Fig. 7.1 have the same number of carbon atoms, the main element of mature soot, similar bond types, and similar mw, yet have different propensities to soot.

Zhou et al. [47] investigated linear and cyclic C6 alkanes and alcohols doped into

n-heptane flames at different liquid volume fractions. They found that the cyclic and non-oxygenated molecules produced more soot. However, their investigation was limited to 2 bar.

The above paragraphs highlights the need for study of liquid fuels at elevated pressures, and identify the YSI methodology as an attractive method of investigation. For fuel comparisons, the YSI methodology is attractive for a few reasons. The low dopant concentrations minimize pre-vaporization complications. The independence from knowledge of soot optical properties is attractive due to the increased uncertainty in these values at elevated pressures. In order to answer several questions related to liquid fuel sooting tendencies at elevated pressures, the objectives of this study are to:

- Evaluate the consistency of the YSI methodology at elevated pressures
- Identify structural effects on a fuel's pressure sensitivity

7.2 Methodology

Coflow flames are established on burner B4t (Section 2.1.2) at 1, 5, and 10 bar. A base flame of pure methane or nitrogen diluted methane is doped with a liquid fuel of interest. The fuels chosen for this study are listed in Table 7.1. Alkane fuels are chosen for this initial study because they are the main components of petroleum-derived fuels and are widely available [110].

Fuels are selected to span a range of carbon numbers, with normal, cyclic, and branched isomers. In the work of McEnally et al. [110], YSI of branched alkanes with varying numbers of methyl groups, and varying positions of the methyl group, were measured. The relative difference in sooting tendency between fuels with a given number of carbon atoms and methyl groups did not depend heavily on the location of the methyl group. However, The number of methyl groups did affect the sooting

Table 7.1: Liquid fuels for YSI investigation.

	Normal	YSI[1]	Cyclic	YSI[1]	Branched	YSI[1]
C6	n-hexane	0.0[2]	cyclo-hexane	19.1	3-methyl-pentane	12.2
C7	n-heptane	8.7	cyclo-heptane	30.4		
C8	n-octane	18.9	cyclo-octane	42.4	2-methyl-heptane	29.5
C10	n-decane	41.7				
C12	n-dodecane	64.2[2]			2,2,4,6,6-pentamethyl-heptane	106.9

[1]YSI values from [110]. [2]Reference fuel for this work.

tendency. In this study, two methyl-alkanes and one pentamethyl-alkane are studied. In previous studies [110], benzene was used as a reference fuel. As the relative sooting tendancy of aromatics may respond differently to pressure than alkanes, two alkanes are chosen as the reference fuels in this study. This will allow the consistency of the relative measurements of sooting tendency between alkanes to be measured. The constants C and D from equation 7.2 are chosen to satisfy

$$\text{YSI} = \begin{cases} 0 & \text{for n-hexane} \\ 64.2 & \text{for n-dodecane} \end{cases} \tag{7.4}$$

where the YSI of n-dodecane is chosen to match that of [110].

Table 7.2 shows the experiment conditions. All flow parameters are maintained constant in the 1 and 5a cases. However, the flames have significantly different soot concentrations. The 5b configuration is selected to produce a less sooty flame at 5 bar, to see if the base flame soot concentrations play a factor in the efficacy of the YSI methodology. The conditions at 10 bar are chosen to keep the flame similar in size and sootiness to the 5b case. As the flames change significantly in size and soot concentration at each condition, different values of the constants C and D are determined for each condition. The coflow air and burner are maintained at 100 °C to prevent condensation of the liquid fuel. This limits the dopant concentration to about 2000 ppm for the heaviest species at 10 bar. The dopant concentration limit

Table 7.2: Experimental conditions for YSI investigation.

Flame	Pressure [bar]	Q_{Air} [slpm]	Q_{CH_4} [sccm]	Q_{N_2} [sccm]	Q_{Dopant} [ppm]	f_v [ppm]	H [mm]
1	1	70	75	0	3500	0.05	13
5a	5	70	75	0	3500	15	17
5b	5	140	70	50	1500	5	17
10	10	140	75	135	1500	7	19

is confirmed by increasing dopant concentration until a plateau in flame luminosity is observed. Higher temperatures cause noticeable instabilities in the flame, thought to be due to air entrainment through the chimney door (see Section 2.1.2).

Previous research has shown the location of peak f_v to be inconsistent, especially at elevated pressures, so a two-dimensional measurement technique is desired. Soot volume fraction is measured by DLE (Section 3.2). 100 images each of I and I_0 are averaged for each measurement, and three measurements are made for each dopant. In the original methodology, only the peak f_v is used to calculate YSI. Here, measurements are made of the base flame before each doped flame measurement. The difference between the doped and undoped measurements is then used to calculate YSI. This is to account for potential small variations in pressure. For a nominally constant base flame, this is mathematically identical to the original methodology. Data is binned 25 times vertically, and 2 times radially, resulting in an axial resolution of 500 μm and a radial resolution of 40 μm. Local values of κ_e are determined from Tikonov regularized onion peeling (Section 3.5) of line-of-sight values.

7.3 Results

Figure 7.2 shows the measured f_v for each of the reference fuels, as well as the undoped flames, at each experimental condition. Each row represents a different experimental condition. The left column of each column pair shows the soot field in the undoped flame, while the right column of each pair shows the soot field when doped with

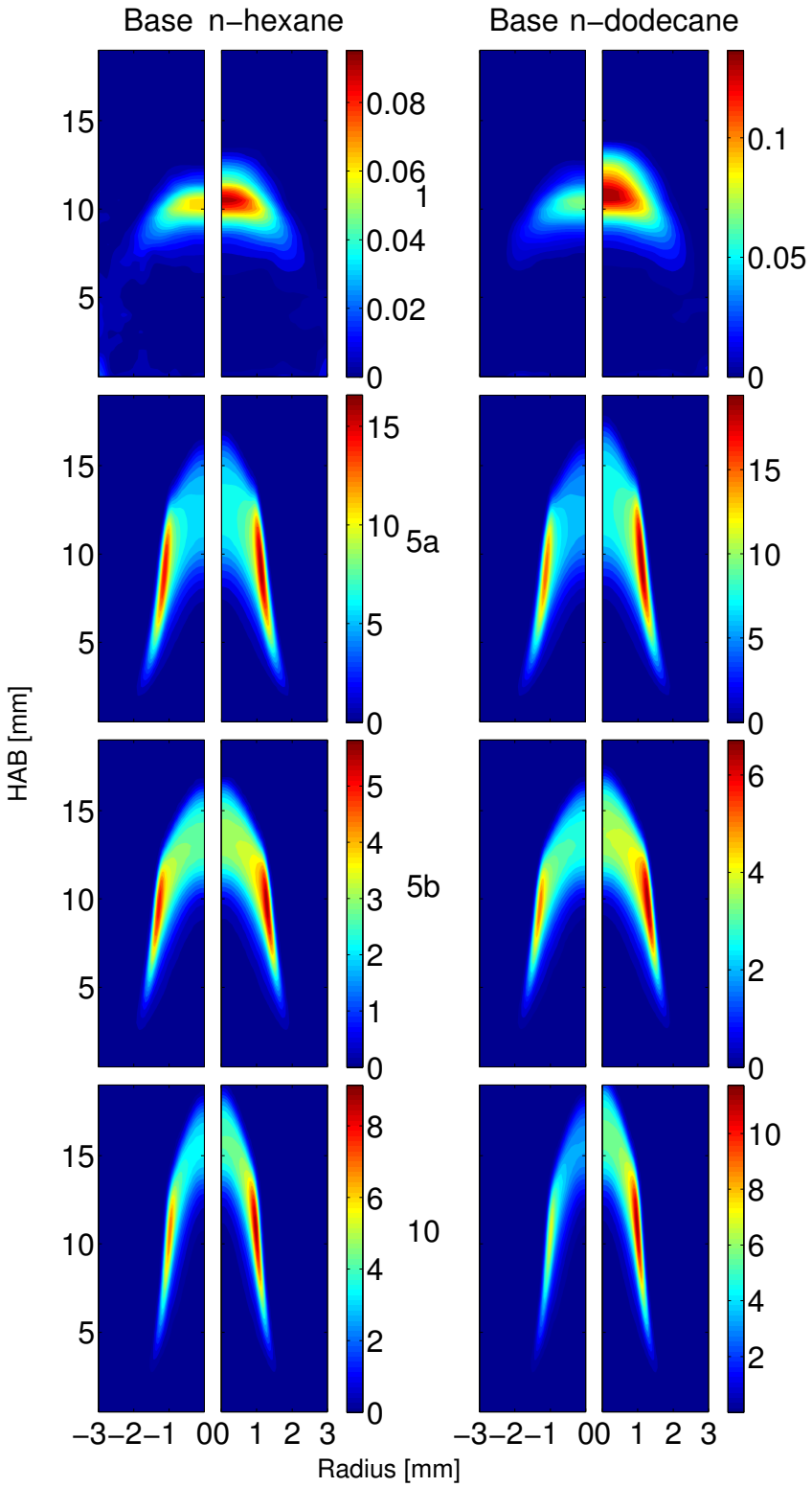

Figure 7.2: Measured f_v [ppm] in base methane flames doped with either n-hexane or n-dodecane.

either n-hexane or n-dodecane. Each column pair is shown with the same color scale to highlight the change in concentration with doping. The significant change in flame shape between conditions is noticeable, while the change from the base flame to doped flames at each condition is relatively minor. As expected, n-dodecane doped flames are more sooty than n-hexane doped flames. The soot field is concentrated at the flame tip at 1 bar, and is annular in shape at elevated pressures. This may be of importance, as some studies have suggested that the dominant pathway for soot formation may be different on centerline and in the flame annulus depending on pressure [112].

First, the reproducability of YSI in the present burner is evaluated. Figure 7.3 shows the measured YSI of each fuel compared to the values measured by McEnally [110]. Error bars represent the standard error of repeated measurements. The black line indicates the ideal case of the measured values matching those of McEnally, while the dotted lines indicate the confidence interval of McEnally [110]. It should be noted that the present values of YSI are set to match those of McEnally at YSI = 0 and 64.2.

Within experimental error, most of the YSI values measured are in agreement with the original measurements [110]. However, there are two discrepancies; benzene and isododecane (2,2,4,6,6-pentamethyl-heptane). This discrepancie with benzene has been observed before [111], and has been attributed to a difference of optical properties due to benzene's larger C/H ratio. The discrepancy with isododecane suggests further experimentation is necessary. In general, the methodology applied to the present burner is consistent with previous measurements.

The measured YSI of the n-alkanes is shown for each condition in Fig. 7.4. The black lines indicates confidence interval of McEnally's measurements [110]. It should be noted that the YSI scale is set to match those of McEnally at carbon numbers of 6 (n-hexane) and 12 (n-dodecane). As formation pathways may differ on centerline and

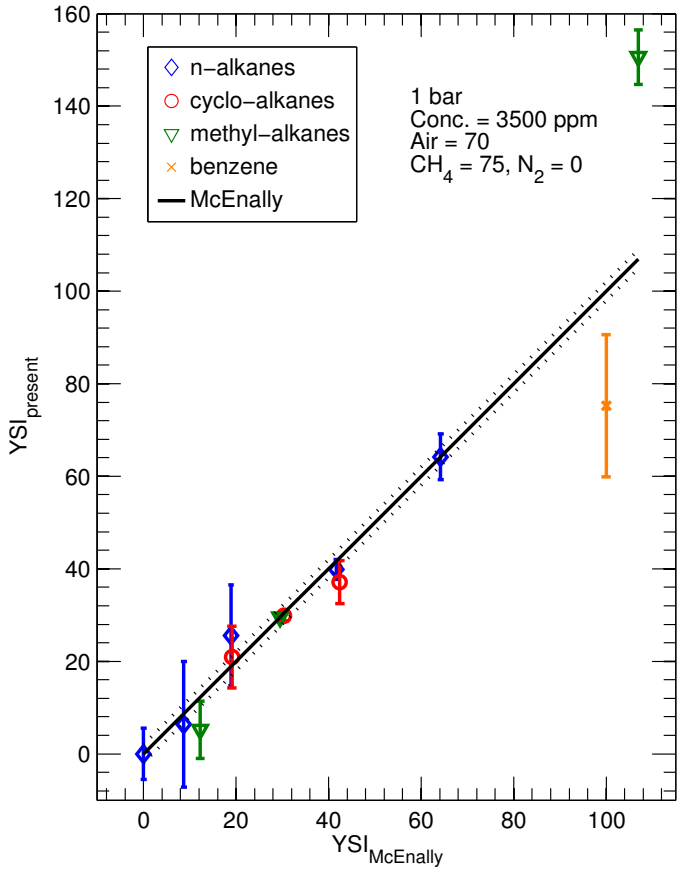

Figure 7.3: Measured YSI

in the annulus, YSI is evaluated from the peak values of f_v in each of these regions for each condition. However, as peak f_v is on centerline for the 1 bar case, only centerline YSI is evaluated. In addition to the previously mentioned agreement at 1 bar, the presently measured YSI values are in good agreement regardless of pressure, dopant concentration, and base flame soot concentration. This suggests that the relative sooting tendencies for fuels of the same structure behave similarly under a range of conditions. This could be expected, as two n-alkanes are used as the reference fuels. The error bars represent standard error from triplicate measurements. Error is largest at 1 bar, where the soot concentrations measured (Fig. 7.2) are close to the detection limit of DLE.

Figure 7.5 shows the measured YSI for the cyclo-alkanes, with dotted lines indicat-

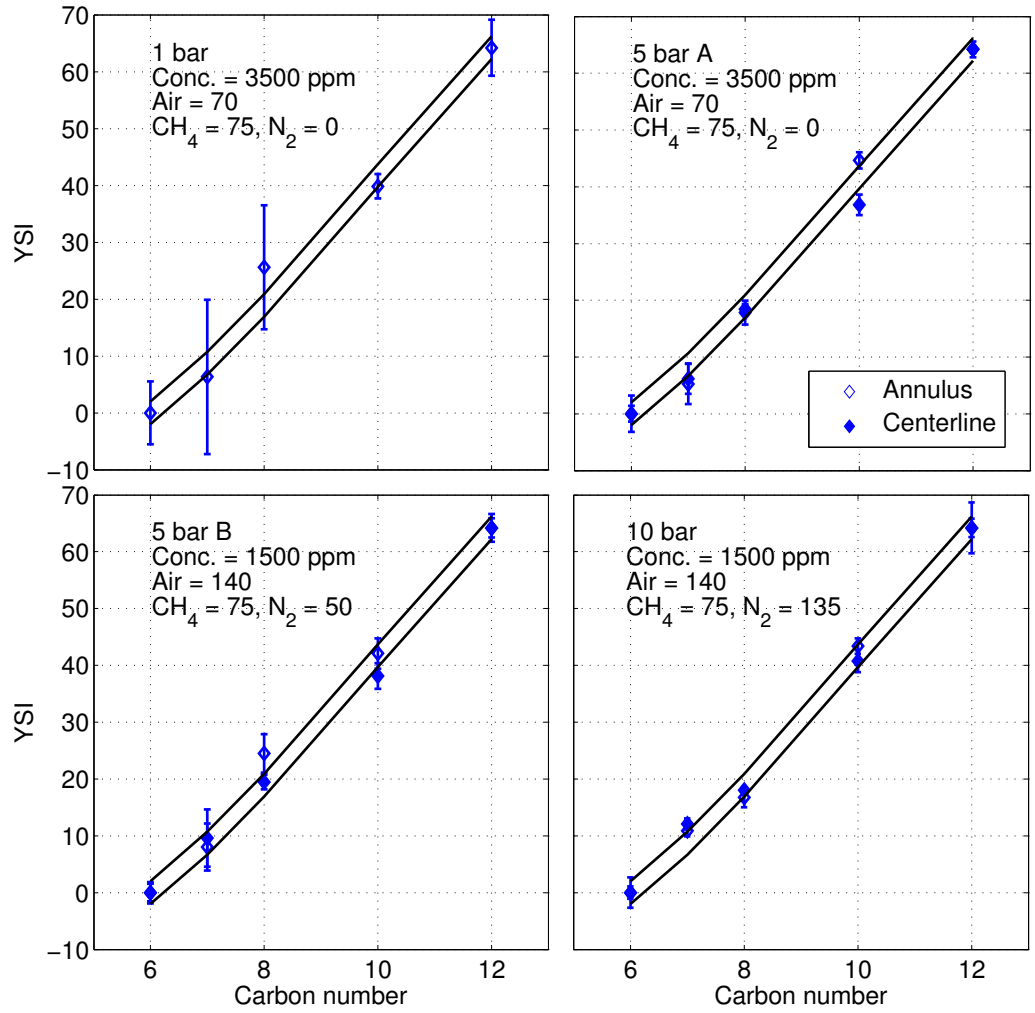

Figure 7.4: Measured YSI for n-alkanes.

ing the confidence interval of the literature values. Above 1 bar, YSI is consistently measured lower than in the literature. This would indicate cyclo-alkanes are less sensitive to pressure than n-alkanes, as the soot yield at elevated pressures is not at high as expected. In case 5b, cyclooctane doped flames are even less sooty than n-octane flames. However, this is not observed in the 5a or 10 cases. The peculiar behavior of the relative sooting tendencies of cyclo-alkanes in case 5b suggests possible experimental error, particularly considering the spread in triplicate measurements.

Measured YSI of methyl-alkanes is shown in Fig. 7.6, with dashed lines indicating literature values. As the sooting tendency of methyl-alkanes depends on both the

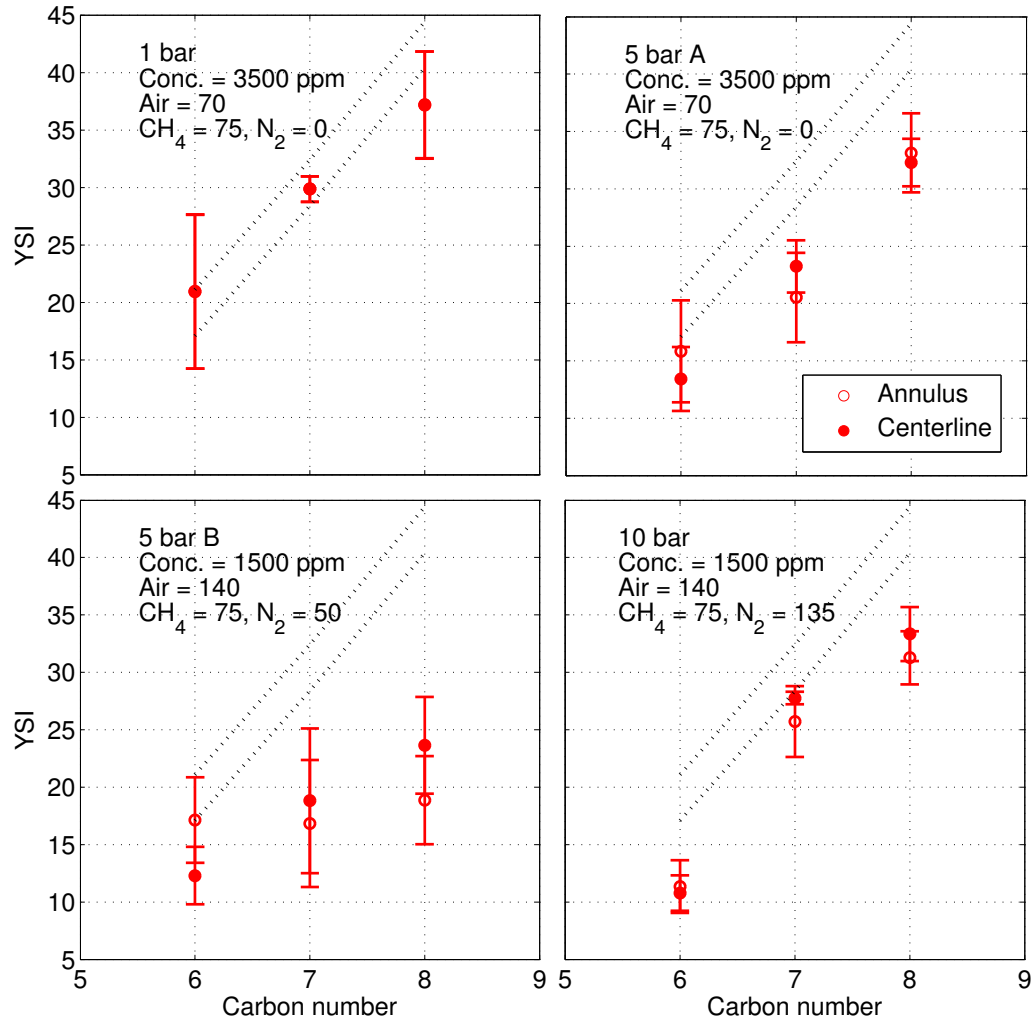

Figure 7.5: Measured YSI for cyclo-alkanes.

number and position of the methyl groups, only the literature values for the methylalkanes measured in this study, including two methyl-alkanes and one pentamethylalkane, should be inferred from the dashed lines. As with the cycloalkanes, the methylakanes appear to have less sensitivity to pressure than n-alkanes, though to a lesser extent.

Data for all fuels presently studied are shown in Fig. 7.7. The measurements indicate that cyclo- and methyl-alkanes could be less sensitive to pressure than n-alkanes. However, the measurements of benzene doped flames show a surprising

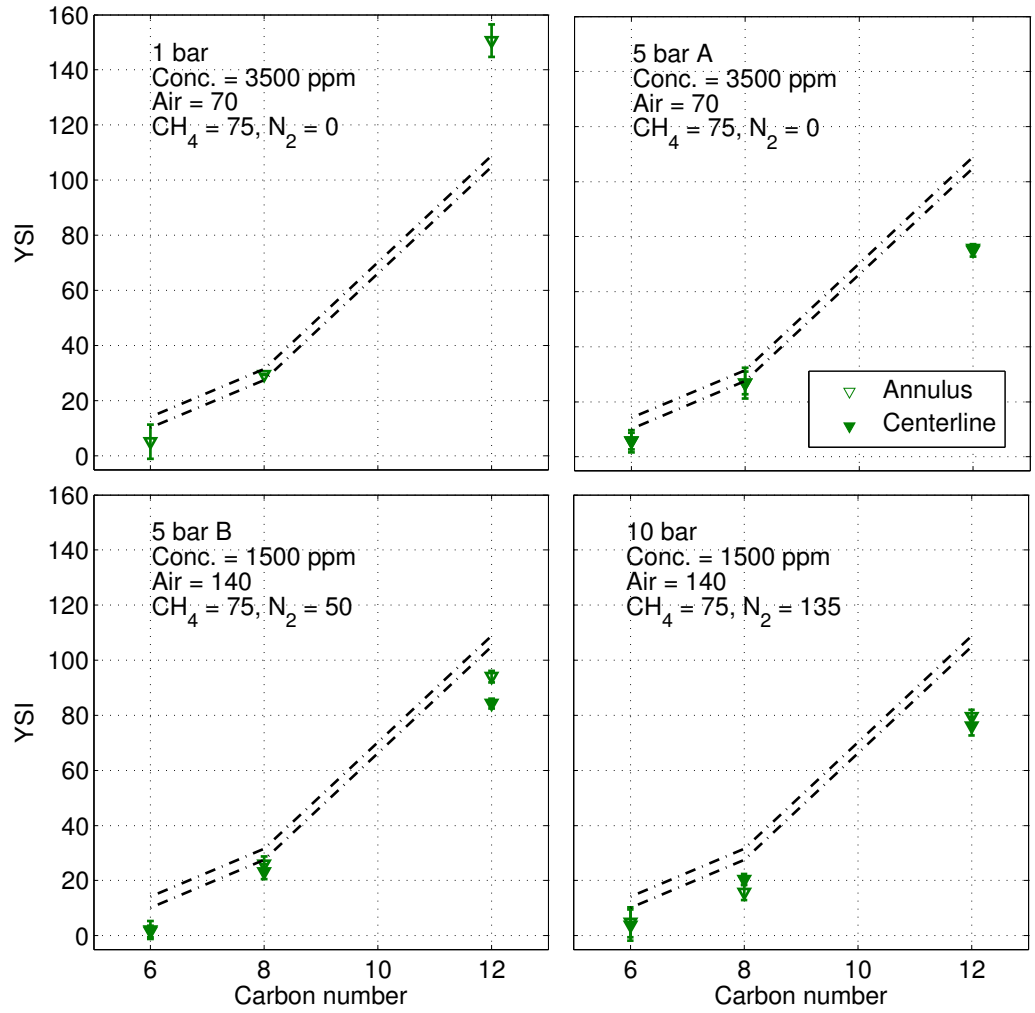

Figure 7.6: Measured YSI for methyl-alkanes.

result. In the 5b and 10 bar cases, benzene appears less sooty than expected. Recent work by Daca et al. [113] show that toluene doped flames have a lower pressure sensitivity than n-heptane doped flames. They attribute this to the reduced pyrolysis of benzene and toluene above 2-3 bar. However, the discrepancies in measurements between the 5a and 5b cases suggest further study is needed before conclusions can be drawn.

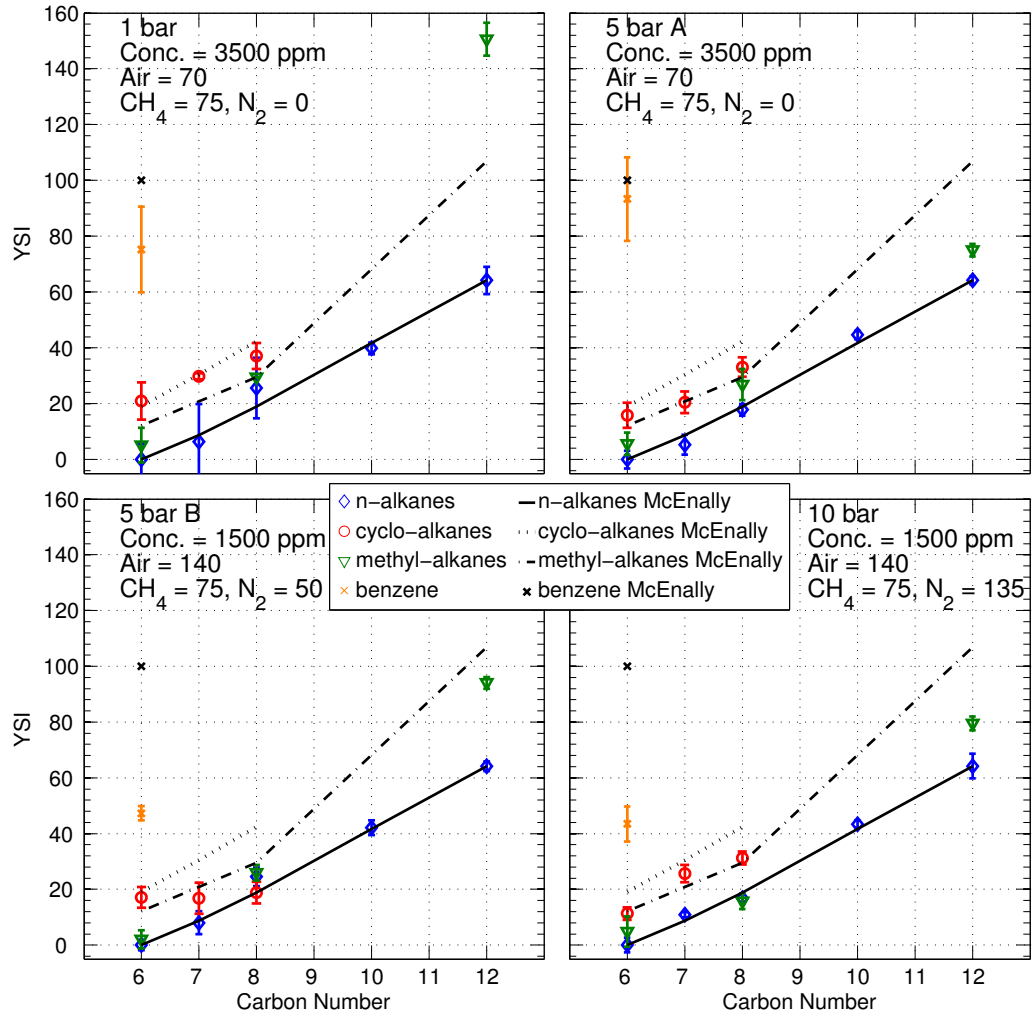

Figure 7.7: Measured YSI for alkanes and benzene.

7.4 Conclusions

The relative sooting tendency of 12 liquid fuels is investigated at pressures up to 10 bar. The YSI methodology is applied to facilitate measurements and comparisons. Major conclusions are as follows:

The relative sooting tendency of n-alkanes at 5 and 10 bar are consistent with those measured at atmospheric pressure. The holds for different soot loads, dopant concentrations, and flame shapes, consistent with previous studies [111]. This suggests replacing one n-alkane in a surrogate would have a predictable effect on the

sooting tendency of that surrogate, even in an elevated pressure application.

Cyclo- and methyl-alkane sooting tendencies have relatively lower pressure sensitivity compared with n-alkanes.

Due to some inconsistencies in the measurements, further experimentation is required. These measurements should clarify if there are apparatus specific effects on sooting tendency, and if optical properties are responsible for observed discrepencies between studies [110, 111].

Chapter 8

Conclusions and Future Work

Chapter 1 outlined the need for an understanding of soot formation at elevated pressures. It also showed several areas in which our understanding is lacking. The experimental apparatus required for these studies is somewhat unique, so even fundamental information is difficult to obtain. Therefore, several different paths of investigation are followed in the present work.

In the course of measuring particle sizes in the ISF flame, evaluating YSI at elevated pressures, and collaboration with numerical modelers, several questions about the behavior of coflow flames have arisen. The effect of coflow velocity and the general practice of investigating the pressure scaling of soot at constant mass flow rate are questioned. Therefore, the stability, scaling, and soot suppression of coflow flames at elevated pressures is investigated. Images and soot volume fraction measurements are made in a number of flames spanning the three-dimensional space of Gr/Re/r_u. The limits of stability of coflow flames in this space is evaluated. The ability to scale flames in this space is investigated by changing pressure and nozzle diameter. The effect of r_u on soot is also investigated. The major outcomes of these investigations are the following:

- Over the range of Re investigated, Gr is a reasonable predictor of flame stability. The limiting value of Gr for stable flames is dependent on r_u and Re, and may differ for burners of different design.

- Flame shape, for a given fuel, can be sufficiently described by Gr (or Ri) and

Re. Flames scaled in pressure by using nozzles of different diameters show self-similar shape, soot fields, and soot yield profiles.

- An alternative method of scaling flames in pressure is proposed. Scaling flames at constant Re and Gr reduces the effect of hydrodynamic changes on soot yield by scaling scalar dissipation rate in a controlled way. Soot yield in flames scaled at constant Re and Gr have a weaker pressure dependence than flames scaled at constant $\dot{m}$ over the same pressure range.

- The ratio of coflow to nozzle velocities plays an important role in stabilizing flames. Increased coflow rate can enhance flame stability and suppress soot. The suppression of soot is correlated to the relative importance of buoyancy of the flame, with less buoyant flames more susceptible to soot. The most suitable r_u depends on the P and Re of interest.

Future work in this area should include:

- Numerical studies which investigate the scaling of flames at constant Re and Gr.

- Numerical studies to further characterize how flow parameters may affect stability and the suppression of soot.

Soot concentration and particle size measurements are added to the ISF data set for pressurized laminar coflow flames. This work includes the first measurements of two-dimensional soot volume fraction and particle size fields in nitrogen-diluted ethylene diffusion flames from 4-16 atm. This work, combined with previous studies in the same ISF target flame, provides further data for validation of numerical models. Major conclusions of the study are as follows:

- In these flames, local peak f_v is found to scale with pressure as P^n with $n =$ 2.0, 2.3, and 2.2 on the centerline, in the annulus, and globally, respectively,

and peak soot yield is found to scale as $P^{1.8}$ over the pressure range of 4-16 atm. This scaling may differ from those in the literature, as the coflow velocity ratio was altered with pressure. However, the effect is expected to be minor.

- Aggregate sizes are found to increase with pressure, consistent with previous studies [20, 41, 42]. Particle sizes increase more rapidly with pressure in the flame annulus. Large increases in particle sizes are observed between 4 and 8 atm, and little increase was observed between 12 and 16 atm. The observations combined with large uncertainties suggest the need for further experimental measurement.

In order to validate previous particle size measurements, and enable the same measurements in more challenging environments, the development of TiRe-LII is necessary. A better understanding of the effect of laser pulse temporal shape and duration is sought. While development of the KAUST LII model is still ongoing, the following conclusions can be reached:

- There is not a significant dependence of peak incandescence temperature on pulse shape or duration, though tophat profiles are generally $\sim$ 100 K higher. Saturation temperature is reached at the same fluence regardless of pulse shape or duration. Saturation temperature is lower in the 15 bar flame than the 1 bar flame. This could be due to differences in soot composition, or error in measurement due to changes in soot optical properties.

- LII intensity increases much quicker, and more linearly, during absorption of tophat profiles, compared to Gaussian profiles. For Gaussian profiles, LII intensity starts to decay during the laser absoprtion, even at low fluences. The effect is more noticeable at elevated pressures.

- Particle sizes are measured to be larger in the 15 bar flame. There could be a larger bias towards large particles due to the shorter timescales at elevated

pressures. Poly-dispersity must be included in the KAUST LII model to further evaluate the effect of laser pulse duration.

Future work in this area should include:

- TiRe-LII of particles with known size distribution.
- Simulations of LII signals from particles with a variety of size distributions.

As we gain understanding of soot formation in flames of simple fuels at elevated pressures, focus will eventually need to turn to realistic fuels. As the current understanding of soot formation from liquid fuels is limited, the sooting tendencies of several alkanes is investigated. To facilitate comparisons, and at the same time validate the methodology for use in engine surrogate development, the YSI is used. The relative sooting tendency of 12 liquid fuels is investigated at pressures up to 10 bar. The major conclusions are as follows:

- The relative sooting tendency of n-alkanes at 5 and 10 bar are consistent with those measured at atmospheric pressure. The holds for different soot loads, dopant concentrations, and flame shapes, consistent with previous studies [111]. This suggests replacing one n-alkane in a surrogate would have a predictable effect on the sooting tendency of that surrogate, even in an elevated pressure application.
- Cyclo- and methyl-alkane sooting tendencies have relatively lower pressure sensitivity compared with n-alkanes.

Future work in this area should include:

- Investigations to clarify if there are apparatus specific effects on sooting tendency, and if optical properties are responsible for observed discrepencies between studies [110, 111].

- Investigation of other major fuel groups at elevated pressures.

- Investigation of alternative base flame fuels. The relative sooting tendency of components in fuels containing significant fractions of non-alkane components may be different. Additionally, possible chemical synergistic effects [114] may be elucidated.

Each of these investigations are only a starting point towards a further understanding of soot formation. There is still disparity between experimental measurement and numerical modeling of these types of flames, even with gaseous fuels. While predictive capability of real devices is still a long way off, further work in each of these investigative paths can eventually change this.

REFERENCES

[1] I. M. Kennedy, The health effects of combustion-generated aerosols, Proceedings of the Combustion Institute 31 (2) (2007) 2757–2770.

[2] U. Pöschl, Atmospheric aerosols: composition, transformation, climate and health effects, Angewandte Chemie (International ed. in English) 44 (46) (2005) 7520–40.

[3] T. C. Bond, S. J. Doherty, D. W. Fahey, P. M. Forster, T. Berntsen, B. J. DeAngelo, M. G. Flanner, S. Ghan, B. Kärcher, D. Koch, S. Kinne, Y. Kondo, P. K. Quinn, M. C. Sarofim, M. G. Schultz, M. Schulz, C. Venkataraman, H. Zhang, S. Zhang, N. Bellouin, S. K. Guttikunda, P. K. Hopke, M. Z. Jacobson, J. W. Kaiser, Z. Klimont, U. Lohmann, J. P. Schwarz, D. Shindell, T. Storelvmo, S. G. Warren, C. S. Zender, Bounding the role of black carbon in the climate system: A scientific assessment, Journal of Geophysical Research: Atmospheres 118 (11) (2013) 5380–5552.

[4] S. Menon, J. Hansen, L. Nazarenko, Y. Luo, Climate effects of black carbon aerosols in China and India, Science 297 (5590) (2002) 2250–3.

[5] M. Z. Jacobson, Short-term effects of controlling fossil-fuel soot, biofuel soot and gases, and methane on climate, Arctic ice, and air pollution health, Journal of Geophysical Research 115 (D14) (2010) D14209.

[6] I. S. Diakunchak, Performance Deterioration in Industrial Gas Turbines, Journal of Engineering for Gas Turbines and Power 114 (2) (1992) 161. `arXiv:27113049`,

[7] B. R. Stanmore, J. F. Brilhac, P. Gilot, The oxidation of soot: A review of experiments, mechanisms and models, Carbon 39 (15) (2001) 2247–2268.

[8] B. S. Haynes, H. G. Wagner, Soot Formation, Progress in Energy and Combustion Science 7 (1981) 229–273.

[9] C. S. McEnally, L. D. Pfefferle, B. Atakan, K. Kohse-Höinghaus, Studies of aromatic hydrocarbon formation mechanisms in flames: Progress towards closing the fuel gap, Progress in Energy and Combustion Science 32 (3) (2006) 247–294.

[10] J. S. McArragher, K. J. Tan, Soot Formation at High Pressures: A Literature Review, Combustion Science and Technology 5 (1) (1972) 257–261.

[11] H. Mätzing, H. G. Wagner, Measurements about the influence of pressure on carbon formation in premixed laminar C2H2-air flames, Twenty-First Symposium (International) on Combustion (1986) 1047–1055.

[12] H. Bohm, C. Felderman, H. Jander, B. Lüers, H. G. Wagner, Soot formation in premixed C2H4-air flames for pressures up to 100 bar, Twenty-Fourth Symposium (International) on Combustion (1992) 991–998.

[13] T. Heidermann, H. Jander, H. G. Wagner, Soot particles in premixed C H air-fames at high pressures (P=30-70 bar), Physical chemistry chemical physics : PCCP 1 (1999) 3497–3502.

[14] J. Singh, M. Balthasar, M. Kraft, W. Wagner, Stochastic modeling of soot particle size and age distributions in laminar premixed flames, Proceedings of the Combustion Institute 30 (1) (2005) 1457–1465.

[15] H. Kellerer, A. Müller, H.-J. Bauer, S. Wittig, Soot Formation in a Shock Tube under Elevated Pressure Conditions, Combustion Science and Technology 113 (1) (1996) 67–80.

[16] H. Kellerer, R. Koch, S. Wittig, Measurements of the growth and coagulation of soot particles in a high-pressure shock tube, Combustion and Flame 120 (1-2) (2000) 188–199.

[17] D. B. Kittelson, Engines and nanoparticles: A review, Journal of Aerosol Science 29 (5-6) (1998) 575–588.

[18] R. L. Schalla, T. P. Clark, G. E. McDonald, Formation and combustion of smoke in laminar flames, Tech. rep., National Advisory Committee for Aeronautics (1954).

[19] I. M. Miller, H. G. Maahs, High-pressure flame system for pollution studies with results for methane-air diffusion flames, Tech. Rep. June, National Aeronautics and Space Administration (1977).

[20] W. L. Flower, C. T. Bowman, Measurement of the Structure of Sooting Laminar Diffusion Flames at Elevated Pressures, in: Twentieth Symposium (Internation) on Combusion, 1984, pp. 1035–1044.

[21] W. L. Flower, C. T. Bowman, Measurement of the effect of elevated pressure on soot formation in laminar diffusion flames, Combustion Science and Technology 37 (1-2) (1984) 93–97.

[22] W. L. Flower, The Effect of Elevated Pressure on the Rate of Soot Production in Laminar Diffusion Flames, Combustion Science and Technology 48 (1-2) (1986) 31–43.

[23] W. L. Flower, C. T. Bowman, Observations on the soot formation mechanism in laminar ethylene-air diffusion flames at one and two atmospheres, Combustion Science and Technology 53 (2-3) (1987) 217–224.

[24] W. L. Flower, C. T. Bowman, Soot production in axisymmetric laminar diffusion flames at pressures from one to ten atmospheres, in: Twenty-First Symposium (International) on Combustion, 1986, pp. 1115–1124.

[25] W. Lee, Y. D. Na, Soot study in laminar diffusion flames at elevated pressure using two-color pyrometry and Abel inversion, JSME International Journal Series B 43 (4) (2000) 550–5.

[26] L. L. McCrain, W. L. Roberts, Measurements of the soot volume field in laminar diffusion flames at elevated pressures, Combustion and Flame 140 (1-2) (2005) 60–69.

[27] T. L. Berry, W. L. Roberts, Measurement of smoke point in velocity-matched coflow laminar diffusion flames with pure fuels at elevated pressures, Combustion and Flame 145 (3) (2006) 571–578.

[28] T. L. Berry Yelverton, W. L. Roberts, Effect of Dilution, Pressure, and Velocity on Smoke Point in Laminar Jet Flames, Combustion Science and Technology 180 (7) (2008) 1334–1346.

[29] T. L. Berry Yelverton, W. L. Roberts, Soot surface temperature measurements in pure and diluted flames at atmospheric and elevated pressures, Experimental Thermal and Fluid Science 33 (1) (2008) 17–22.

[30] K. A. Thomson, Ö. L. Gülder, E. J. Weckman, R. A. Fraser, G. J. Smallwood, D. R. Snelling, Soot concentration and temperature measurements in co-annular, nonpremixed CH4 / air laminar flames at pressures up to 4 MPa, Combustion and Flame 140 (2005) 222–232.

[31] H. I. Joo, Ö. L. Gülder, Soot formation and temperature field structure in co-flow laminar methane-air diffusion flames at pressures from 10 to 60 atm, Proceedings of the Combustion Institute 32 (1) (2009) 769–775.

[32] D. S. Bento, K. A. Thomson, Ö. L. Gülder, Soot formation and temperature field structure in laminar propane-air diffusion flames at elevated pressures, Combustion and Flame 145 (4) (2006) 765–778.

[33] P. M. Mandatori, Ö. L. Gülder, Soot formation in laminar ethane diffusion flames at pressures from 0.2 to 3.3MPa, Proceedings of the Combustion Institute 33 (1) (2011) 577–584.

[34] H. I. Joo, Ö. L. Gülder, Experimental study of soot and temperature field structure of laminar co-flow ethylene-air diffusion flames with nitrogen dilution at elevated pressures, Combustion and Flame 158 (3) (2011) 416–422.

[35] Ö. L. Gülder, G. Intasopa, H. I. Joo, P. M. Mandatori, D. S. Bento, M. E. Vaillancourt, Unified behaviour of maximum soot yields of methane, ethane and propane laminar diffusion flames at high pressures, Combustion and Flame 158 (10) (2011) 2037–2044.

[36] A. E. Karataş, Ö. L. Gülder, Soot formation in high pressure laminar diffusion flames, Progress in Energy and Combustion Science 38 (6) (2012) 818–845.

[37] International Sooting Flame (ISF) Workshop, `http://www.adelaide.edu.au/cet/isfworkshop/`, accessed: 2016-11-30.

[38] R. K. Abhinavam Kailasanathan, E. K. Book, T. Fang, W. L. Roberts, Hydrocarbon species concentrations in nitrogen diluted ethylene-air laminar jet diffusion flames at elevated pressures, Proceedings of the Combustion Institute 34 (1) (2013) 1035–1043.

[39] R. K. Abhinavam Kailasanathan, T. L. B. Yelverton, T. Fang, W. L. Roberts, Effect of diluents on soot precursor formation and temperature in ethylene laminar diffusion flames, Combustion and Flame 160 (3) (2013) 656–670.

[40] A. Valavanidis, K. Fiotakis, T. Vlachogianni, Airborne Particulate Matter and Human Health: Toxicological Assessment and Importance of Size and Composition of Particles for Oxidative Damage and Carcinogenic Mechanisms, Journal of Environmental Science and Health, Part C 26 (4) (2008) 339–362.

[41] K. A. Thomson, D. R. Snelling, G. J. Smallwood, F. Liu, Laser induced incandescence measurements of soot volume fraction and effective particle size in a laminar co-annular non-premixed methane / air flame at pressures between 0.5-4.0 MPa, Applied Physics B 83 (2006) 469–475.

[42] C. H. Kim, F. Xu, G. M. Faeth, Soot surface growth and oxidation at pressures up to 8.0 atm in laminar nonpremixed and partially premixed flames, Combustion and Flame 152 (3) (2008) 301–316.

[43] A. G. Mouis, A. Menon, V. Katta, T. A. Litzinger, M. Linevsky, R. J. Santoro, S. P. Zeppieri, M. B. Colket, W. M. Roquemore, Effects of m-xylene on aromatics and soot in laminar, N2-diluted ethylene co-flow diffusion flames from 1 to 5 atm, Combustion and Flame 159 (10) (2012) 3168–3178.

[44] A. G. Mouis, T. A. Litzinger, Y. Wang, V. Iyer, S. S. Iyer, M. Linevsky, R. J. Santoro, V. Katta, Effects of a JP-8 surrogate and its components on soot in laminar, N2-diluted ethylene co-flow diffusion flames from 1 to 5atm, Combustion and Flame (2015) 1–9

[45] A. E. Karataş, G. Intasopa, Ö. L. Gülder, Sooting behaviour of n-heptane laminar diffusion flames at high pressures, Combustion and Flame 160 (9) (2013) 1650–1656.

[46] L. Zhou, N. J. Dam, M. D. Boot, L. P. H. de Goey, Measurements of sooting tendency in laminar diffusion flames of n-heptane at elevated pressure, Combustion and Flame 160 (11) (2013) 2507–2516.

[47] L. Zhou, N. J. Dam, M. D. Boot, L. P. H. de Goey, Investigation of the effect of molecular structure on sooting tendency in laminar diffusion flames at elevated pressure, Combustion and Flame 161 (10) (2014) 2669–2677.

[48] L. Figura, A. Gomez, Laminar counterflow steady diffusion flames under high pressure (P3MPa) conditions, Combustion and Flame 159 (1) (2012) 142–150.

[49] H. Gohari Darabkhani, Q. Wang, L. Chen, Y. Zhang, Impact of co-flow air on buoyant diffusion flames flicker, Energy Conversion and Management 52 (8-9) (2011) 2996–3003.

[50] K.-C. Lin, G. M. Faeth, Hydrodynamic suppression of soot emissions in laminar diffusion flames, Journal of Propulsion and Power 12 (1) (1996) 10–17.

[51] Z. Dai, G. M. Faeth, Hydrodynamic suppression of soot formation in laminar coflowing jet diffusion flames, Proceedings of the Combustion Institute 28 (1) (2000) 2085–2092.

[52] R. K. Abhinavam Kailasanathan, Experimental investigations on ethylene laminar flames at elevated pressures, Ph.D. thesis, North Carolina State University (2012).

[53] R. J. Santoro, H. G. Semerjian, R. A. Dobbins, Soot Particle Measurements in Diffusion Flames, Combustion and Flame 51 (1983) 203–218.

[54] Ö. L. Gülder, K. A. Thomson, D. R. Snelling, Effect of fuel nozzle material properties on soot formation and temperature field in coflow laminar diffusion flames, Combustion and Flame 144 (1-2) (2006) 426–433.

[55] R. K. Abhinavam Kailasanathan, J. Zhang, T. Fang, W. L. Roberts, Effects of Diluents on Soot Surface Temperature and Volume Fraction in Diluted Ethylene Diffusion Flames at Pressure, Combustion Science and Technology 186 (6) (2014) 815–828.

[56] S. A. Steinmetz, T. Fang, W. L. Roberts, Soot particle size measurements in ethylene diffusion flames at elevated pressures, Combustion and Flame 169 (2016) 85–93.

[57] K. A. Thomson, Soot Formation in Annular Non-premixed Laminar Flames of Methane-Air at Pressures of 0.1 to 4.0 MPa, Ph.D. thesis, University of Waterloo (2004).

[58] Y. Li, Applications of transient grating spectroscopy to temperature and transport properties measurements in high-pressure environments, Ph.D. thesis, North Carolina State University (2001).

[59] T. L. B. Yelverton, Soot formation in laminar jet diffusion flames at elevated pressures, Phd, North Carolina State University (2008).

[60] R. J. Santoro, J. H. Miller, Soot Particle Formation in Laminar Diffusion Flames, Langmuir 3 (2) (1987) 244–254.

[61] R. Puri, T. F. Richardson, R. J. Santoro, R. A. Dobbins, Aerosol Dynamic Processes of Soot Aggregates in a Laminar Ethene Diffusion Flame, Combustion and Flame 92 (1993) 320–333.

[62] Ü. Ö. Köylü, Y. C. Xing, D. E. Rosner, Fractal morphology analysis of combustion-generated aggregates using angular light scattering and electron microscope images, Langmuir 11 (12) (1995) 4848–4854.

[63] Ü. Ö. Köylü, Quantitative analysis of in situ optical diagnostics for inferring particle/aggregate parameters in flames: Implications for soot surface growth and total emissivity, Combustion and Flame 109 (3) (1997) 488–500.

[64] T. C. Williams, C. R. Shaddix, K. A. Jensen, J. M. Suo-Anttila, Measurement of the dimensionless extinction coefficient of soot within laminar diffusion flames, International Journal of Heat and Mass Transfer 50 (2007) 1616–1630.

[65] C. M. Sorensen, Light Scattering by Fractal Aggregates : A Review, Aerosol Science and Technology 35 (November) (2001) 648–687.

[66] K. A. Thomson, M. R. Johnson, D. R. Snelling, G. J. Smallwood, Diffuse-light two-dimensional line-of-sight attenuation for soot concentration measurements, Applied Optics 47 (5).

[67] J. Manin, L. M. Pickett, S. A. Skeen, Two-Color Diffused Back-Illumination Imaging as a Diagnostic for Time-Resolved Soot Measurements in Reacting Sprays, SAE International Journal of Engines 6 (4) (2013) 2013–01–2548.

[68] J. Manin, S. A. Skeen, L. M. Pickett, Understanding soot optical properties through dual-wavelength diffused back-illumination imaging, in: THIESEL Conference on Thermo- and Fluid Dynamic Processes in Direct Injection Engines, 2014.

[69] H. A. Michelsen, F. Liu, B. F. Kock, H. Bladh, A. Boiarciuc, M. Charwath, T. Dreier, R. Hadef, M. Hofmann, J. Reimann, S. Will, P.-E. Bengtsson, H. Bockhorn, F. Foucher, K.-P. Geigle, C. Mounaïm-Rousselle, C. Schulz, R. Stirn, B. Tribalet, R. Suntz, Modeling laser-induced incandescence of soot : a summary and comparison of LII models, Applied Physics B: Lasers and Optics 87 (2007) 503–521.

[70] F. Liu, K. J. Daun, D. R. Snelling, G. J. Smallwood, Heat conduction from a spherical nano-particle: Status of modeling heat conduction in laser-induced incandescence, Applied Physics B: Lasers and Optics 83 (3) (2006) 355–382.

[71] H. A. Michelsen, C. Schulz, G. J. Smallwood, S. Will, Laser-induced incandescence: Particulate diagnostics for combustion, atmospheric, and industrial applications, Progress in Energy and Combustion Science 51 (2015) 2–48.

[72] G. Comte-Bellot, Hot-wire anemometry, Annual Review of Fluid Mechanics 8 (1) (1976) 209–231.

[73] C. J. Dasch, One-dimensional tomography: a comparison of Abel, onion-peeling, and filtered backprojection methods, Applied optics 31 (8) (1992) 1146–1152.

[74] K. J. Daun, K. A. Thomson, F. Liu, G. J. Smallwood, Deconvolution of axisymmetric flame properties using Tikhonov regularization, Applied optics 45 (19) (2006) 4638–46.

[75] E. O. Åkesson, K. J. Daun, One- and Two-Dimensional Tikhonov-Regularized Tomography for Axisymmetric Flames, in: 37th AIAA Fluid Dynamics Conference and Exhibit, no. June, 2007.

[76] E. O. Åkesson, K. J. Daun, Parameter selection methods for axisymmetric flame tomography through Tikhonov regularization., Applied optics 47 (3) (2008) 407–16.

[77] F. G. Roper, C. Smith, A. C. Cunningham, The prediction of laminar jet diffusion flame sizes: Part II. Experimental verification, Combustion and Flame 29 (1977) 227–234.

[78] F. G. Roper, The prediction of laminar jet diffusion flame sizes: Part I. Theoretical model, Combustion and Flame 29 (1977) 219–226.

[79] Ö. L. Gülder, Corrigendum to "Dependence of sooting characteristics and temperature field of co-flow laminar pure and nitrogen-diluted ethylene-air diffusion flames on pressure" (Combustion and Flame (2015) 162(4) (1566-1574)), Combustion and Flame 173 (2016) 1.

[80] C. K. Law, G. M. Faeth, Opportunities and challenges of combustion in microgravity, Progress in Energy and Combustion Science 20 (1) (1994) 65–113.

[81] R. W. Davis, E. F. Moore, R. J. Santoro, J. R. Ness, Isolation of Buoyancy Effects in Jet Diffusion Flame Experiments, Combustion Science and Technology 73 (August 2011) (1990) 625–635.

[82] H. Gohari Darabkhani, Y. Zhang, Methane Diffusion Flame Dynamics at Elevated Pressures, Combustion Science and Technology 182 (3) (2010) 231–251.

[83] E. R. Subbarao, B. J. Cantwell, Investigation of a co-flowing buoyant jet: experiments on the effect of Reynolds number and Richardson number, Journal of Fluid Mechanics 245 (1992) 69–90.

[84] M. R. J. Charest, C. P. T. Groth, Ö. L. Gülder, A numerical study on the effects of pressure and gravity in laminar ethylene diffusion flames, Combustion and Flame 158 (10) (2011) 1933–1945.

[85] M. R. J. Charest, C. P. T. Groth, Ö. L. Gülder, Effects of gravity and pressure on laminar coflow methaneair diffusion flames at pressures from 1 to 60 atmospheres, Combustion and Flame 158 (5) (2011) 860–875.

[86] A. Abdelgadir, I. A. Rakha, S. A. Steinmetz, A. Attili, F. Bisetti, W. L. Roberts, Effects of hydrodynamics and mixing on soot formation and growth in laminar coflow diffusion flames at elevated pressures, Combustion and Flame, in review.

[87] F. Bisetti, G. Blanquart, M. Mueller, H. Pitsch, On the formation and early evolution of soot in turbulent nonpremixed flames, Combustion and Flame 159 (1) (2012) 317–335.

[88] A. Attili, F. Bisetti, M. Mueller, H. Pitsch, Formation, growth, and transport of soot in a three-dimensional turbulent non-premixed jet flame, Combustion and Flame 161 (7) (2014) 1849–1865.

[89] A. Attili, F. Bisetti, M. Mueller, H. Pitsch, Damköhler number effects on soot formation and growth in turbulent nonpremixed flames, Proceedings of the Combustion Institute 35 (2) (2015) 1215–1223.

[90] A. E. Karataş, Ö. L. Gülder, Dependence of sooting characteristics and temperature field of co-flow laminar pure and nitrogen-diluted ethyleneair diffusion flames on pressure, Combustion and Flame 162 (2015) 1566–1574.

[91] M. R. J. Charest, H. I. Joo, Ö. L. Gülder, C. P. T. Groth, Experimental and numerical study of soot formation in laminar ethylene diffusion flames at elevated pressures from 10 to 35atm, Proceedings of the Combustion Institute 33 (1) (2011) 549–557.

[92] S. G. Rabinovich, Measurement errors and uncertainties, 3rd Edition, Springer science and media, Inc., New York, 2005.

[93] M. R. Kholghy, J. Weingarten, M. J. Thomson, A study of the effects of the ester moiety on soot formation and species concentrations in a laminar coflow diffusion flame of a surrogate for B100 biodiesel, Proceedings of the Combustion Institute 35 (1) (2015) 905–912.

[94] M. Hofmann, B. F. Kock, T. Dreier, H. Jander, C. Schulz, Laser-induced incandescence for soot-particle sizing at elevated pressure, Applied Physics B 90 (3-4) (2007) 629–639.

[95] P. Desgroux, X. Mercier, K. A. Thomson, Study of the formation of soot and its precursors in flames using optical diagnostics, Proceedings of the Combustion Institute 34 (1) (2013) 1713–1738.

[96] M. Saffaripour, K.-P. Geigle, D. R. Snelling, G. J. Smallwood, K. A. Thomson, Influence of rapid laser heating on the optical properties of in-flame soot, Applied Physics B 119 (2015) 621–642.

[97] E. Cenker, K. Kondo, G. Bruneaux, T. Dreier, T. Aizawa, C. Schulz, Assessment of soot-particle size imaging with LII at Diesel engine conditions through comparison with TEM analysis of soot samples, Applied Physics B: Lasers and Optics 119 (2015) 765–776.

[98] E. Cenker, G. Bruneaux, T. Dreier, C. Schulz, Sensitivity analysis for in-cylinder soot-particle size imaging with laser-induced incandescence, Applied Physics B: Lasers and Optics 119 (2015) 745–763.

[99] E. Cenker, G. Bruneaux, T. Dreier, C. Schulz, Determination of small soot particles in the presence of large ones from time-resolved laser-induced incandescence, Applied Physics B: Lasers and Optics 118 (2) (2015) 169–183.

[100] M. A. Dansson, M. Boisselle, M. A. Linne, H. A. Michelsen, Complications to optical measurements using a laser with an unstable resonator : a case study on laser-induced incandescence of soot, Applied Optics 46 (33) (2007) 8095–8103.

[101] F. Liu, G. J. Smallwood, D. R. Snelling, Effects of primary particle diameter and aggregate size distribution on the temperature of soot particles heated by pulsed lasers, Journal of Quantitative Spectroscopy and Radiative Transfer 93 (1-3 SPEC. ISS.) (2005) 301–312.

[102] M. Charwath, R. Suntz, H. Bockhorn, Constraints of two-colour TiRe-LII at elevated pressures, Applied Physics B 104 (2) (2011) 427–438.

[103] H. A. Michelsen, Laser-induced incandescence of flame-generated soot on a picosecond time scale, Applied Physics B 83 (3) (2006) 443–448.

[104] M. Hofmann, W. G. Bessler, C. Schulz, H. Jander, Laser-induced incandescence for soot diagnostics at high pressures., Applied optics 42 (12) (2003) 2052–2062.

[105] F. Liu, B. J. Stagg, D. R. Snelling, G. J. Smallwood, Effects of primary soot particle size distribution on the temperature of soot particles heated by a nanosecond pulsed laser in an atmospheric laminar diffusion flame, International Journal of Heat and Mass Transfer 49 (3-4) (2006) 777–788.

[106] H. F. Calcote, D. M. Manos, Effect of Molecular Structure on Incipient Soot Formation, Combustion and Flame 49 (1983) 289–304.

[107] Y. Wang, S. H. Chung, Effect of strain rate on sooting limits in counterflow diffusion flames of gaseous hydrocarbon fuels: Sooting temperature index and sooting sensitivity index, Combustion and Flame 161 (5) (2014) 1224–1234.

[108] C. S. McEnally, L. D. Pfefferle, Improved sooting tendency measurements for aromatic hydrocarbons and their implications for naphthalene formation pathways, Combustion and Flame 148 (4) (2007) 210–222.

[109] C. S. McEnally, L. D. Pfefferle, Sooting tendencies of nonvolatile aromatic hydrocarbons, Proceedings of the Combustion Institute 32 (1) (2009) 673–679.

[110] C. S. McEnally, L. D. Pfefferle, Supporting Information for Sooting tendencies of oxygenated hydrocarbons in laboratory-scale flames (2011) 1–20.

[111] M. Kashif, P. Guibert, J. Bonnety, G. Legros, Sooting tendencies of primary reference fuels in atmospheric laminar diffusion flames burning into vitiated air, Combustion and Flame 161 (6) (2014) 1575–1586.

[112] N. A. Eaves, A. Veshkini, C. Riese, Q. Zhang, S. B. Dworkin, M. J. Thomson, A numerical study of high pressure, laminar, sooting, ethaneair coflow diffusion flames, Combustion and Flame 159 (10) (2012) 3179–3190.

[113] A. E. Daca, Ö. L. Gülder, Soot formation characteristics of diffusion flames of methane doped with toluene and n-heptane at elevated pressures, Proceedings of the Combustion Institute

[114] J. Y. Hwang, W. Lee, H. G. Kang, S.-H. Chung, Synergistic effect of ethylene-propane mixture on soot formation in laminar diffusion flames, Combustion and Flame 114 (3-4) (1998) 370–380.